

1-1-2013

Femtosecond Laser Nano-Fabrication And Its Biomedical Applications

Amirhossein Tavangar
Ryerson University

Follow this and additional works at: <http://digitalcommons.ryerson.ca/dissertations>

 Part of the [Mechanical Engineering Commons](#)

Recommended Citation

Tavangar, Amirhossein, "Femtosecond Laser Nano-Fabrication And Its Biomedical Applications" (2013). *Theses and dissertations*. Paper 1709.

This Dissertation is brought to you for free and open access by Digital Commons @ Ryerson. It has been accepted for inclusion in Theses and dissertations by an authorized administrator of Digital Commons @ Ryerson. For more information, please contact bcameron@ryerson.ca.

FEMTOSECOND LASER NANO-FABRICATION AND ITS BIOMEDICAL APPLICATIONS

by

Amirhossein Tavangar, B.Sc., M.Sc.

Mechanical Engineering

Iran University of Science and Technology, Tehran, Iran 2008

Amirkabir University of Technology, Tehran, Iran 2003

A dissertation presented to

Ryerson University in partial fulfillment of the requirements

for the degree of Doctor of Philosophy in the

Program of Mechanical and Industrial Engineering

Toronto, Ontario, CANADA

© Amirhossein Tavangar 2013

Author's Declaration

I hereby declare that I am the sole author of this dissertation. This is a true copy of the dissertation, including any required final revisions, as accepted by my examiners.

I authorize Ryerson University to lend this dissertation to other institutions or individuals for the purpose of scholarly research.

Amirhossein Tavangar

Department of Mechanical and Industrial Engineering

I further authorize Ryerson University to reproduce this dissertation by photocopying or by other means, in total or in part, at the request of other institutions or individuals for the purpose of scholarly research.

I understand that my dissertation may be made electronically available to the public.

Amirhossein Tavangar

Department of Mechanical and Industrial Engineering

Abstract

FEMTOSECOND LASER NANO-FABRICATION AND ITS BIOMEDICAL APPLICATIONS

© Amirhossein Tavangar 2013

Doctor of Philosophy in the Program of Mechanical and Industrial Engineering

This dissertation aims to develop a new technique for fabrication of three-dimensional (3-D) interwoven nanofibrous platforms using femtosecond laser ablation of solids in ambient conditions.

In the first part, the mechanism of ablation of solids by multiple femtosecond laser pulses in ambient air is described in an explicit analytical form. The formulas for evaporation rates and the number of ablated particles for laser ablation by multiple pulses as a function of laser parameters, background gas, and material properties are predicted and compared to experimental results. Later, the formation mechanism of the nanofibrous structures during laser ablation of targets in the presence of air is discussed. The results indicate that femtosecond laser ablation of solids at air background yields crystalline nanostructures. It's also shown that this technique allows synthesis of 3-D nanostructures on a wide range of materials including synthetic and natural materials.

Later, potential practice of the proposed technique for integration of nanostructures on transparent platforms as well as inside microstructures toward device fabrication is

investigated. Presented studies show that integrated nanostructure inside microchannels can be fabricated in one single step using this technique.

Finally, to address the potential use of the nanostructures for biomedical application, several studies are performed to evaluate the bioactivity and biocompatibility of the nanostructures. The fabricated nanostructures incorporate the functions of 3-D nano-scaled topography and modified chemical properties to improve osseointegration, while at the same time leaving space for delivering other functional agents. *In vitro* experiments reveal that the titania nanofibrous platforms possess an excellent bioactivity and can induce rapid, uniform, and controllable bone-like apatite precipitation once immersed in simulated body fluid (SBF). Furthermore, the influence of synthesized titanium platforms on the *in vitro* proliferation and viability of osteoblast-like MC3T3-E1 cells and NIH 3T3 mouse embryonic fibroblasts is investigated. The results from *in vitro* studies reveal that the platforms possess excellent biocompatibility and significantly enhance proliferation of both cell lines compared to the untreated titanium specimen. The cell population increases consistently with the density of nanofibrous structures. This approach of nano-engineering 3-D architectures suggests considerable perspective for promoting material interfacial properties to develop new functional biomaterials.

ACKNOWLEDGMENTS

There are many people whom I would like to thank for their support of my research during my graduate studies at Ryerson University. First, I would like to thank my supervisors, Prof. Krishnan Venkatakrishnan and Prof. Bo Tan for their invaluable advice and endless patience and support. I'm also grateful to thank my committee members, Prof. Ziad Saghir, Prof. Vincent Chan, Prof. Karthi Umpathy, and Prof. Muthukumaran Packirisamy who provided me a lot of references and research considerations. I would also like to thank Prof. Ahmad Ghasempour, Graduate Program Director in Mechanical and Industrial Engineering, the faculty members, the technical officers, and the administrative staff members for their kind support and cooperation throughout my studies and research at Ryerson University. I would like to particularly acknowledge Dr. Hassan Firoozmand for helping and teaching me how to use confocal microscopy and also Alan Machin and Andrew Heim for assisting with the material preparation and the experimental setup.

I would like to thank my colleagues, who are my good friends as well: Dr. Amirkianoosh Kiani for sharing the lab at day and night together from very beginning and his help on many things, Priyatha Premnath for helping me with the *in vitro* experiments, helpful discussions about cell biology, and her encouragement, Alireza Dalili for helpful suggestions and support, especially when I had just joined the group, and Helia Zahedi for her support and encouragement, particularly when I was writing the dissertation.

I would truly like to thank my wonderful friends who are like family and made this journey possible: Shadi Deljoomanesh, Dr. Arash Hariri, Dr. Masroor Mohajerani, Dr. Pooyan Hashemi, and Amar khojasteh.

Lastly, I would like to express my deepest gratitude and love to my family, especially my mom, for their unfailing love, support, and prayer.

*Dedicated to my family, especially my mother,
who have always shown unfailing love and support*

TABLE OF CONTENTS

Acknowledgments	v
List of Figures	xiii
List of Tables	xxiii
List of Abbreviation.....	xxiv
List of Symbols	xxvi
1 Introduction	1
1.1 Nanostructures.....	1
1.2 Nanofabrication techniques	2
1.2.1 Anodization technique	4
1.2.2 Electrospining technique	4
1.2.3 Laser ablation technique.....	5
1.3 Nanostructured materials.....	8
1.3.1 Synthetic materials.....	8
1.3.2 Natural materials	11

1.4	Research objective	13
1.5	Organization of the dissertation.....	14
2	Physics of Ultrashort Laser Interaction with Solids	16
2.1	Mechanisms of ablation by ultra-short laser pulses.....	17
2.1.1	Ablation threshold in vacuum.....	18
2.1.2	Ablation thresholds in ambient gas	21
2.2	Summary.....	26
3	Experimental Setup and Procedure	27
3.1	Fabrication system.....	28
3.1.1	Experimental Setup.....	28
3.1.2	Materials.....	29
3.1.3	Laser beam delivery.....	30
3.2	Surface characterization.....	32
3.2.1	Morphology characterizations.....	32
3.2.2	Chemical and phase characterizations	34
3.2.3	Physiochemical characterizations.....	35
4	Study of the Formation of 3-D Nanostructure Platforms	37
4.1	Laser Processing of Synthetic Material: Study of the ablation mechanism of Ti... 38	
4.1.1	Ablation mechanism by a single ultrashort laser pulse in ambient gas	39
4.1.2	Ablation rate in case of multiple laser pulses	41

4.1.3	Nanostructure growth in ambient air	43
4.1.4	Experimental Results and discussion	47
4.2	Laser Processing of Natural Biomaterial: Synthesis of 3-D calcium carbonate nanofibrous structure from eggshell	56
4.2.1	Materials and experimental details	57
4.2.2	Results and discussion	57
4.3	Laser Processing of Natural Material: Synthesis of 3-D Micro/Nanostructures on Rice Husk and Wheat Straw	62
4.3.1	Results and Discussions	62
4.4	Summary.....	68
5	Direct nanostructure integration into other structures.....	70
5.1	Incorporation of Nanofibrous structures on Transparent Platform.....	71
5.1.1	Laser-induced reverse transfer LIRT	72
5.1.2	Experimental detail and fabrication process	73
5.1.3	Results and discussions.....	73
5.2	Single-step Generation and Incorporation of Nanofibrous Membrane into Microchannels	81
5.2.1	Membranes.....	81
5.2.2	Experimental details.....	82
5.2.3	Results and discussions.....	83

5.2.4	Effect of laser scanning parameters	85
5.2.5	Study of pore size and density of nanofibrous structure	86
5.3	Summary.....	91
6	Bioassay of manufactured platforms.....	92
6.1	Bioactivity assay of synthesized 3-D Titania Nanofibrous Platforms.....	93
6.1.1	Experimental detail.....	94
6.1.2	Sample SBF soaking for in vitro assessment.....	94
6.1.3	Result and discussion.....	95
6.2	The Influence of Titania Nanofibrous Platforms on Cell Behavior	106
6.2.1	Experimental details.....	107
6.2.2	Results and discussion.....	110
6.2.3	Discussion.....	118
6.3	Summary.....	122
7	Summary and future research.....	123
7.1	Summary.....	123
7.2	Recommended future work	127
	Appendices	129
	Appendix A	130
A.1	Refereed Journal.....	130

A.2 Refereed conference papers.....	131
A.3 Submitted to refereed journals	131
Appendix B	132
B.1 Preparation of modified simulated body fluid (m-SBF)	132
B.1.1 Reagents for m-SBF	132
B.1.2. Ion concentrations of m-SBF	133
B.1.3. Preparation procedure of m-SBF	133
B.1.4. Preservation of SBF	134
B.2. Procedure of apatite-forming ability test.....	134
Appendix C.....	136
C.1 Cell culture.....	136
C.2 Cell proliferation	137
References	138

LIST OF FIGURES

Figure 1.1 (a) SEM image of poly L-lactic acid (PLLA) porous scaffold fabricated by phase-separation technique [4]. (b) Electrospun nanofibers [5]. (c) Aligned single wall carbon nanotube (SWCNT) grown with water-assisted chemical vapor deposition [6]. (d) TEM image of monodispersed magnetic nanoparticles deposited from hexane dispersion and dried at room temperature [7], image modified from [1]..... 3

Figure 1.2 Schematic showing the electrospinning process, taken from [19] 5

Figure 3.1 Experimental setup..... 28

Figure 3.2 Schematic of telecentric scanning lens..... 32

Figure 4.1 SEM images of titania nanofibrous structures generated on a Ti substrate at laser repetition of a) 4 MHz and b) 12 MHz..... 47

Figure 4.2 The number of ablated atoms from the Ti target at different laser pulse repetition rates at laser pulse dwell time of 1ms based on Eq. 4.9 depicted by the blue hollow line. The

red solid line represents the absorbed laser fluence by the Ti target. The dashed line determines the laser ablation threshold of 0.42 J/cm^2 for Ti..... 49

Figure 4.3 The average evaporation rate for a single pulse at different laser fluences predicted by Eq. 4.6..... 49

Figure 4.4 TEM images of Ti nanofibers synthesized at repetition (a) 4 MHz, (b) 8 MHz, and (c) 12MHz (the scale bar : 100nm). 50

Figure 4.5 Measured average nanofiber diameter at different laser pulse repetition rates.. 51

Figure 4.6 Measured average pore sizes of generated structures at different laser pulse repetition rates..... 52

Figure 4.7 The number of ablated atoms from the Ti target at different laser dwell time and laser pulse repetition rate predicted by Eq. 2.17. 52

Figure 4.8 X-ray Diffraction patterns of generated titania nanofibrous layer Ti sample after laser irradiation..... 54

Figure 4.9 Schematic illustration of titania nanofibrous structure using femtosecond laser ablation of Titanium target. 55

Figure 4.10 SEM images of calcium carbonate nanofibrous structure synthesized on an eggshell at laser repetition rate of 4 MHz..... 58

Figure 4.11 TEM images of calcium carbonate nanofibers synthesized at repetition rate of 4 MHz at magnification of a) X50000 and b) X100000..... 58

Figure 4.12 SEM images of calcium carbonate nanofibrous structure synthesized on an eggshell at laser repetition rates of (a) 8 MHz, and (b) 13 MHz..... 59

Figure 4.13 EDS analyses of (a) unprocessed eggshell, and (b) synthesized calcium carbonate nanofibrous structure..... 59

Figure 4.14 X-ray Diffraction patterns of (a) unprocessed eggshell (b) nanofibrous structure generated on the eggshell substrate. The peaks marked with asterisk (*) correspond to calcium hydroxide..... 60

Figure 4.15 SEM micrograph of structure generated on rice husk at laser rep of 26 MHz, and dwell time of 0.1 ms beam power of 15W at magnification of a) X10K, b) X50K, and c) X200K. 63

Figure 4.16 SEM micrograph of structure generated on rice husk at laser rep of 26 MHz, dwell time of 0.1 ms and beam power of 10W at magnification of a) X20K, b) X50K, and c) X200K. 64

Figure 4.17 SEM micrograph of structure generated on rice husk at laser rep of 26 MHz, and dwell time of 0.1 ms beam power of 5W at magnification of a) X10K, b) X20K, and c) X50K. 65

Figure 4.18 EDXs analyses of a) unprocessed rice husk and b) structures generated on rice husk at laser rep of 26 MHz and power 5W, c) structures generated on rice husk at laser rep of 26 MHz and power 10W, and d) structures generated on rice husk at laser rep of 26 MHz and power 15W..... 65

Figure 4.19 SEM micrographs of structure generated on Rice husk at laser rep. of 26 MHz, dwell time of 0.05 ms, and power of 5W at magnification of a) X1K, b) X5K, and c) X10K. . 66

Figure 4.20 SEM micrographs of structure generated on wheat straws at laser rep of 26 MHz, dwell time of 0.05 ms, and power of 5W at magnification of a) X1K, b) X5K, and c) X10K (Same parameters as Figure 4.19 but at different location)..... 67

Figure 4.21 SEM micrographs of structure generated on Rice husk at laser rep. of 26 MHz, dwell time of 0.05 ms, and power of 10W at magnification of a) X1K, b) X5K, and c) X10K.67

Figure 4.22 SEM micrographs of structure generated on wheat straws at laser rep of 26 MHz, dwell time of 0.05 ms, and power of 15W at magnification of a) X1K, b) X5K, and c) X10K..... 68

Figure 5.1 Schematic of Laser-Induced Reverse Transfer process..... 73

Figure 5.2 SEM image of Aluminum deposition formed by laser beam of 515 nm wavelength, at freq. of 13 MHz and machining velocity of 1000 mm/s. 75

Figure 5.3 SEM image of silicon nanofibers deposited on a glass acceptor with gap of 60 μm and formed by laser beam of 515 nm wavelength, at frequency of 13 MHz and machining velocity of 1000 $\mu\text{m/s}$ at magnification of a) X1000 and b) X25000..... 76

Figure 5.4 SEM image of silicon nanofibers deposited on a glass substrate with gap of 120 μm and formed by laser beam of 515 nm wavelength, at frequency of 13 MHz and machining velocity of 1000 mm/s at magnification of a) X10000 and b) X2000..... 77

Figure 5.5 SEM image of Aluminum nanofibers deposited on a glass acceptor with a) gap of 60 μm and b) gap of 180 μm formed by laser beam of 515 nm wavelength, at frequency of 13 MHz and machining velocity of 1000 mm/s..... 78

Figure 5.6 SEM image of three different zones of silicon nanofibers deposited on a glass acceptor with gap of 120 μm and formed by laser beam of 515nm wavelength, at frequency of 13 MHz and machining velocity of 1000 mm/s..... 79

Figure 5.7 EDS analysis of aluminum oxide nanofibers deposited on a glass acceptor. 80

Figure 5.8 EDS analysis of a) pure Si and b) silicon oxide nanofibers deposited on a Si substrate..... 80

Figure 5.9 Fabrication set up..... 83

Figure 5.10 3-D and plane view of the microchannel and sequences of nanofiber growth inside the microchannel. The related SEM images corresponding to each sequence are

brought on the bottom. The microchannels were formed by laser beam at freq. of 13 MHz with laser scanning speed of 1000 mm/s after a) 5 and b) 20 scanning passes..... 84

Figure 5.11 SEM cross sectional image of nanofibrous structure inside a microfluidic channel formed by laser beam at freq. of 13 MHz with laser scanning speed of a) 1000 mm/s and b) 2000 mm/s..... 86

Figure 5.12 SEM cross sectional image of nanofibrous structure growth sequences inside the microfluidic channel formed by 1040 nm wavelength laser beam at freq. of 26 MHz after a) 5, b) 10, and c) 20 laser scanning passes. 86

Figure 5.13 SEM cross sectional image and pore diameter distribution graph of nanofibrous structure inside the microfluidic channel formed by laser beam of 1040 nm wavelength, at freq. of a) 8 MHz b) 13 MHz, and c) 26 MHz..... 88

Figure 5.14 SEM image and pore diameter distribution graph of nanofibrous structure inside the microfluidic channel formed by laser beam at freq. of 26 MHz with pulse width of a) 214 fs b) 1428 fs, and c) 3500 fs..... 90

Figure 5.15 Energy dispersive X-ray spectroscopy (EDS) analysis of a) pure Si and b) silicon oxide nanofibers deposited on a Si substrate..... 90

Figure 6.1 SEM images of titania nanofibrous structure synthesized on the Ti4 sample at laser repetition of 4 MHz at magnifications of a) X500, b) X1000, and c) X2500..... 96

Figure 6.2 SEM images of titania nanofiberous structure synthesized on the Ti8 at laser repetition of 12 MHz at magnifications of a) X500, b) X1000, and c) X5000. 96

Figure 6.3 SEM images of titania nanofiberous structure synthesized on the Ti12 at laser repetition of 12 MHz at magnifications of a) X500, b) X1000, and c) X5000. 97

Figure 6.4 TEM images of Ti nanofibers synthesized at repetition of a) 12 MHz and b) 8 MHz. 97

Figure 6.5 XRD patterns of a) an unprocessed Ti sample and b) the titania nanofibrous layer generated on the Ti4 sample after laser irradiation. 98

Figure 6.6 SEM images of surface morphology of an unprocessed Ti sample after a day soaking in SBF and b) SEM image of theTi4 morphology which compares the different apatite-inducing abilities of (1) the unprocessed area, and (2) the nanofibrous layer after soaking for 3 days. 99

Figure 6.7 SEM images of the Ti12 surface morphology after soaking in SBF for a) 1day and b) 3days. 99

Figure 6.8 SEM images of the Ti8 surface morphology after soaking in SBF for a) 1day and b) 3days. 100

Figure 6.9 SEM images of Ti4 surface morphology after soaking in SBF for a) 1day and b) 3days. 100

Figure 6.10 EDS analysis of Ti4 after soaking in SBF for a) 1day and b) 3days 101

Figure 6.11 XRD analysis of Ti4 after soaking in SBF for a) 1day and b) 3days.....	102
Figure 6.12 Microscopic images of a distilled water droplet on a) an unprocessed Ti and b) nanofibrous layer on the Ti8.	103
Figure 6.13 Sessile drop water contact angle measurement for an unprocessed Ti substrate, and the titania nanofibrous layer on the Ti4, Ti8, and Ti12.....	103
Figure 6.14 SEM images of titania nanofibrous structure of a) Ti2 sample at laser repetition of 8 MHz and dwell time of 2ms and b) Ti10 sample at laser repetition of 8 MHz and dwell time of 10ms.	110
Figure 6.15 Sessile drop water contact angle measurement for the control sample, and the titania nanofibrous structures on the Ti2 and Ti10.	112
Figure 6.16 Zeta potential values for the control sample and the titania nanofibrous structures on the Ti2 and Ti10.	113
Figure 6.17 Force-distance curves taken at for the (a) control sample and the titania nanofibrous structures on the (b) Ti2 and (c) Ti10.	113
Figure 6.18 Adhesion energy calculated from the area under the force-height curves for the control sample and the titania nanofibrous structures on the Ti2 and Ti10.....	114
Figure 6.19 MTT assay of MC3T3-E1 cells (solid red) and NIH3T3 cells (stripe blue) seeded and incubated for 48 hrs on Ti2, Ti10, and control samples.	115

Figure 6.20 Representative SEM images of MC3T3-E1 cells after 1 day on the control substrate and titania nanofibrous structure. Images show a higher degree of MC3T3-E1 activation and matrix formation on titania nanofibrous structure. The close-up image on the right indicates MC3T3-E1 cell extension on the surface of titania nanofibrous structure. Arrows show cells spreading on the nanofibrous structures. Note that the substrates were coated with a 10 nm layer of gold and imaged at 5 keV. Experiments were replicated on at least three different samples.....116

Figure 6.21 Representative SEM images of NIH3T3 cells after 1 day on (a) the titania nanofibrous structure and (b) the control substrate. Images show a higher degree of cell activation and matrix formation on titania nanofibrous structure. Arrows show cells spreading on the nanofibrous structures. Note that the substrates were coated with a 10 nm layer of gold and imaged at 15 keV. Experiments were replicated on at least three different samples.....117

Figure 6.22 Schematic illustrations demonstrating the mechanism of apatite formation on nanofibers surface. a) The nanofibers surface is slightly negative due to the deprotonation of acidic hydroxides. b) A negatively charged surface attracts **Ca²⁺** cations and forms calcium hydroxide. c) Phosphate ions (**PO₄³⁻**) present in the SBF react with the calcium hydroxide layer that results in apatite nuclei formation. d) Since SBF is a supersaturated solution of Ca and P ions, bone-like apatite spheroids grow spontaneously on apatite nuclei sites.....119

Figure 6.23 Comparison of the cell interaction and adhesion to the surface of a) control sample, b) surface with lower nanofiber density, and c) surface with lower nanofiber density. Upon immersion in culture media, proteins are adsorbed to the titania nanofibrous structures. By increasing the density of nanofibers and consequently increasing the surface area, more protein would be adsorbed to the nanostructures. These proteins would then act as potential adhesion sites for the cells.....121

LIST OF TABLES

Table 6.1 Ion concentration of m-SBF in comparison with blood plasma, taken from [152]	95
Table B.1 Order, amounts, and purities of reagents for preparing 1000 ml of m-SBF, adopted from [177]	134

LIST OF ABBREVIATION

Å Angstrom, 46

AFM Atomic force microscopy, 47

BSA Bovine serum albumin, 147

BSE Backscattered electrons, 45

CVD Chemical vapor deposition, 92

DMEM Dulbecco's Modified Eagle Medium, 133

DMSO dimethyl sulfoxide, 134

DPBS *dulbecco's phosphate buffered saline*, 134

DPBS Dulbecco's Phosphate-Buffered Saline, 133

EDS Energy dispersive X-ray spectroscopy, 46

fs Femtosecond, 42

HA Hydroxyapatite, 72

HAZ Heat affected zone, 22

HEPS 4-(2-hydroxyethyl)-1-piperazineethanesulfonic acid, 117

LCVD Laser chemical vapor deposition, 92

LIFT Laser-induced forward transfer, 92

LIRT Laser induced reverse transfer, 93

MC3T3-E1 Osteoblast-like MC3T3-E1 cells, 130

MEMS microelectromechanical systems, 22

MEMS Microelectromechanical systems, 22

MHz Megahertz pulse, 38

m-SBF modified simulated body fluid, 117

MTT 3-(4,5-Dimethylthiazol-2-Yl)-2,5-Diphenyltetrazolium Bromide, 134

NEMS nanoelectromechanical systems, 22

NEMS Nanoelectromechanical systems, 22

NIH 3T3 Mouse embryonic fibroblasts, 130

NIH 3T3 NIH 3T3 mouse embryonic fibroblasts, 130

nm Nanometer, 42

OCP Octacalcium phosphate, 124

ps Picosecond, 42

SBF simulated body fluid, 25

SEM Scanning electron microscope, 41

TEM Transmission electron microscopy, 41, 45

XRD X-Ray Diffraction, 41

ZP Zeta potential, 48

μm Micrometer, 43

LIST OF SYMBOLS

a	Thermal diffusion coefficient, [cm^2/s]
A	Target laser absorption coefficient
A_{foc}	Irradiation focal spot area, [cm^2]
C_p	Specific heat, [$J/(g K)$]
D	The laser beam diameter
D_0	Theoretical laser minimum spot diameter, [cm]
D_{dv}	Diffusion velocity
D_t	Laser beam dwell time of
f	Effective focal length of the lens
F_0	Incident laser fluence, [J/cm^2]
F_{th}^d	Ablation threshold of a dielectric, [J/cm^2]
F_{th}^m	Ablation threshold of a metal, [J/cm^2]
I_0	Incident laser energy, [W/cm^2]
I_a	Absorbed laser energy, [W/cm^2]
J_i	Ionization potential [eV]

k	Imaginary part of material refractive index
k_h	Heat conduction coefficient, $[W/(cm K)]$
l_{abl}	The ablation depth
l_{g-k}	Gas-kinetic mean free path in air in standard conditions
n	Real part of material refractive index
n_e	Electron number density
N_p	Number of atoms evaporated per single pulse
N_{MP}	Number of atoms evaporated at multiple pulses
P_{ave}	Average power, $[W]$
R	Target laser reflection coefficient
R_{rep}	Laser repetition rate, $[s^{-1}]$
$(R_{evp})_{therm}$	Thermal evaporation, $[\frac{atoms}{cm^2}]$
t_{b-s}	Bulk-to-surface energy transfer time at the maximum temperature
t_{eq}	Equilibration time
t_p	Laser pulse duration, $[s]$
T_{eq}	Solid-air surface equilibration temperature, $[K]$
T_{max}	Maximum temperature at the end of the laser pulse, $[K]$
ϵ	Material refractive index
ϵ_b	Binding energy, $[eV]$
ϵ_e	Fermi energy, $[eV]$
ϵ_{kin}	Kinetic energy of an atom, $[eV]$
ϵ_{wf}	Work function, $[eV]$
λ_0	Wavelength of the laser, $[nm]$
v_{th}	Average thermal velocity in air

ω	Laser frequency, [Hz]
ρ_0	Target material density, [g/cm^3]
σ_{Ti-air}	Cross section for titanium-air elastic collision
σ_{total}	Total cross section

CHAPTER 1

INTRODUCTION

1.1 Nanostructures

Nanotechnology is considered as a key technology of current century, as it influences not only microelectronic technologies but also biological, medical, and chemical industries. Nanotechnology is defined as the fabrication and characterization of devices with precision scale down to atomic or molecular level. Structures with basic structural units, grains, particles, fibers or other constituent components smaller than 100 nm in at least one dimension are considered nanostructures [1]. Nanostructures have drawn great attention due to the unique physical and chemical properties exhibited when the size of particles are in the order of sub 100 nm. Nanostructures can be in forms of nanoparticles, nanoclusters, nanocrystals, nanotubes, nanofibers, nanowires, nanorods, nanofilms, etc. Synthesized nanostructures have numerous potential applications in the fabrication of

nano-devices in microelectronic, biomedical, photonic fields, tissue engineering and filtration technologies.

Generally, for all the applications to become practical, the major requirement is to develop an engineering nanofabrication approach that would allow processing of materials with the desired structural, mechanical, optical, magnetic, or electrical properties in almost atomic precision. Generally, the nanofabrication techniques are divided into two major categories in terms of the processes involved in creating nanoscale structures: “top-down” and “bottom-up” techniques. In top-down approaches, nanofabrication tools are used to create nanoscaled structures/functional devices with the desired shapes and characteristics from larger dimensions features [2]. While, in bottom-up approaches molecular or atomic components are manipulated and built up into more complex nanoscale assemblies based on multifaceted mechanisms and technologies [3]. In other words, this approach uses atoms or small molecules as building blocks of multi-level structures. This approach is particularly promising as it could lead to no-waste materials.

1.2 Nanofabrication techniques

To date, numerous top down and bottom-up nanofabrication technologies such as lithography techniques, electrospinning, phase separation, self-assembly processes, thin film deposition, chemical vapor deposition (CVD), and laser ablation, are available to synthesize nanostructures (Figure 1.1 [4–7]).

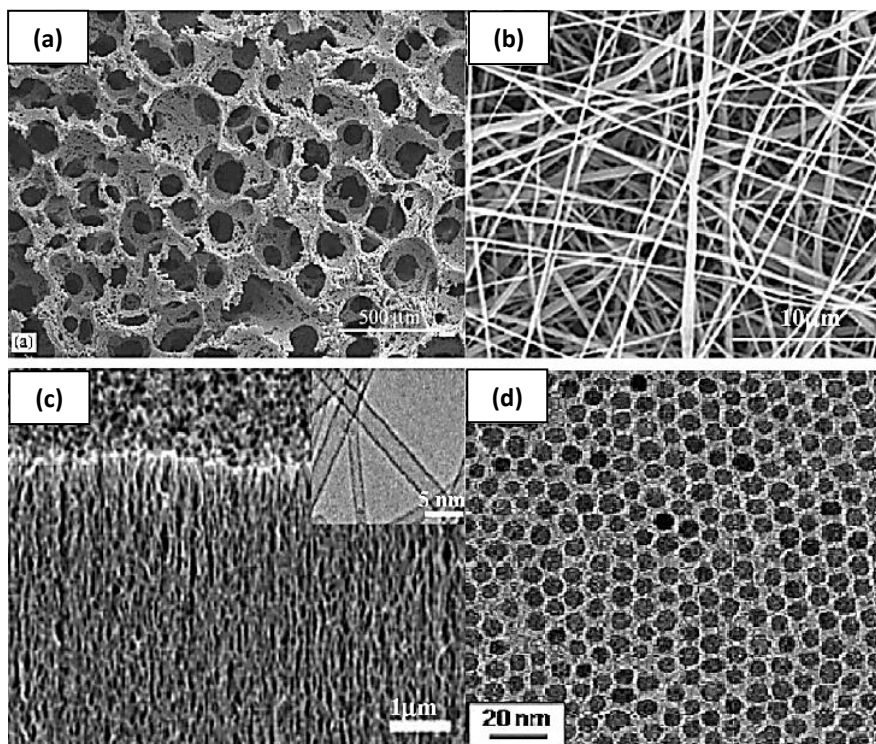


Figure 1.1 (a) SEM image of poly L-lactic acid (PLLA) porous scaffold fabricated by phase-separation technique [4]. (b) Electrospun nanofibers [5]. (c) Aligned single wall carbon nanotube (SWCNT) grown with water-assisted chemical vapor deposition [6]. (d) TEM image of monodispersed magnetic nanoparticles deposited from hexane dispersion and dried at room temperature [7], image modified from [1].

Among nanostructures, nanofiber and nanotube architectures of high surface-to-volume ratios show functional and unique properties compared to that of their bulk counterparts. High surface area, surface roughness, and surface-to-volume ratios of these structures lead to superior physiochemical properties (i.e., mechanical, electrical, optical, catalytic, magnetic properties, etc.) [8]. They can be used for a number of applications such as gas sensors, solar cells, implants surface modifications, tissue engineering, implantable drug delivery systems, and other medical devices [9–12]. Nanotubes have been synthesized by several techniques such as anodization [13], template-based synthesis [14], sol-gel [15], and hydrothermal synthesis [16]. Among them, anodization continues to excite interest due

to the simplicity of material preparation, as well as more control over the synthesis process in comparison with other methods.

1.2.1 Anodization technique

The fabrication of the titania nanotubes using anodization includes two steps. In the first step, which is basically a pretreatment, a Ti foil is anodized at several voltages for a period of time which leads to formation of a layer of nanotubes on the foil surface. Then, the nanotube layer is removed ultrasonically in deionized water, and the glossy underlying Ti is exposed. The pattern left on the foil surface after the removal of the nanotube layer is the key player in the further growth of well-aligned nanotubes. In the second step of the anodization, the pretreated Ti foil is used as the anode. After the conclusion of the two-step anodization, the sample is cleaned ultrasonically in ethanol and finally rinsed subsequently in deionized water and ethanol.

In anodization, a multistep process is needed; material preparation is also comparatively complex owing to long process and high temperature [17]. Furthermore, the as-anodized nanotubes are amorphous and a high temperature annealing step is required to form the crystalline phase [18].

1.2.2 Electrospinning technique

Electrospinning gained substantial academic attention in the 1990s, which was partially initiated by the activities of Reneker's group. The schematic diagram for a typical electrospinning apparatus is depicted in Figure 1.2 [19]. Briefly, the basic electrospinning

process uses a polymeric solution driven from a syringe into a needle by a syringe pump. A high voltage is applied to the syringe needle, causing the surface of the drop to distort into the shape of a cone, which is known as the Taylor Cone. When a critical voltage is exceeded, a jet of solution erupts from the apex of the cone and is accelerated toward the electrically grounded target by the macroscopic electric field. As this jet travels through the air, the solvent evaporates leaving behind a polymer fiber (via electrospinning) or polymer nanoparticles (via electrospray) to be collected on an electrically grounded target. Although, electrospinning has been used to generate composite metallic nanofibers, it is limited mostly to polymer nanofibers. Other disadvantages of electrospinning are limited control over generating 3-D structures and using organic solvent.

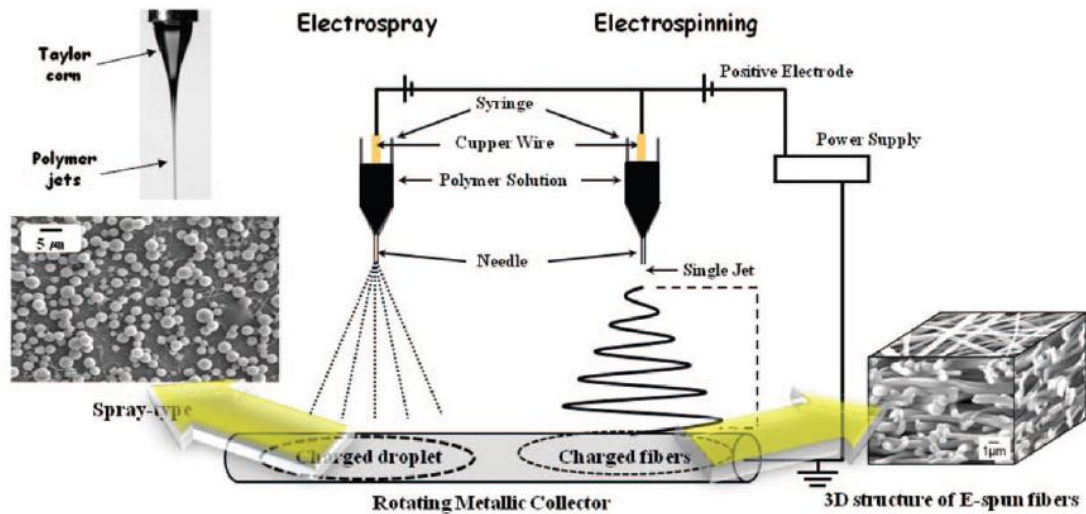


Figure 1.2 Schematic showing the electrospinning process, taken from [19]

1.2.3 Laser ablation technique

Ultrashort pulsed laser ablation is a promising bottom-up nanofabrication technique to generate porous nanofibrous structures due to its simplicity in equipment

configuration, high speed, and low investment. Ultrashort pulsed lasers have been extensively utilized over the last years, and their rapid development has opened a wide range of new applications in numerous areas such as surface micromachining, laser nanofabrication, analytic sampling, thin film deposition, microelectromechanical systems (MEMS) & nanoelectromechanical systems (NEMS) fabrication, and biomedical applications [20–28]. Ultrashort lasers are capable of generating very high peak intensity and rapid deposition of energy into the material. The pulse duration in the ultrashort laser interaction with a solid target appears to be shorter than all characteristic relaxation times including electron heat conduction time, electron to ion energy transfer time, and consequently hydrodynamic or, the expansion time [29]. Hence, target density remains almost constant during the laser pulse. An important advantage of material ablation with ultrashort laser pulses over nanosecond pulses is that there is little or no collateral damage in dielectric materials [30], and minimized heat affected zone (HAZ) in metals [31] because of the thermal effects produced in the material being processed. Furthermore, plasma shielding of succeeding laser beam with ablated material is prevented in ultrashort lasers leading to maximum absorption efficiency [32].

Ultrashort pulsed laser machining is a feasible tool for high resolution machining of different materials including metals, semiconductors, dielectrics, polymers, and biological tissues [25], [29], [33–35]. In addition, this process offers high precision, flexibility of pattern design, and non-contact machining, that makes it robust technique for various applications [36–41]. In addition, ultrashort laser material processing is a convenient, cost-effective process as, unlike most of other techniques, it does not typically require clean

room conditions to perform perfect machining. For instance, in chemical wet etching, tiny dust particles could block photoresist exposure which results in corresponding pattern errors. In ultrashort pulsed laser machining, such particles are evaporated by absorbing insignificant slight amounts of energy and with no effects on the precision of the machining process. Additional advantages of ultrashort laser processing are single-step and flexibility of design.

In studies described in this dissertation, femtosecond laser material processing is developed and employed to synthesize nano/micro architectures to evolve biomedical device fabrication and other biomedical applications. Synthesized structures include nanofibrous platforms, membranes, and microchannels. These synthesized structures require machined features in materials that are impossible or challenging to produce by conventional fabrication approaches due to limited applicability of fabrication and/or material property. For instance, synthesis of three-dimensional (3-D) nanofibrous structures requires a femtosecond megahertz-pulse repetition laser and it cannot achieve using kilohertz-pulse nanosecond lasers. In the material point of view, Natural organic biomaterials such as eggshells are hard, brittle, and easy to burn. Conventional lasers and other approaches are not capable of fabricating 3-D nanostructures on them because the tool itself limits the process. However, direct write femtosecond laser ablation can be performed to generate 3-D nanostructures on natural biomaterials in an ambient condition with minimal thermal effect on their surface.

1.3 Nanostructured materials

1.3.1 Synthetic materials

1.3.1.1 *Titanium (Ti)*

Nanostructures have recently drawn great attention due to the exceptional physical, optical, and chemical properties they present compared to those of their bulk counterparts which can be utilized for the development of different technological applications.

In particular, titanium dioxide (titania) nanostructures have attracted lots of interest due to their outstanding mechanical and thermal properties, biocompatibility, and corrosion resistance [42], [43]. They have been widely exploited in numerous technologies including implantable drug delivery systems, biosensors [44], [45], solar cells [46], [47], photocatalysis [48], [49], tissue engineering [40], [50], and other medical devices [45], [51]. Titania nanotube films have been widely recognized as growth support substrates for bone and stem cells, for prevention of bacterial adhesion, and enhancing blood clotting to control of haemorrhage. Recent *in vivo* and *in vitro* studies have demonstrated that surfaces comprised of nanotube platforms exhibit additional biological effects by producing integration between oxide and apatite nanocrystals and also by improving the cell-material interaction [52–55].

Various preparation techniques have been developed for the synthesis of titania nanostructures, such as anodization [56], chemical vapour synthesis [57], hydrothermal methods [58], so-gel [15], and template-based synthesis [14]. However, these traditional routes have disadvantages such as expensive precursors, long processing time, and

uncontrollable phase transformation during chemical routes [52], [59]. These drawbacks seem to be harmful to titania nanostructure practical applications.

Laser ablation has proven to be an effective technique for synthesis of nanostructures of various shape and internal structure on different materials [60], [61]. Extensive studies have been reported on synthesis of different titania nanostructures such as nanoparticle, nanotube, nanofibers, nanorod and nanowires using laser ablation [15], [35], [52], [62]. However, Special conditions are often required to promote a particular type of structure to grow. For instance, the synthesis of nanotube using a low-repetition-rate nanosecond laser needs to be performed in a furnace with high controlled temperature and under continuous noble gas stream as the laser plume cools down after the pulse below the minimal temperature required for the nanotube formation. In respect to tissue regeneration, 3-D porous structures would be especially more promising for scaffolding systems than one-dimensional nanotubes owing to their porous and interwoven structure. The merits of a surface comprised of interwoven ultrafine nanofibrous structures would be high porosity, variable pore-size distribution, high surface to volume ratio and most importantly, morphological similarity to extracellular matrix (ECM) [63]. The introduction of megahertz-repetition rate femtosecond lasers along with a better understanding of the physics of ultrashort laser-matter interaction have allowed the synthesis of nanostructures which previously couldn't be produced by traditional long laser pulses. However, up to now, there have been no reports on synthesis of 3-D titania nanofibrous structure using femtosecond laser ablation.

1.3.1.2 ***Silicon (Si)***

Due to high chemical & thermal stability and bioinertness, silicon is an appealing substrate for microfluidic and biomedical devices. Previous researches suggest that fabricated silicon membranes are inert and relatively nontoxic [64]. In addition, good mechanical strength of silicon membranes facilitates their utilization in pressurized filtering devices at macro- and micro-scale as well as harsh environments [65]. Silicon nanostructures have recently attracted great attention in tissue regeneration research as they are biocompatible and biodegradable.

1.3.1.3 ***Silver (Ag)***

Silver compounds have been widely used for both hygienic and healing purposes for decades [66]. Recently, silver nanostructures have become the center of attention as they show remarkably improved physicochemical and biological characteristics compared to their bulk counterparts [67]. Silver nanostructures have been used for the treatment of wounds and burns and also marketed as a water disinfectant and room spray [67]. However, their *in vivo* toxicity is a crucial aspect that needs to be assessed when they are considered for therapeutic and diagnostic purposes [68]. Up to now, few *in vivo* studies have been performed, and therefore, through studies on the cytotoxicity, antibacterial characteristics, bio-distribution, degradation, and possible adverse effects of silver nanoparticles are required.

1.3.2 Natural materials

1.3.2.1 *Eggshell*

Autogenous bone has been long considered the ideal grafting material in bone reconstructive surgery owing to its osteogenic, osteoinductive and osteoconductive properties [69], [70]. However, harvesting the autogenous bone requires an additional surgery which increases morbidity at the donor site and extends the operation period [71], [72]. Therefore, a variety of new bone grafting materials has substituted for autogenous grafts thanks to recent advances in biotechnology. Among them, natural bone substitute biomaterials from bovine sources and bone-like minerals (calcium carbonate) derived from corals or avian eggshells, have been preferred due to their biodegradability, abundance and lower price in comparison with synthetic biomaterials [73–77]. The coralline calcium carbonate (calcite), which is totally resorbable and biocompatible and shows good osteoconductivity, has been used as an effective bone substitute in the natural form or converted to hydroxyapatite (HA) in bone healing in dentistry and orthopedic [72], [78–81].

Avian eggshells, with a mineral composition similar to corals, has been introduced as a potential bone substitute in maxillofacial and craniofacial surgery as they could easily be acquired and contain ions of Strontium (Sr) and Fluorine (F) [72], [82], [83]. One of the crucial characteristics to be considered when using a bone substitute graft is its degradation rate due to the fact that it may have effects on the long-term results. The graft should undergo only minimal resorption if it is applied as an onlay graft whereas a resorbable one is desirable when a bone substitute is used as an interpositional graft or in a

peri-implant defect [82]. Eggshell, which can be manufactured under powdered or block form, can be used for both indications.

Many *in vitro* and *in vivo* studies have shown that the microporous surface structure and biodegradability of bone substitutes play critical roles in bone healing. It is indicated that cell attachment and proliferation are improved on nanostructure surface than microstructure one [84].

Of the nanoscale structures, randomly interwoven nanofibrous structures are particularly preferred for scaffolding systems in comparison with nanoparticles due to their continuous structure. There are reported studies where eggshell has been used to compose different Ca-precursor nanoparticles or HA nano-powder that requires the additional step such as sintering to synthesize porous surfaces [83], [85]. However, no studies on synthesizing 3-D nanofibrous structure on natural biomaterials have been accounted so far. Therefore, a simple method to generate 3-D nanofibrous structure from eggshell in a single-step would be in a great interest.

1.3.2.2 ***Rice husk and Wheat straw***

Silicon is the second most abundant element in soil [86]. As a result, plants rooting in soil always have trace of silicon in their tissues. Particularly in the Poaceae species, which are also called Gramineae or true grasses, aqueous silicic acid, $Si(OH)_4$, is taken up by the roots and transported into the plant through the transpiration stream [87]. Polymerization then takes place as a consequence of the increase of the concentration of silicic acid through transpiration. Once the polymerization process finished, silicon is deposited in extracellular and intercellular structures of the plant in the form of phytoliths

which is a porous opal ($SiO_2 \cdot nH_2O$) [86]. This deposited phytoliths can be used as a low-priced Si precursor to formulate nanostructured silica [88], [89].

Thus far, nano-silica materials have been prepared by several methods including vapor phase reaction, sol-gel, and thermal decomposition technique [88], [90], [91]. However, their high cost of preparation has limited their wide application.

Rice husk and wheat straw belong to the Poaceae family containing high concentrated silica. Their ashes contain $> 90\%$ silica by mass with minor amounts of metallic elements which make them most economical sources of nanoscale silica in the future.

Although there have been several studies on generating nano-scaled silica nanoparticles, no study has been reported on synthesizing 3-D micro/nanofibrous structures on rice husk and wheat straws. Therefore, a simple method to synthesize 3-D micro/nanofibrous structure in a single-step would be in a great interest. These structures could be used for the graft surface modification, or as a structural support and component.

1.4 Research objective

As femtosecond laser processing is a fairly new technique, there is still a lack of knowledge about both the laser ablation characteristics of many materials and the potential structures could be synthesized using this technique. Particularly, most of the studies reported so far on the femtosecond laser-material interaction have been performed in vacuum as the ablation mechanism is much more complicated at atmosphere conditions [92–94]. Therefore, further studies to develop knowledge of laser-material interaction are

required to shed light on laser ablation mechanism at ambient condition and also to develop novel functional nanostructures. Moreover, experimental studies are needed to examine the functionality of the synthesized nanostructures for different applications, in particular biomedical application. The presented research in this dissertation aims to cover abovementioned required studies. The main objectives of the dissertation can be highlighted as follows:

- **Theoretical and experimental analyses of femtosecond laser ablation mechanism and nanostructure formation in the presence of ambient air**
- **Development of bio-functionalized platforms with 3-D nanostructure layer and study the *in vitro* bioassay of synthesized platforms**

1.5 Organization of the dissertation

Chapter 2 reviews the mechanism of ultrashort laser interaction with metallic and semiconductor targets in vacuum and the presence of background gas. Also, it presents the theoretical background of ablation mechanism, evaporation rate, and surface temperature for single pulse ablation of materials.

Chapter 3 describes the experimental set up, materials, and methods of characterization used through this dissertation.

Chapter 4 introduces the fabrication of porous nanofibrous platforms on different biocompatible synthetic and natural materials including titanium, eggshell, rice husk, and wheat straw substrates. These platforms have a potential use as supporting 3-D structures

for cells implanted or seeded in a damaged tissue to help its reconstruction. This chapter also studies a fundamental study which experimentally and theoretically demonstrates the formation mechanism of web-like 3-D nanofibrous structures during femtosecond laser ablation of Ti target in the presence of air.

Chapter 5 demonstrates the potential use of the presented technique for fabricating integrated nanostructures on transparent platforms as well as inside microstructures toward device fabrication. Presented studies show that integrated nanostructure inside microchannels can be fabricated in one single step using this technique. In addition, femtosecond laser induced reverse transfer (LIRT) is used for controllable site-specific deposition of nanostructure on transparent platforms. This method may find wide applications to synthesize nano-composite, fabricate porous filters, construct tissue scaffolds, and generate electromagnetic radiation shields for nano-devices, just to name a few.

Chapter 6 presents *in vitro* bioassay studies on fabricated Ti platform. Bioactivity of the platforms is assessed using simulated body fluid (SBF). Also, the interaction of nanofibrous scaffolds with living cells has been examined using different *in vitro* assays. Cell-based assays such as cell adhesion, cell proliferation, and cell viability tests are carried out to evaluate the biocompatibility between cells and implanted platform.

Chapter 7 summarizes the main results obtained in this dissertation and proposes future avenues of research.

CHAPTER 2

PHYSICS OF ULTRASHORT LASER INTERACTION WITH SOLIDS

Over the past several years the interaction of sub-picosecond ultrashort pulsed laser with materials has been an active area of materials science research. A sub-picosecond laser pulse has pulse duration shorter than all major material characteristic relaxation time: the electron-to-ion energy transfer time, the electron heat conduction time, and the hydrodynamic or, the expansion time. Therefore, ultrashort pulses only excite electrons, leaving the lattice cold during the laser-target interaction. For this reason, the ultrashort laser pulse interacts with a solid target with a density constant during the laser pulse. In our experiments we study a wide range of intensity from peak intensity of 10^{11} W/m^2 to high intensity of 10^{13} W/m^2 . For instance, irradiated with pulses with peak intensity of 10^{17} W/m^2 , silicon is estimated to reach temperature of $\sim 10^4 - 10^5 \text{ K}$, more

than the surface temperature of the sun, while still retaining the density of a solid [95]. The development of such high temperature and pressure in the material can lead to non-equilibrium phase transformations as well as the formation of new materials [29], [94]. This chapter brings the mechanism of ultrashort laser interaction with metallic and semiconductor targets in both background gas and vacuum. Also, it presents the theoretical analyses of ablation mechanism, evaporation rate, and surface temperature for single pulse and multiple pulse machining. Finally, it discusses the mechanism of nanoparticle aggregation and nanofiber generation.

2.1 Mechanisms of ablation by ultra-short laser pulses

A sub-picosecond laser pulse has pulse duration shorter than all major material characteristic time, i.e., the electron-to-ion energy transfer time, the electron heat conduction time, and the hydrodynamic or, the expansion time. Therefore, ultrashort pulses only excite electrons, leaving the lattice cold during the laser-target interaction [29]. For this reason, the ultrashort laser pulse interacts with a solid target with a density constant during the laser pulse.

The main process during the ultrashort pulsed laser-material interaction is considered to be only electron heating by the laser electromagnetic field. If the total energy of an electron exceeds its Fermi energy, which is a sum of the binding energy ε_b and work function ε_{wf} , it can escape from the target. Consequently, the generated electric field of the charge separation will drag the ions out of the target surface. The kinetic energy of an atom (ion) needs to be higher than the energy of vaporization of the atom ($\varepsilon_{kin} = \varepsilon_{tot} - \varepsilon_b > 0$)

allowing it to escape the solid. Depending on laser pulse duration, transferred energy intensity to the target, electron-to-ion energy transfer time, and ambient environment, three major ablation mechanisms can be considered [29], [96].

First, at very high energy intensity an extreme non-equilibrium and non-thermal mechanism of material removal, the electrostatic ablation, can occur if the electron temperature surpasses the Fermi energy as mentioned earlier. The second ablation mechanism, the non-equilibrium ablation, can take place if electrons deliver energy in excess of the ions' binding energy just before thermodynamic equilibrium can be established (i.e. before the time period needed for building up the high-energy tail in the Maxwell distribution through Coulomb collisions). Finally, thermal evaporation may occur through ion-ion collisions establishing full equilibrium distribution. In either indicated mechanism, energy in excess of binding energy requires to remove an atom (ion) [97].

2.1.1 Ablation threshold in vacuum

The ablation threshold can be defined as a minimum amount of energy required to initiate the material removal process. The material removal process at the ablation threshold depends on the energy distribution in a surface thin layer which is called skin layer l_s . The skin layer, absorption length, is inversely proportional to the imaginary part of the refractive index, $\varepsilon = (n + ki)^2$, and can be defined as follows [98]:

$$l_s = c/2\omega k = \lambda/4\pi k \quad (2.1)$$

where, ω is laser frequency and k is imaginary part of material refractive index (absorptive index).

The energy distribution is accountable for the contribution of non-equilibrium ablation or/and thermal evaporation. In addition, the establishment of the energy distribution in the skin layer is strongly influenced by the ambient condition, i.e., if the ablation happens in vacuum or in the presence of an ambient gas. If the absorbed energy in the skin layer exceeds the electron threshold energy, free electrons can escape a solid target during the pulse duration. As a result, a strong electric field is due to charge separation with the parent ions.

2.1.1.1 *Ablation threshold for metals*

As abovementioned, the minimum energy an electron needs to leave a solid target must be comparable to the work function. The electron also requires additional energy equal to an ion binding energy to pull ions out of the target. Therefore, the ablation threshold for metal targets proceeds if the electron energy of free electrons in the skin layer by the end of the laser pulse surpasses the Fermi energy. The energy condition at the end of the pulse can be expressed through electron temperature in the skin layer [29]:

$$\varepsilon_e = \varepsilon_b + \varepsilon_{wf} = \frac{4AF_0}{3l_s n_e} \quad (2.2)$$

Then, the laser threshold fluence for ablation of a metal target can be expressed as the following:

$$F_{th}^{metal} \equiv F_0 = \frac{3l_s n_e}{4A} (\varepsilon_b + \varepsilon_{wf}) \quad (2.3)$$

It should be noted that the number density of the electrons n_e assumed to be unchanged during the laser-metal interaction process. After insertion of Eq. 2.1 for the skin

layer into Eq. 2.3, the estimated formula for the ablation threshold of a metal target F_{th}^m reads the following form:

$$F_{th}^m \equiv F_0 \approx \frac{3cn_e}{8\omega Ak} (\varepsilon_b + \varepsilon_{wf}) \equiv \frac{3\lambda n_e}{16\pi Ak} (\varepsilon_b + \varepsilon_{wf}) \quad (2.4)$$

where, $F_0 = I_0 t_p$ is incident laser fluence (t_p is the laser pulse duration), n_e is electron number density, and A is laser absorption coefficient of the target. The laser absorption coefficient can be calculated from the Fresnel formulas as follows [99]:

$$A = 1 - R = \frac{4n}{(n + 1)^2 + k^2} \quad (2.5)$$

here, n and k are real part and imaginary part of refractive index of the target material, respectively. In terms of reflectivity of metals, one should note that, it is not enough to use Fresnel's equation as abundance of free electron in metals may affect the electromagnetic waves [100]. Particularly when considering ultrashort laser-metal interaction, other parameters such as beam polarization, laser fluence, number of laser pulses, sample surface roughness, and oxide films on the surface also may influence the reflectivity [101–103].

2.1.1.2 *Ablation threshold for dielectrics*

The ablation mechanism for dielectric targets is considered similar to that for metals. However, several characteristic differences should be borne in mind when predicting laser ablation threshold for dielectrics. First, an extra energy is required to build free carriers (i.e., to transfer electrons from valence band to conductivity band to increase the absorbed energy density to the level required for ablation). Thus, energy equal to the

ionization potential J_i needs to be delivered to valence electrons. Second, the number density of free electrons is governed by the laser intensity and laser pulse during [29]. Nevertheless, if the intensity during the pulse goes beyond the ionization threshold then the first ionization is ended before the end of the laser pulse and the number density of free electrons is saturated at the level equal to the number density of atoms in the target. Considering the abovementioned modifications as well as the fact that the absorption in the ionized dielectric also takes place in the skin layer, the threshold fluence for ablation of dielectric targets F_{th}^d takes:

$$F_{th}^d \equiv F_0 \approx \frac{3cn_e}{8\omega Ak}(\epsilon_b + J_i) \equiv \frac{3\lambda n_e}{16\pi Ak}(\epsilon_b + J_i) \quad (2.6)$$

Thus, as a rule of thumb, the ablation threshold for dielectric targets in the ultrashort laser-matter interaction regime would be higher than that for metals, supposing that all the atoms in the interaction zone are at least singly ionized [104].

2.1.2 Ablation thresholds in ambient gas

Previous studies showed that material ablation in air takes place at lower ablation thresholds in compare of it in the vacuum [98], [105], [106]. Experimental studies suggest that ablation thresholds for several metals in ambient air are less than half of those determined in vacuum [105]. In vacuum, the time required for the bulk-to-surface energy transfer in order to build the high-energy tail is longer than other characteristic relaxation times (e.g. the electron-ion temperature equilibration time and surface cooling time) which hinders thermal evaporation in vacuum [97]. While in air, on the other hand, collisions

between the ambient gas atoms and the surface is believed to significantly decrease the lifetime of the non-equilibrium regime leading to thermal evaporation [94].

Once the laser pulse interacted with the target, the air next to its heated surface collides with the target surface and obtains energy required for the formation of a Maxwell distribution in the air in close vicinity of the target surface. In other words, the presence of air leads to the establishment of a high-energy tail Maxwell distribution in the surface layer increasing the bulk-to-surface energy transfer. Therefore, three different processes are assumed to be acting at the same time which control the ablation conditions at the solid-air boundary [94]: (I) Evolution of the Maxwell distribution at the surface due to air-solid collisions, (II) Evolution of the Maxwell distribution at the surface due to bulk-to-surface energy transfer, and (III) Cooling of the surface by heat conduction.

Mechanism (I) is considered to be the only mechanism that results in to thermal evaporation as the two other process are too slow to lead to the formation of high-energy Maxwell tail as will be explained later [94]. Therefore the presence of air significantly increases thermalization rate reducing the time for building up the high-energy tail at the surface. In this case, the ablation rate can be determined by thermodynamic equilibrium equations which relate the saturated vapor density and pressure to its temperature.

The air-solid equilibrium energy distribution is started by air molecules-solid collisions. Considering the gas-kinetic mean free path in air in standard conditions ($l_{g-k} = 6 \times 10^{-6}$ cm) [107], the equilibration time t_{eq} required to form a Maxwell distribution in air can be estimated to be $t_{eq} \sim 1.8 \times 10^{-10}$ using $t_{eq} \approx t_{g-k} \approx l_{g-k}/v_{th}$. The average thermal velocity v_{th} in air is approximately $v_{th} = 3.3 \times 10^4$ cm/s at room

temperature [94]. According to previous studies, the bulk-to-surface energy transfer time at the maximum temperature for the threshold fluence conditions in air calculated to be $t_{b-s} \sim 30 \text{ ns} \gg t_{eq}$ for several metal targets (i.e. Cu, Al, and Fe) after the end of the pulse [97]. As the bulk-to surface energy transfer time is much longer the air-solid equilibrium time, it is assumed that only the air-surface collisions plays a role for thermal evaporation from the surface.

Thermal evaporation would initiate sometime after the equilibration time $t > t_{eq}$. At this equilibration time the solid-air interface temperature equilibration is completed and continues to fall according to the linear heat conduction law. Hence, after establishing the Maxwell equilibrium at the air-solid interface, the number of atoms ablated per unit area may be estimated by [94]:

$$\langle R_{evp} \rangle_{therm} = \int_{t_{eq}}^{\infty} (R_{evp})_{therm} dt. \quad (2.7)$$

Assuming the vapor-air mixture with a predominance of air plays the role of the saturated vapor over the ablated solid, the thermal evaporation can be taken as [97]:

$$(R_{evp})_{therm} \approx \frac{n_{air} k_B T_{eq}}{(2\pi M_a k_B T_{eq})^{1/2}} \quad (2.8)$$

Then Eq. 2.1 takes the following form:

$$\langle R_{evp} \rangle_{therm} = \int_{t_{eq}}^{\infty} (R_{evp})_{therm} dt \approx n_{air} \left(\frac{k_B T_{eq}}{2\pi M_a} \right)^{1/2} t_{eq} \left[\frac{atoms}{cm^2} \right] \quad (2.9)$$

It should be noticed that the Eq. 2.3 gives an approximate evaporation rate and a reliable estimate may be achieved with the numerical coefficients taken out from the

known experimental data at the temperature close to the experimental conditions. The solid-air surface equilibration temperature T_{eq} in Eq. 2.9 can be calculated using linear heat conduction law [108]:

$$T_{eq} \approx T_{max} \left(\frac{t_p}{t_{eq}} \right)^{1/2} \quad (2.10)$$

where, T_{max} is the maximum temperature at the end of the laser pulse that could be estimated at the experimentally determined threshold fluence in air. A simple way to estimate the maximum temperature, however, is to consider that the target is heated by a single laser pulse in a heat conduction regime where all losses due to radiation and plume expansion can be neglected. Therefore, the heating process can be modeled as propagation of a heat wave into the target according to the one-dimensional (1-D) heat conduction regime [108], [109]:

$$\frac{\partial T}{\partial t} = a \frac{\partial^2 T}{\partial x^2} \quad (2.11)$$

where,

$$a = \frac{k_h}{C_p \rho_0}$$

Here a is the thermal diffusion coefficient in [cm^2/s]; k_h is the heat conduction coefficient in [$W/(cm K)$], C_p is specific heat [$J/(g K)$], and ρ_0 is target material density in [g/cm^3].

To simplify the problem, one can assume that the laser pulse profile in time has a rectangular shape with a step-like rise and fall: $I = I_a(0 \leq t \leq t_p)$, the target fills the half space at $x > 0$, and the heat flux at the target surface has the same temporal form as the absorbed laser flux. Here I_a is the absorbed laser intensity. Then, the heat conduction Eq. 2.5 with these boundary conditions has an exact solution [108]:

$$T(x, t) = \frac{a^{1/2}}{k_h \pi^{1/2}} \int_0^{t_p} \frac{I_a(\theta)}{(t - \theta)^{1/2}} \exp\left\{-\frac{x^2}{2a(t - \theta)}\right\} d\theta. \quad (2.12)$$

The average temperature of the heated area over space after the end of the laser pulse reads [108]:

$$\langle T \rangle = \frac{1}{(at_p)^{1/2}} \int_0^\infty T(x, t_p) dx. \quad (2.13)$$

Using Eq. 2.6 and 2.7 one can obtain the average temperature as a function of the laser parameters and target temperature:

$$\langle T \rangle = \left(\frac{2}{\pi}\right)^{1/2} \frac{I_a(at_p)^{1/2}}{k_h} = \frac{1}{2^{1/2}} T(0, t_p) \quad (2.14)$$

One should note that the maximum target temperature occurs at the end of the laser pulse, i.e., $T_{max} = T(0, t_p)$.

2.2 Summary

This chapter reviewed the mechanism of ultrashort laser interaction with metallic and semiconductor targets in vacuum and the presence of background gas. Also, it presented the theoretical background of ablation mechanism, evaporation rate, and surface temperature for single pulse interaction with materials.

CHAPTER 3

EXPERIMENTAL SETUP AND PROCEDURE

This chapter describes the experimental setup, materials, and methods of characterization used for the studies in this dissertation. For all the experiments performed in this dissertation, a high power Megahertz femtosecond laser system has been utilized. The physiochemical characterizations of synthesized nanostructures have been investigated by several techniques, e.g. Scanning electron microscope (SEM), Transmission electron microscopy (TEM), X-Ray Diffraction (XRD), which are discussed in this chapter.

3.1 Fabrication system

3.1.1 Experimental Setup

Experiments were carried out with a direct-diode-pumped Yb-doped fiber amplified ultrafast laser system. The laser gives a maximum output power of 16 W with pulse frequency ranging from 200 kHz to 26 MHz (Clark-MXR Inc. IMPULSE Series Ultrashort Pulse Laser). Due to solid state operation and high spatial mode quality of fiber lasers, a Yb-doped fiber-oscillator/fiber-amplifier functions under low noise performance. Moreover, parameters of the laser, such as pulse width, repetition rate and total beam power, are computer monitored, which enables a simple interaction with the performed experiments. The pulse width that the laser can produce ranges between 250 fs and 10 ps. The schematic drawing of the experimental setup is shown in Figure 3.1.

1. Femtosecond laser
2. 1030 nm Mirror
3. F = 500 mm Convex Lens
4. 1030 nm Waveplate
5. F = -150 mm Concave Lens
6. 515 nm Mirror
7. 515 nm Mirror
8. F = -75 mm Concave Lens
9. 515 nm $\lambda/4$ Waveplate
10. F = 300 mm Concave Lens
11. 515 nm Mirror
12. Diaphragm
13. Piezo Scanner
14. EFL = 12478 mm Telecentric Lens
15. Sample and Sample Holder
16. Computer

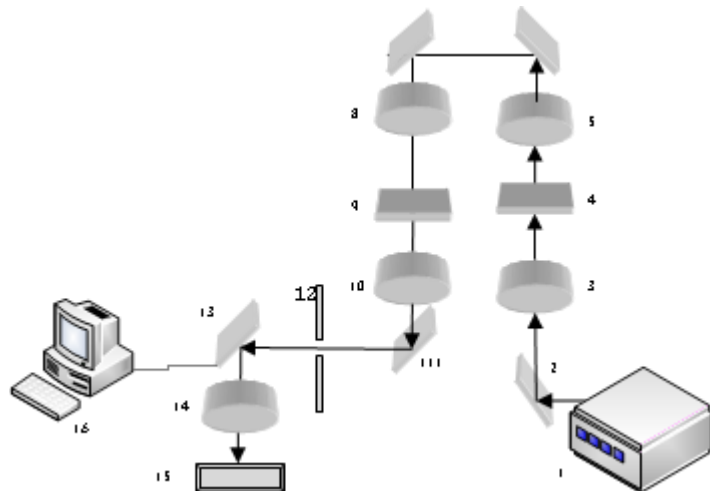


Figure 3.1 Experimental setup

3.1.2 Materials

Titanium nanostructures have attracted lots of interest due to their outstanding mechanical and thermal properties, biocompatibility, and corrosion resistance. They have been widely exploited in numerous technologies including implantable drug delivery systems, biosensors, solar cells, photocatalysis, tissue engineering, and other medical devices. They have been widely recognized as growth support substrates for bone and stem cells, for the prevention of bacterial adhesion, and enhancing blood clotting for control of haemorrhage. Therefore, through the studies in this dissertation, Ti was used as the main material of study for generation of nanofibrous structures as it mainly used for bone tissue regeneration. The synthesized Ti nanostructures also were evaluated using *in vitro* bioassays. For all the studies on Ti target, samples in size of 10×10×0.5 mm were cut from grade 2 (ASTM B265) pure Ti sheet using a diamond saw with oil lubrication. The samples were ground finished to 1200-grit silicate-carbon papers to remove macro-level surface defects and contaminations. Once ground, samples were ultrasonically cleaned in distilled water and dried in desiccators.

Avian eggshells, with a mineral composition similar to corals, has been introduced as a potential bone substitute in maxillofacial and craniofacial surgery as they could easily be acquired and contain ions of Sr and F. They are totally resorbable and biocompatible and shows good osteoconductivity, has been used as an effective bone substitute in the natural form or converted to hydroxyapatite (HA) in bone healing in dentistry and. Hence, for one

of the studies in this dissertation, eggshell was utilized as a natural biomaterial to synthesize nanostructures.

Nanostructured silicon has recently attracted great attention owing to its biocompatible and biodegradable properties. In addition, good mechanical strength of silicon membranes facilitates their application in pressurized filtering devices at macro- and micro-scale as well as harsh environments. In addition to the abovementioned advantages, Si targets, which are supplied in shape of very thin wafers, are easier to work with in terms of manufacturing and characterization. For this reason, Si targets were used for some of the studies in this dissertation where handling or/and characterization of the samples were limited (e.g. cross-sectional imaging is possible with Si target as they are very thin and easy to cut in comparison with Ti targets). The target was a polished silicon wafer with <100> crystal orientation and 550 μ m thickness.

3.1.3 Laser beam delivery

The experiments were conducted using two different optical setups and laser pulses wavelength of 515 nm and 1030 nm depending on the target material and desired synthesized architecture. For instance, light absorption of silicon is higher at laser pulses with wavelength of 515 nm. Also, optical setup with a piezo mirror scanner was used when higher accuracy, steering speed, and control on machining required. On the other hand, optical setup with a Galvo scanner was utilized for higher material ablation and evaporation due to larger spot area.

In the piezo scanner setup, a telecentric lens used to focus the laser beam with 12.478 mm focal length. The theoretical laser minimum spot diameter (D_0) is calculated using $D_0 \approx \frac{1.27\lambda_0 f}{D}$, where λ_0 is the wavelength of the laser, f is the effective focal length of the lens, and D denotes the laser beam diameter. Values for focal length, laser pulse wavelength, and beam diameter are 12.478 mm, 515 nm and 8 mm, respectively. Thus, the theoretical spot size diameter was calculated to be 1.02 μm . The power of the laser beam varied from 100 mW to 200 mW.

In the Galvo scanner setup, the laser beam was expanded to 9 mm by a combination of a plano-convex ($f = -100$) and a plano-concave ($f = 200$) lenses; then the laser beam was rotated to circularly polarized by a quarter waveplate placed in the beam path. The diameter of the beam was decreased to 8 mm using an iris diaphragm just before arriving to galvo scanner. A telecentric lens with a focal length of 63.5 mm was employed to focus the normal beam on the surface of targets (see Figure 3.2). From Eq. 2.12 the theoretical spot size is calculated to be 10.38 μm in diameter when using 1030 nm pulse wavelength. During the experiment the spot size may be bigger due to scatter and misalignment.

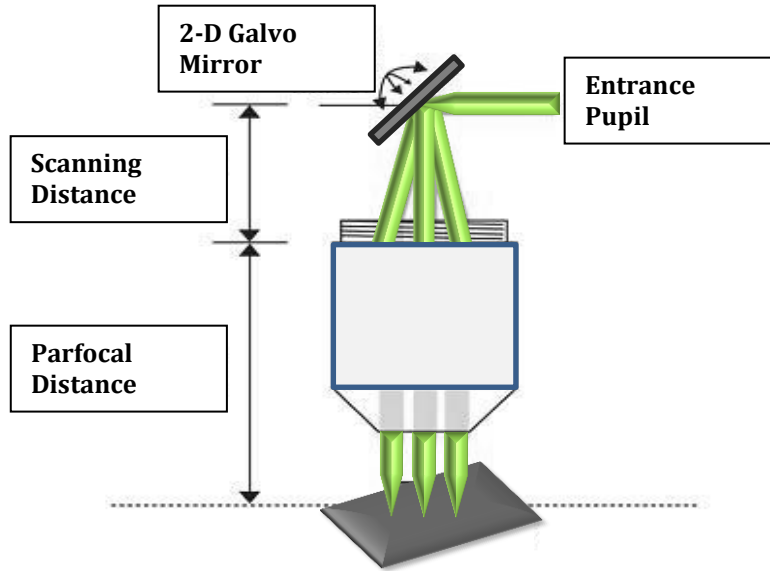


Figure 3.2 Schematic of telecentric scanning lens.

3.2 Surface characterization

3.2.1 Morphology characterizations

3.2.1.1 *Scanning Electronic Microscope (SEM)*

Morphology of nanofibrous structures was characterized using SEM analyses. The SEM uses a focused beam of high-energy electrons to create a range of signals at the surface of target specimens. The generated signals from electron-target interactions give information about the surface external morphology as well as its chemical composition. In most applications, data collected over a selected area of the surface are used to produce a 2-dimensional (2-D) image that displays spatial variations in these properties.

A beam of accelerated electrons generated at the top of the microscope by an electron gun travels to a vertical path through the microscope, which is held within a

vacuum chamber. The beam goes through several electromagnetic fields and lenses, which focus the beam down toward the surface of a sample. Once these high energy electrons hit the surface of the sample, they are decelerated and a variety of signals are generated from the electron-sample interaction. These signals include secondary electrons, backscattered electrons (BSE), diffracted backscattered electrons, photons, visible light, and heat. Secondary electrons and backscattered electrons are generally used for imaging samples. Secondary electrons are mostly employed to display morphology and topography of a surface of samples and backscattered electrons are usually used to show contrasts in composition in multiphase samples (i.e. for rapid phase discrimination). X-ray is generated by inelastic collisions of the incident electrons with electrons in discrete shells of atoms in the sample. As the excited electrons return to lower energy levels, they emit X-rays which are of a fixed wavelength. Therefore, the emitted X-rays are characteristic for each element in a sample excited by the electron beam. The x-rays generated by electron interactions do not lead to volume loss of the sample which makes SEM analysis non-destructive to material to be tested [110], [111].

3.2.1.2 *Transmission electron microscopy (TEM)*

Nanoparticle aggregation and size of a nanofiber were studied using TEM analyses. In order to separate the nanostructures from the substrate, samples were immersed in isopropanol solution and ultrasound vibration was applied. Then a drop of the nanofiber-dispersed solution was placed on the copper meshes and allowed to dry in desiccators.

The TEM functions on the same basic principles as the light microscope but uses electrons beam instead of light. TEMs use electron beams as light source and their much

lower wavelength (wavelength of accelerated electron is about 6pm) enables imaging at resolutions thousand times better than with a light microscope. In TEMs, a high energy electron beam is transmitted through a very thin sample to image and analyze the microstructure of materials in order of atomic scale resolution. The electrons are focused on samples using electromagnetic lenses. Then, the image is observed on a fluorescent screen, or recorded on film or digital camera. Although, the accelerated high energy electrons have a wavelength in order of 0.025 Å, the resolution of the electron microscope is limited by aberrations inherent in electromagnetic lenses, to about 1-2 Å [112].

3.2.2 Chemical and phase characterizations

3.2.2.1 *Energy dispersive X-ray spectroscopy (EDS) analyses*

EDS is an analytical technique utilized to study the elemental analysis or chemical characterization of a sample. It relies on the investigation of an interaction of some source of X-ray excitation with a sample. The fundamental principle of EDS is that each element has a distinctive atomic structure which allows unique set of peaks on its X-ray spectrum.

3.2.2.2 *X-ray Diffraction (XRD) analyses*

Phase analysis of the synthesized structures was performed using X-ray Diffraction (XRD). The x-ray source was a Cu $k\alpha$ rotating anode generator with parallel focused beam and 3-circle diffractometer with a 2D detector. The average wavelength of the x-rays was 1.54184 Å. Phi scans with widths of 60° were done with the detector at four different swing angles for each sample in order to get a profile with a 2 θ range of 10.5-104°.

X-ray diffraction works based on constructive interference of monochromatic X-rays and a crystalline sample. The interaction of the incident rays with the sample creates constructive interference and diffracted X-rays. The diffracted X-rays are then detected, processed and counted. By scanning the sample through a range of 2θ angles, all possible diffraction directions of the lattice is collected due to the random orientation of the powdered material. Conversion of the diffraction peaks to d-spacing allows identification of a mineral as each mineral has a set of identical d-spacing. Generally, the identification process is completed by comparison of the acquired d-spacings with standard reference patterns.

3.2.3 Physiochemical characterizations

3.2.3.1 *Atomic force microscopy (AFM)*

The AFM, in contact mode, was implemented to measure the interaction forces. Nanoprobe single crystal silicon (N-type) cantilevers (Model CSG10 series) was purchased from NT-MDT Co. The radius of tip curvature was less than 10nm. Six force measurements were made at each location, then three locations were chosen for the force measurement on each sample, and an average value was taken. Force curves (tip deflection versus piezo position) were obtained after the force measurement. The adhesion force was calculated assuming the force was a linear function of the probe displacement relative to the sample surface along Z-axis. Tip deflection data were converted to force (in NanoNewtons) by multiplying by the spring constant of the cantilevers according to Hooke's law: $F = k \cdot \Delta H$, where ΔH is the cantilever deflection and k is the cantilever spring constant (N/m). The manufacturer's value for the spring constant of the cantilever is $0.11 N/m$.

3.2.3.2 *Contact angle measurement*

The wetting properties of the nanofibrous layer were studied by dynamic contact angle measurements. Samples were fixed and a droplet of distilled water was applied to the surface. Images of each drop on the surfaces were recorded using a digital microscope. The contact angles were determined from the images using axisymmetric drop shape analysis profile (ADSA-NA) methodology [113]. The mean value of the contact angles was calculated from five individual measurements taken at different locations on the substrates.

3.2.3.3 *Zeta potential (ZP)*

The zeta potential test (Zetasizer Nano-ZS90; Malvern Instruments, UK) was used to characterize the physio-chemical parameters at the solid and liquid interface. In this test the zeta potential characterized the surface of the wafer by measuring the stability of the nanostructures on the titanium surface. If the ZP is high it signifies repulsive forces and stability at the surface and if it is low it shows attractive forces and instability. In order to measure the zeta potential of the nanostructures the ablated surface was carefully scratched using a surgical blade to separate it from the titanium wafer. The particles were then collected in an eppendorf tube and mixed well with 1mL of de-ionized distilled water. The solution was mixed well to prevent the aggregation of the nanoparticles. The mixture was then transferred to a cuvette and the measurement was taken.

CHAPTER 4

STUDY OF THE FORMATION OF 3-D NANOSTRUCTURE PLATFORMS

This chapter demonstrates the fabrication of porous nanofibrous platforms on different biocompatible synthetic and natural materials including titanium, eggshell, rice husk, and straw wheat substrates. These platforms have a potential use as supporting 3-D structures for cells implanted or seeded in a damaged tissue to help its reconstruction. It also consists of a fundamental study which experimentally and theoretically demonstrates the formation mechanism of web-like 3-D nanofibrous structures during femtosecond laser ablation of Titanium (Ti) target in the presence of air.

4.1 Laser Processing of Synthetic Material: Study of the ablation mechanism of Ti¹

The introduction of megahertz-repetition rate femtosecond lasers along with a better understanding of the physics of ultrashort laser-matter interaction have allowed the synthesis of nanostructures which previously couldn't be produced by traditional long laser pulses. It allows eliminating additional heating and the need for the ambient gas in the chamber [114]. Also, the interaction of femtosecond laser pulses with materials results in reduced thermal effects compared to nanosecond-pulsed lasers. Femtosecond laser pulses heat materials to higher pressure and temperature than do longer-pulse lasers of comparable fluences as the energy is delivered before significant thermal conduction happens in the materials [29], [108]. Therefore, a femtosecond laser pulse can heat any material to a solid-density plasma state with temperature and pressure above the critical point. This leads to generation of high density plume which leads to nanoparticle aggregation after plume condensation.

This section demonstrates the mechanism of ablation of solids by multiple femtosecond laser pulses in ambient air in an explicit analytical form. The formulas for evaporation rates and the number of ablated particles for laser ablation by a single pulse as well as multiple pulses as a function of laser parameters, background gas, and material properties are predicted and compared to experimental results. The calculated dependence

¹ Reprinted from Journal of Applied Physics, 113(2), A. Tavangar, B. Tan, and K. Venkatakrishnan, Study of the Formation of 3-D Titania Nanofibrous Structure by MHz Femtosecond Laser in Ambient Air, pp. 023102-023110, Copyright (2013), with permission from American Institute of Physics. The dissertation author was the primary investigator and author of this article.

of the evaporation rate on the pulse repetition and laser pulse dwell time is in accordance with the experimental data. Later, the formation mechanism of the nanofibrous structures during femtosecond laser ablation of targets in the presence of air is discussed. The results indicate that femtosecond laser ablation of solids at air background yields crystalline nanostructures. The formation of crystalline nanostructures is preceded by thermal mechanism of nucleation and growth. It also demonstrates the formation of nanofibrous structures by applying an existing simplified kinetic model to Ti target and ambient condition.

4.1.1 Ablation mechanism by a single ultrashort laser pulse in ambient gas

As mentioned in the previous chapter, material ablation in air takes place at lower ablation thresholds in compare of it in the vacuum. It was reported that in the presence of air background, collisions between the ambient gas atoms and the surface decreases the lifetime of the non-equilibrium regime leading to thermal evaporation. Once the laser pulse interacted with the target, the air next to its heated surface collides with the target surface and obtains energy required for the formation of a Maxwell distribution in the air in close vicinity of the target surface. In other words, the presence of air leads to the establishment of a high-energy tail Maxwell distribution in the surface layer increasing the bulk-to-surface energy transfer. It was assumed that only the air-surface collisions plays a role for thermal evaporation from the surface as the bulk-to surface energy transfer time is much longer the air-solid equilibrium time.

After establishing the Maxwell equilibrium at the air-solid interface, the number of atoms ablated per unit area can be estimated by Eq. 2.9. Using the solid-air surface equilibration temperature Eq. 2.10 as a function of maximum temperature T_{max} , one can predict the laser evaporation rate as follows:

$$\langle R_{evp} \rangle_{therm} \approx n_{air} \left(\frac{k_B T_{max}}{2\pi M_a} \right)^{1/2} (t_p t_{eq})^{1/2} \left[\frac{atoms}{cm^2} \right] \quad (4.1)$$

where, T_{max} is the maximum temperature at the end of the laser pulse that can be written from Eq. 2. 14 as follows:

$$T_{max} = \frac{2I_a (at_p)^{1/2}}{k_h (\pi)^{1/2}} \quad (4.2)$$

The absorbed laser intensity on the target surface $I_a = AI_0$ can be obtained by having the intensity of incident pulse and laser absorption coefficient.

The intensity of the incident laser pulse (I_0) can be calculated by measuring the average power P_{ave} as follows:

$$I_0 = \frac{P_{avg}}{R_{rep} t_p A_{foc}} \quad (4.3)$$

Here, P_{avg} is average power (in W), measured directly from incident laser pulse, R_{rep} (in s^{-1}) is laser repetition rate and A_{foc} (in cm^2) is the irradiation focal spot area which can be obtained by calculating the theoretical laser minimum spot diameter (D_0) as follows [109], [115]:

$$D_0 \approx \frac{1.27\lambda_0 f}{D} \quad (4.4)$$

λ_0 is the wavelength of the laser, f is the effective focal length of the lens, and D denotes the laser beam diameter.

Using Eq. 4.2 and Eq. 4.3, one can estimate the maximum temperature as a function of laser parameters:

$$T_{max} = \frac{2AP_{avg}a^{1/2}}{k_h R_{rep} A_{foc} (\pi t_p)^{1/2}} \quad (4.5)$$

Then, the evaporation rate for a single pulse can be expressed by substituting Eq. 4.5, into Eq. 4.1 as follows:

$$\langle R_{evp} \rangle_{therm} \approx n_{air} \left(\frac{k_B a A t_{eq}^{3/2} P_{avg}}{M_a k_h \pi^{3/2} R_{rep} A_{foc}} \right)^{1/2} \left[\frac{atoms}{cm^2} \right] \quad (4.6)$$

The first part in the bracket depends on target material properties, while the second part shows the evaporation rate dependency on the parameters of laser process.

4.1.2 Ablation rate in case of multiple laser pulses

One single ultrashort high intensity pulse would evaporate relatively a limited number of atoms per pulse [116]. However, for practical and industrial application laser systems with high average ablation rate are required [117]. For this reason, nowadays, laser systems with high pulse (MHz) repetition rates are utilized to attain a high average ablation rate. For instance, high repetition rates up to 100 MHz would retain the atomic

flow into the plume at levels of $10^{19} - 10^{20}$ atom/s which is suitable for nanostructure formation/deposition and micro/nano-processing applications [97]. In addition to aforementioned, if the maximum intensity of a single pulse merely slightly surpasses the ablation threshold, then the plume produced by such a pulse contains a mixture of phases as a single laser pulse at a target generates a Gaussian intensity distribution across the focal spot. Therefore, in order to control the phase state of the evaporated plume, the spatial intensity distribution needs to be improved. By scanning a target by a high repetition rate pulses (MHz), multiple pulses hits the same spot and spatial intensity distribution over the target surface integrates over time. As a result, the evaporation conditions become almost homogeneous and all the imperfections of a single beam are smoothed down.

Using MHz repetition rates, the focused laser beam can dwell at a particular spot on the target for times longer than the time gap between the pulses. Therefore, multiple laser pulses arrive at the same spot on the target surface, depends on the laser pulse dwell time (D_t), which leads to incubation of heating and evaporation process.

Now to define the number of evaporated atoms after multiple laser pulses, one should consider the number of pulses arrive at the same spot on the target in specific dwell time. The number of atoms evaporated per single pulse can be expressed as follows:

$$N_p = R_{evp} A_{foc} [atoms] \quad (4.7)$$

Then the number of atoms evaporated from the same spot after successive pulses at the laser beam dwell time of D_t reads:

$$N_{MP} = N_p R_{rep} D_t = R_{evp} A_{foc} R_{rep} D_t \text{ [atoms]} \quad (4.8)$$

By substituting Eq. 4.7 into Eq. 4.8, the number of evaporated atoms by successive pulses based on laser parameters and target material properties can be estimated as following:

$$N_{MP} \approx n_{air} \left(\frac{k_B a A t_{eq}^{3/2}}{M_a k_h \pi^{3/2}} \right)^{1/2} (P_{avg} R_{rep} A_{foc})^{1/2} D_t \text{ [atoms]} \quad (4.9)$$

One should note from Eq. 4.9 that the number of evaporated particles is a function of laser processing parameters, material properties, and ambient gas vapor density. The main factor is laser beam dwell time which linearly affects the evaporated atoms. The laser repetition rate influences the number of evaporated atoms by a square root.

As the laser beam dwell time is usually higher than the time between the two successive laser pulses in MHz-repletion regimes, multiple pulses arrive at the same spot. Consequently, the atomic flow into the plume would remain at levels required to generate nanostructures.

4.1.3 Nanostructure growth in ambient air

The expanding plume of ablated material cools down adiabatically either owing to diffusion in the ambient air or by expansion in vacuum. Vapour condensation starts with nucleation, proceeds with growth of a supercritical nucleus and comes to a halt due to quenching. The density and temperature of evaporated atoms in the adiabatically expanding plume are the main factors for formation of nanostructures. The diffusion and

collision of evaporated atoms/ions with ambient gas atoms/ions at the high temperature early in the cooling process result in coalescence [61]. As the plume cools down, coalescence terminates and colliding particles are likely to form aggregates. The formation of nanostructures will go on through an aggregate-aggregate and atom-aggregate attachment over the period of time after the end of the laser pulse. The longer the plume with high density and temperature lasts the more consecutive inelastic collisions occur, and as a result, the larger nanostructures would form. The time plume lasts until diffuse to the background air depends on the combination of laser, material parameters, and ambient condition. However, it's been reported that the diffusion time of the ablated material through the gas plays a major role in determining the cluster formation time and, thus, the nanostructure size [118]. Depending on the density of the evaporated atoms, different type of nanostructures from individual particles to 3-D nanofibrous structures can be formed and deposited on the substrate. Therefore, in order to synthesize 3-D nanofibrous structures, the continuous arrival of the laser pulses are required to keep the plume density at the critical point for 3-D nanostructure formation. Previous studies have confirmed that only MHz laser pulse repetition rates lead to formation of 3-D nanostructures [35], [114].

The simplified kinetic model of nanocluster formation may be applied to estimate the number of atoms in a nanostructure as a function of average plume parameters, based on the conservation of energy, momentum, and number of atoms in the generated plume after the end of the pulse. Accordingly, it could predict the nanostructure size and radius of a nanofiber [118]. This model assumes that a nanocluster is formed through the neutral-neutral monomer inelastic sticky collisions and ignores the ion-ion, ion-neutral, and the

other complex dusty-plasma collision effects. The first important step toward synthesis of a large nanostructure is the formation of dimers.

The use of an ambient air with atmospheric pressure has the advantages of the plume confinement which increases the density of the component atoms in formation region leading to higher probability of sticky attachment. It's been reported that the diffusion plays the major role when the pressure of background gas approaches 10% of atmosphere pressure. Therefore, one can assume that in ambient air only diffusion-dominated expansion of the plume exists.

Diffusion of single titanium atoms in air of density n_{air} proceeds with diffusion velocity, $D_{dv} = lv_{Ti}/3 \approx v_{Ti}/(3n_{air}\sigma_{Ti-air})$ where σ_{Ti-air} is the cross section for titanium-air elastic collision. Note that $Ti - air$ collision cross section is almost 10 times larger than that for $Ti - Ti$ collisions. The diffusion coefficient in the mixture of two gases depends on the total cross section σ_{total} which expresses as the following:

$$\sigma_{total} = \frac{\pi(d_1^2 + d_2^2)}{4} \quad (4.10)$$

where d_1 and d_2 are diameters of particles in the mixture. In case of $Ti - Ti$ collision, the total cross section $\sigma_{Ti-Ti} = 0.31 \times 10^{-15} \text{ cm}^2$ (the atomic radius 140 pm; $d_{Ti} = 280 \text{ pm}$). The cross section of titanium atoms and air (Considering oxygen atom radius, $d_{air} = 308 \text{ pm}$) is on $\sigma_{Ti-air} = 1.36 \times 10^{-15} \text{ cm}^2$. Thus the formation of nanostructures mostly depends on the diffusion of Ti atoms in ambient air.

Following the model presented in [118], one can assume that the time for a formation nanofiber composed of N atoms equals to diffusion time, then the radius of a synthesized nanofiber reads:

$$r_{nanofiber} \approx B n_{Ti}^{-2/15} l_{abl}^{1/6} n_{air}^{3/10} (\sigma_{Ti-Ti} \sigma_{Ti-air})^{1/4} \left(\frac{T_{min}}{T_0} \right)^{1/20} \quad (4.11)$$

Here, $l_{abl} \equiv N_p / n_{Ti} A_{foc}$ is the ablation depth, B is a dimensionless numerical coefficient that should be estimated from the experiments, T_{min} is the minimum temperature for the nanostructure formation which is equal to the temperature in the mixture of Ti-air atoms after equilibrium, and $T_0 = T_{max}$ is the initial plume temperature. Therefore, the nanofiber radius depends on the air density, the cross section of target and ambient gas atoms, and the number of ablated atom estimated from Eq. 4.9, in the diffusion dominated conditions as follows:

$$r_{nanofiber} \approx B n_{Ti}^{-9/30} n_{air}^{3/10} (\sigma_{Ti-Ti} \sigma_{Ti-air})^{1/4} \left(\frac{N_p}{A_{foc}} \right)^{1/6} \left(\frac{T_{min}}{T_0} \right)^{1/20} \quad (4.12)$$

As one can see from Eq. 4.12, the main factor playing role in nanofiber size is the density of the ambient air, which affects the size approximately as a cubic root of the gas pressure.

4.1.4 Experimental Results and discussion

4.1.4.1 Morphology of nanostructures

As indicated before, the structure of the nanofibrous architecture is influenced by various laser parameters, such as laser fluence, laser pulse repetition, and laser pulse dwell time. This study investigated the influence of laser pulse repetition rate on porosity, density, and size of the generated nanofibers. The ablation of Ti target was performed at different repetition rates from 2MHz to 26 MHz at laser pulse dwell time of 1ms. Figure 4.1 SEM images of titania nanofibrous structures generated on a Ti substrate at laser repetition of a) 4 MHz and b) 12 MHz. shows SEM micrographs of the nanofibrous structure generated on the Ti surface at pulse repetition rates of 4 and 12 MHz. A close-up view of the structure shows that it consisted of self-assembled closed rings and bridges in which nanoparticles are aggregated together. The pores are interconnected.

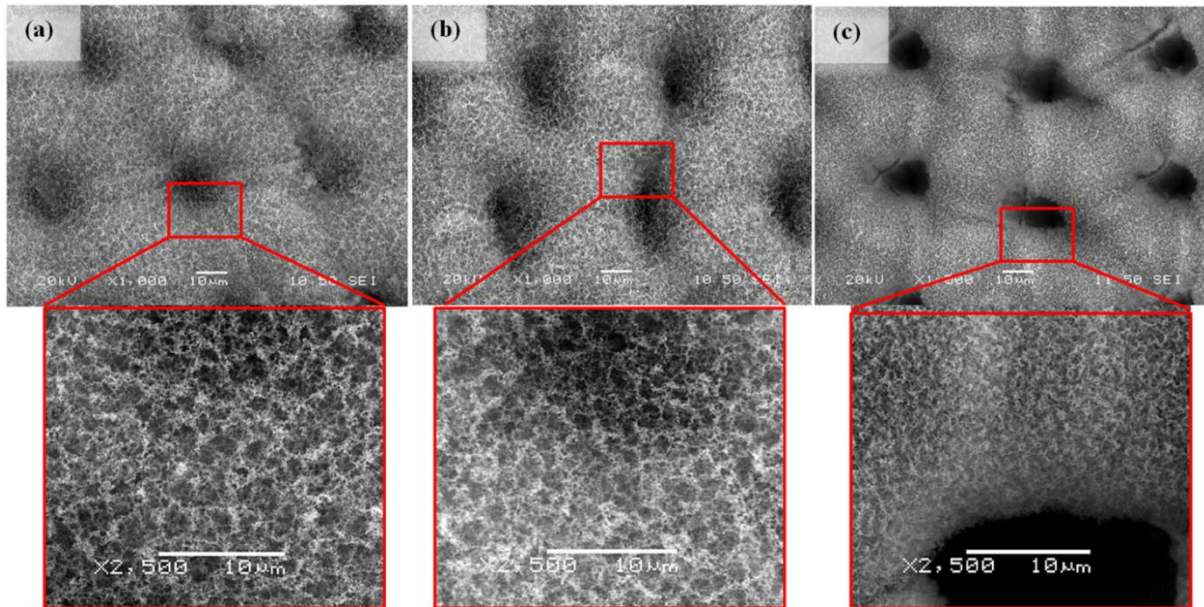


Figure 4.1 SEM images of titania nanofibrous structures generated on a Ti substrate at laser repetition of a) 4 MHz and b) 12 MHz.

It was observed from the experiments that by increasing the laser pulse repetition rates from 2MHz up to 8MHz, the density of generated nanostructures increases. However, increasing the repetition rate beyond 8MHz leads to a decline to the abundance of generated nanostructures. Figure 4.2 presents the number of evaporated atoms predicted by Eq. 4.9, by increasing the laser pulse repetition rate the number of pulses arrive at the same spot for the particular laser pulse dwell time increase which leads to higher amount of ablated atoms. However, as the curve for absorbed laser fluence in Figure 4.2 suggests, the increase of laser repetition rates results in a reduction in laser pulse energy and consequently on the laser ablation fluence to the point that it drops below the target ablation threshold. In case of titanium target, the ablation threshold was measured to be $0.48 J/cm^2$. Taking into the account our system average laser power $P_{avg} = 10 W$, $A_{foc} = 84.62 \times 10^{-8} cm^2$, and titanium laser absorption coefficient for titanium $A = 0.42$, one can see that at the repetition rates more than 8MHz the laser fluence drops below the required fluence for ablation of titanium target which in accordance with our experimental results.

From Eq. 4.6 one can predict the thermal evaporation rates in ambient air for different laser fluences. Different laser fluences were achieved by varying the laser repetition rates (see Figure 4.3). Using Eq. 4.6 for the laser fluence of $1.2 J/cm^2$ will result in the evaporation rate of $1.85 \times 10^{16} cm^{-2}$ for Ti target. This value is in good agreement with the thermal evaporation of Fe target in air ($1.67 \times 10^{15} cm^{-2}$) close to our experiment parameters reported elsewhere [94]. The higher evaporation rate for Ti may be attributed to the greater Ti absorption coefficient ($A_{Ti} = 0.42$ and $A_{Fe} = 0.36$) and its lower thermal

losses ($a_{Ti} = 0.714 \times 10^{-1} \text{ cm}^2/\text{s}$, and $a_{Fe} = 2.26 \times 10^{-1} \text{ cm}^2/\text{s}$) in compare to ones for Fe which lead to higher fluence absorption and lower heat transfer to the lattice.

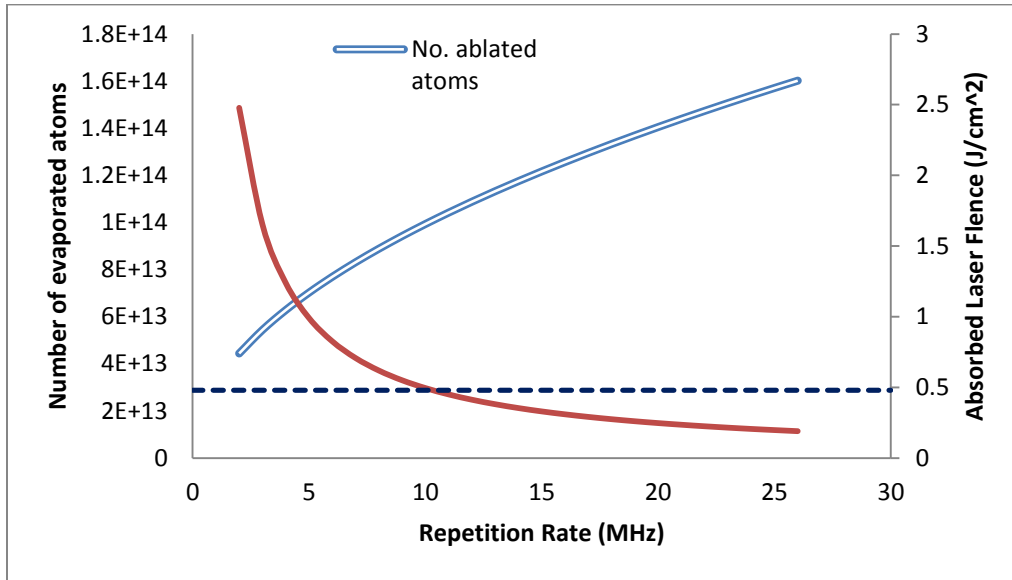


Figure 4.2 The number of ablated atoms from the Ti target at different laser pulse repetition rates at laser pulse dwell time of 1ms based on Eq. 4.9 depicted by the blue hollow line. The red solid line represents the absorbed laser fluence by the Ti target. The dashed line determines the laser ablation threshold of 0.42 J/cm^2 for Ti.

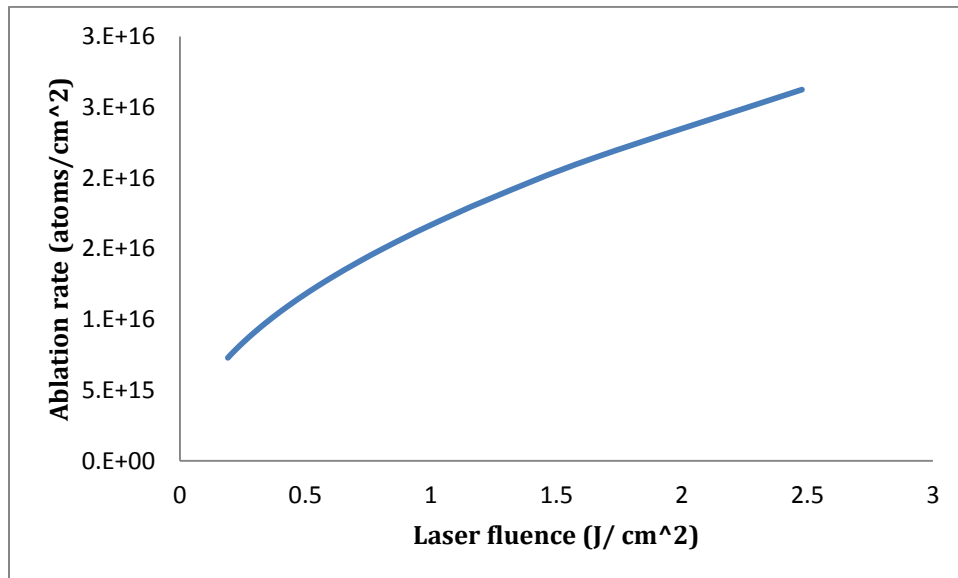


Figure 4.3 The average evaporation rate for a single pulse at different laser fluences predicted by Eq. 4.6.

To study the effect of laser repetition on nanofiber size, the generated nanofibers detached from the substrate and characterized by TEM. In TEM micrographs of a single nanofiber one can observe a high degree of nanoparticle aggregation (Figure 4.4). The average diameter of the nanofibers generated at different repetition rates is depicted in Figure 4.5. The average nanofiber diameter is approximately 16–20 nm for structure generated at pulse repetition of 12 MHz and increases as the repetition rate is reduced to 2 MHz.

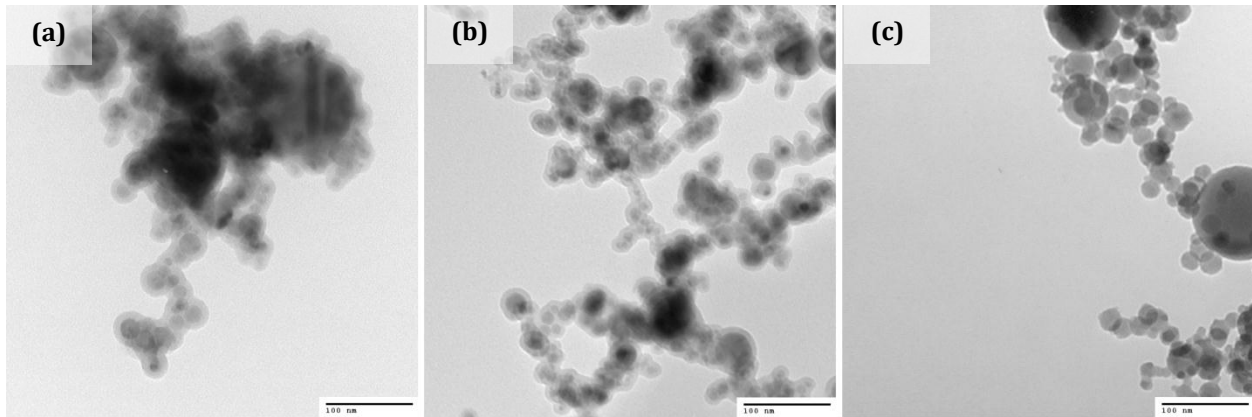


Figure 4.4 TEM images of Ti nanofibers synthesized at repetition (a) 4 MHz, (b) 8 MHz, and (c) 12MHz (the scale bar : 100nm).

As mentioned before, laser fluence at repetition higher than 12 MHz falls below the ablation threshold for Ti, hence, at repetition of 26 MHz barely nanofibrous structures can be seen instead nanostructures in form of nanoparticles are generated. These results indicate that a reduction in laser pulse repetition rate leads to an increase in the density of the nanofibrous structures as well as in the size of nanoparticles. This is due to the fact that at laser repetitions above the target ablation threshold, the increase in laser repetition rates will result in higher evaporation rates. The volumetric concentration of evaporated atoms in the plume strongly influences the number of primary nucleation sites [61].

Increasing the number of primary nucleation sites causes a reduction in nanofiber size. Moreover, an increase in the laser fluence results in increase of plume temperature and consequently the time required for nanoparticle sticky attachment. This results in forming larger nanofibers. As a results of finer and abundance nanofibers, the pore size of the nanostructures become smaller, as illustrated in Figure 4.6.

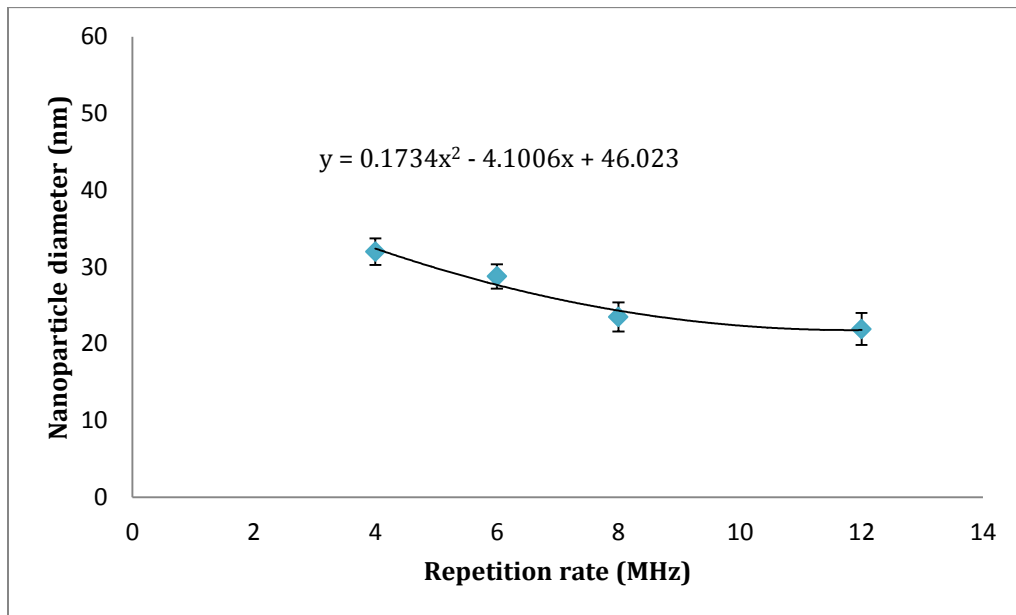


Figure 4.5 Measured average nanofiber diameter at different laser pulse repetition rates.

The experiments have shown that at laser fluences above the ablation threshold fluence of titanium, the increase in laser pulse dwell time influences the number of laser pulses hit the same spot on the target. Subsequently, it leads to a rise of ablation rate. The deposition rate of nanostructures is analogous to the ablation. The results from the experiments indicate that the density of synthesized nanostructures intensify by increasing of laser pulse dwell time.

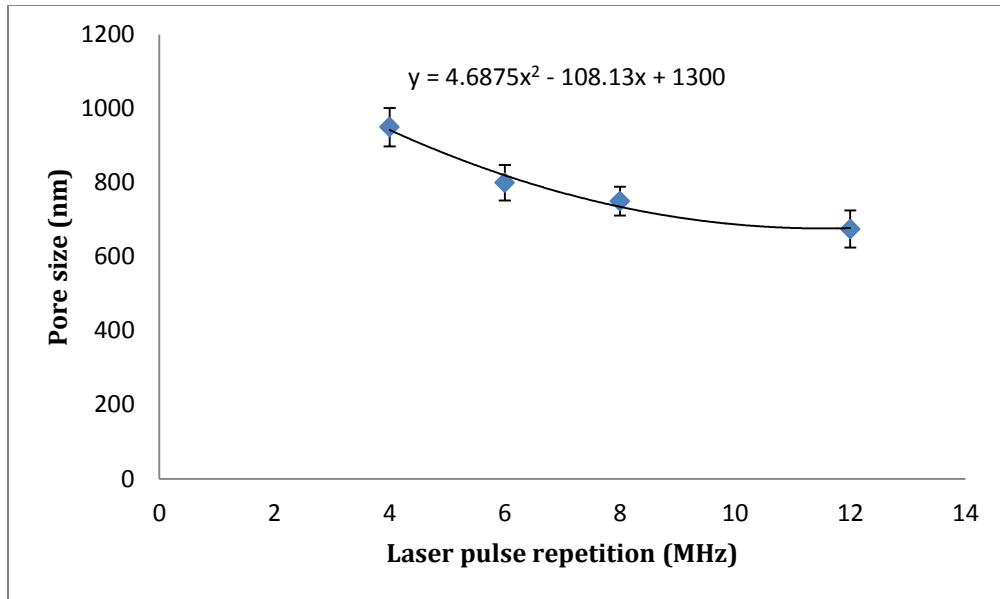


Figure 4.6 Measured average pore sizes of generated structures at different laser pulse repetition rates.

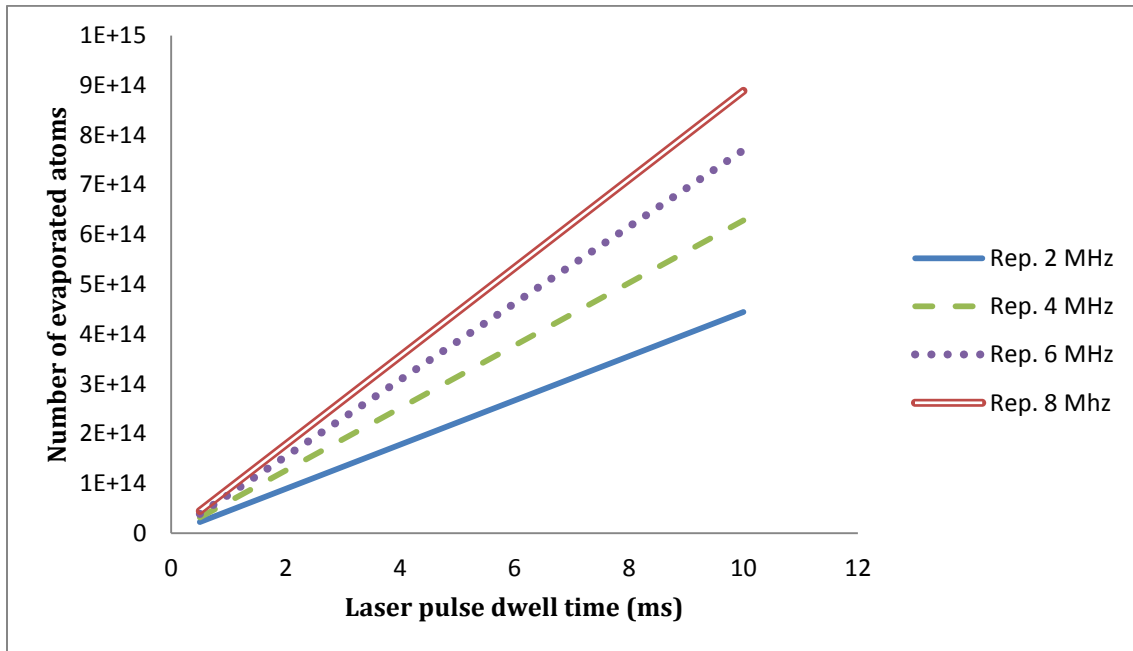


Figure 4.7 The number of ablated atoms from the Ti target at different laser dwell time and laser pulse repetition rate predicted by Eq. 2.17.

Figure 4.7 shows the predicted evaporation rates for target ablation at different laser pulse dwell times and laser repetitions. Laser processing of a target at laser dwell time of 1ms and laser repetitions of 12 MHz means that 12K pulses would arrive at the same spot on the target surface. The time interval between the pulses is 83 ns. Previous studies on the ablation of Ti in ambient air by laser intensities close to our experiment parameters suggested that plume expansion time lasts for more than 300nm [98], [119]. Therefore, one can expect the accumulation effect when laser ablating by repetition rates higher than 2MHz. It's in agreement with previous study which reported that the threshold pulse repetition frequency for 3-D nanofibrous structure formation is around 2 MHz [114].

4.1.4.2 *Phase analysis of nanostructures*

XRD analysis was performed in order to evaluate the crystal structure of nanofibrous layer. Figure 4.8 shows the XRD patterns of the nanofibrous layer generated on the Ti substrate. The unprocessed Ti sample was entirely composed of alpha-phase titanium (α -Ti), while the pattern of nanofibrous structure indicate that it consists of tetragonal TiO_2 (rutile and anatase) and cubic TiO (hongquite). The sharp peaks in the patterns can be associated with the high crystallinity of the oxide phases. Titania exists in two main crystallographic forms, anatase (A) and rutile (R) [120]. The XRD peaks at 2θ : 25.28° (A101) and 2θ : 27.4° (R110) are often interpreted as the characteristic peaks of anatase and rutile crystal phases, respectively [120], [121]. The peaks at 2θ : 43.37° may be attributed to TiO . The mixture of anatase and rutile crystalline phases in the synthesized titania nanostructures can be connected to the oxygen concentration change during the ablation process. Previous studies have suggested that there might be a definite linking

between the available oxygen during the synthesis procedure and the growth of crystalline phases [122].

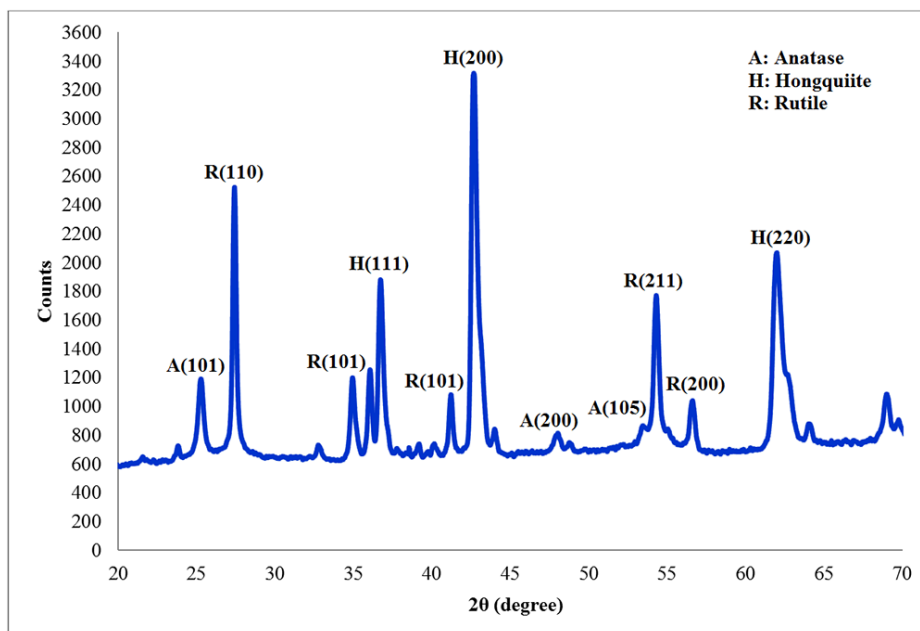


Figure 4.8 X-ray Diffraction patterns of generated titania nanofibrous layer Ti sample after laser irradiation.

Figure 4.9 depicts the schematic illustration of titania nanofibrous structure using femtosecond laser ablation of Ti target. The high temperature plume generated by laser ablation is very reactive. Thus, the presence of trace amounts of reactive gases, like oxygen in case of ambient air, can lead to chemical reactions. The evaporated atoms, in our case *Ti*, reacts with the surrounding oxygen in the front boundary of the expanding plume, and consequently, *Ti-O* molecular monomers are formed. As the oxidation of *Ti* to generate *TiO₂* is highly exothermic with the enthalpy of formation of -944.74 kJ/mol , *TiO₂* molecular would be formed preferably. The generated molecules, later, collide as a result of thermal motion. The generated *TiO₂* vapor flows to the outer wall of the plume where temperature is lower, allowing the *TiO₂* supersaturation which results in the nucleation. Once the

temperature falls to the range below the boiling or sublimation point, nanostructures start to form.

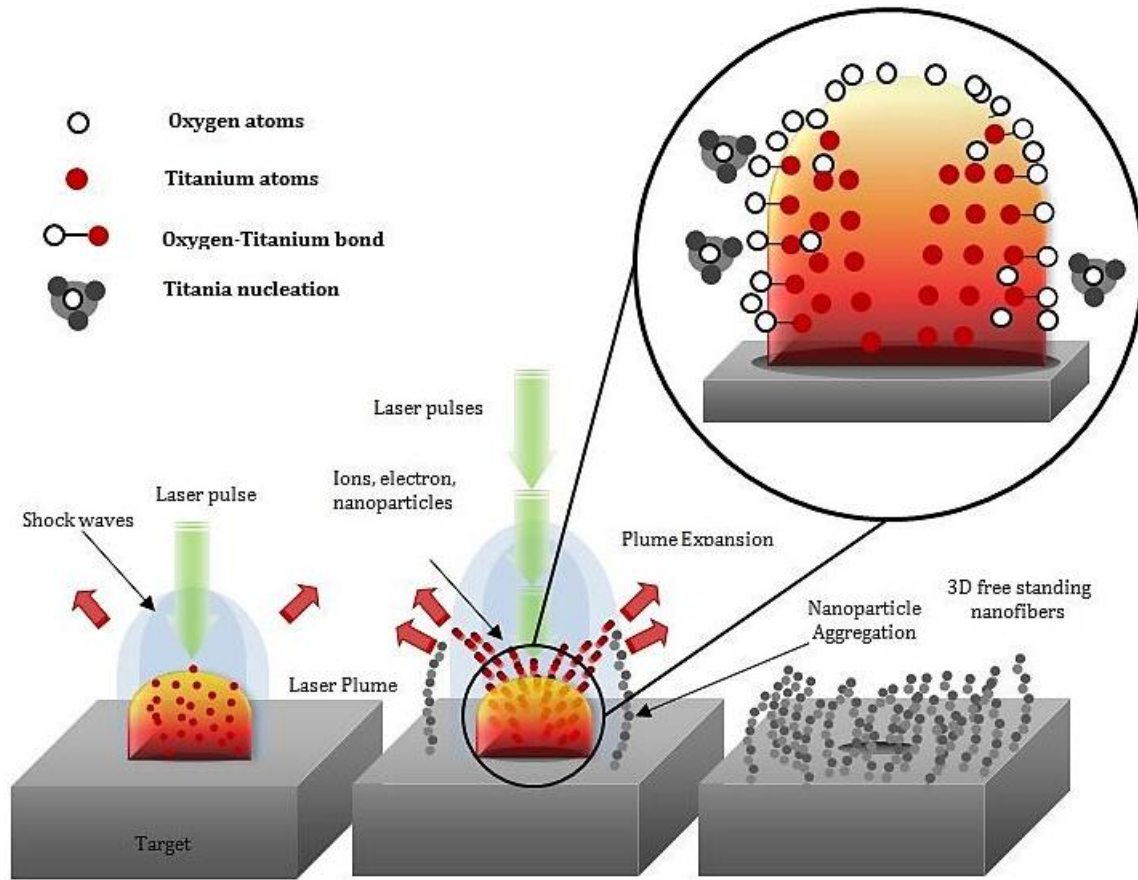


Figure 4.9 Schematic illustration of titania nanofibrous structure using femtosecond laser ablation of Titanium target.

4.2 Laser Processing of Natural Biomaterial: Synthesis of 3-D calcium carbonate nanofibrous structure from eggshell¹

Natural biomaterials from bone-like minerals derived from avian eggshells have been considered as promising bone substitutes owing to their biodegradability, abundance, and lower price in comparison with synthetic biomaterials. However, cell adhesion to bulk biomaterials is poor and surface modifications are required to improve biomaterial-cell interaction. 3-D freestanding nanostructures are preferred to act as growth support platforms for bone and stem cells. Although there have been several studies on generating nanoparticles from eggshells, no research has been reported on synthesizing 3D nanofibrous structures. This study proposes a novel technique to synthesize 3-D calcium carbonate interwoven nanofibrous platforms from eggshells using high repetition femtosecond laser irradiation. The eggshell waste is value-engineered to calcium carbonate nanofibrous layer in a single step under ambient conditions. Our striking results demonstrate that by controlling the laser pulse repetition, nanostructures with different nanofiber density can be achieved. This approach presents an important step towards synthesizing 3-D interwoven nanofibrous platforms from natural biomaterials. The synthesized structures can promote biomaterial interfacial properties to improve cell-platform surface interaction and develop new functional biomaterials for a variety of biomedical applications.

¹ Reprinted from Journal of Nanobiotechnology, 9, A. Tavangar, B. Tan, and K. Venkatakrishnan, Synthesis of three-dimensional calcium carbonate nanofibrous structure from eggshell using femtosecond laser ablation, Copyright (2011), with permission from BioMed Central. The dissertation author was the primary investigator and author of this article.

4.2.1 Materials and experimental details

The avian eggshell representing 11% of the total weight of the egg consists mainly of calcium carbonate (94%), calcium phosphate (1%), organic matter (4%) and magnesium carbonate (1%) [74]. Hen's eggs were purchased, emptied and washed thoroughly with distilled water to get rid of dirt and organic layer. Experiments were carried out with a 1040 nm wavelength direct-diode-pumped Yb-doped fiber amplified ultrafast laser system. To investigate the effects of pulse repetition rate on morphology of generated nanofibrous structures, experiment were performed at laser repetition of 4, 8 and 13 MHz. The nanofibrous structure morphology was then characterized using SEM, EDS, and TEM analyses. Phase analysis of the synthesized structures was performed using XRD.

4.2.2 Results and discussion

The morphology of the nanofibrous structures are influenced by various laser parameters such as, laser fluence, laser repetition, and laser dwell time. Figure 4.10 depicts the nanofibrous structure generated at repetition of 4 MHz. A close-up view of the structures shows that they consists of self-assembled closed-rings and bridges in which particles are fused together, as shown in Figure 4.10. TEM image of a single nanofiber demonstrates a high degree of nanoparticle aggregation with average size of 50 ± 20 nm (Figure 4.11). Therefore, the bond between the particles themselves and with the eggshell substrate is assumed to be strong.

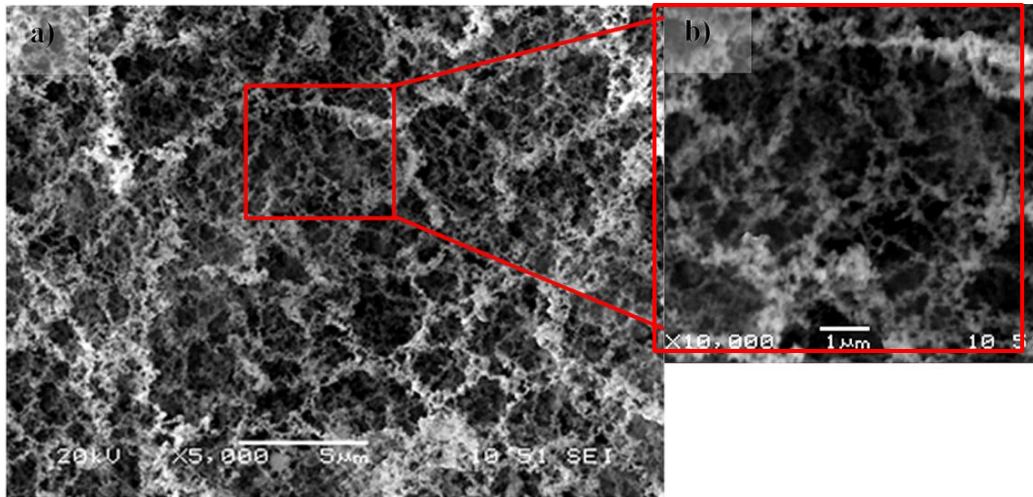


Figure 4.10 SEM images of calcium carbonate nanofibrous structure synthesized on an eggshell at laser repetition rate of 4 MHz.

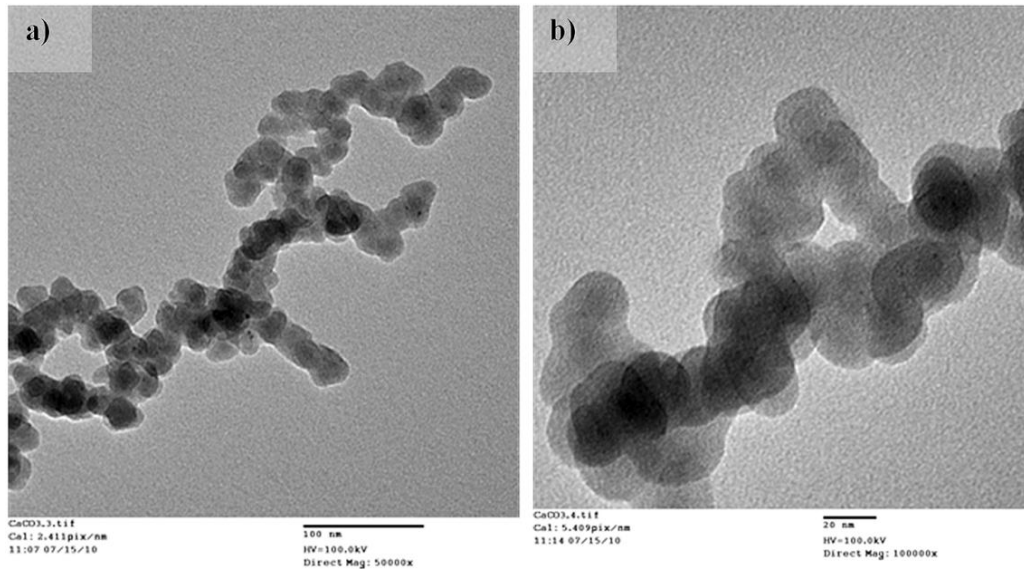


Figure 4.11 TEM images of calcium carbonate nanofibers synthesized at repetition rate of 4 MHz at magnification of a) X50000 and b) X100000

Further experiments were performed with different laser repetition rates at 8 and 12 MHz (see Figure 4.12). It can be observed that the structure pore size has been decreased by increasing the repetition rate. This is due to the increase in density of synthesized nanofibers.

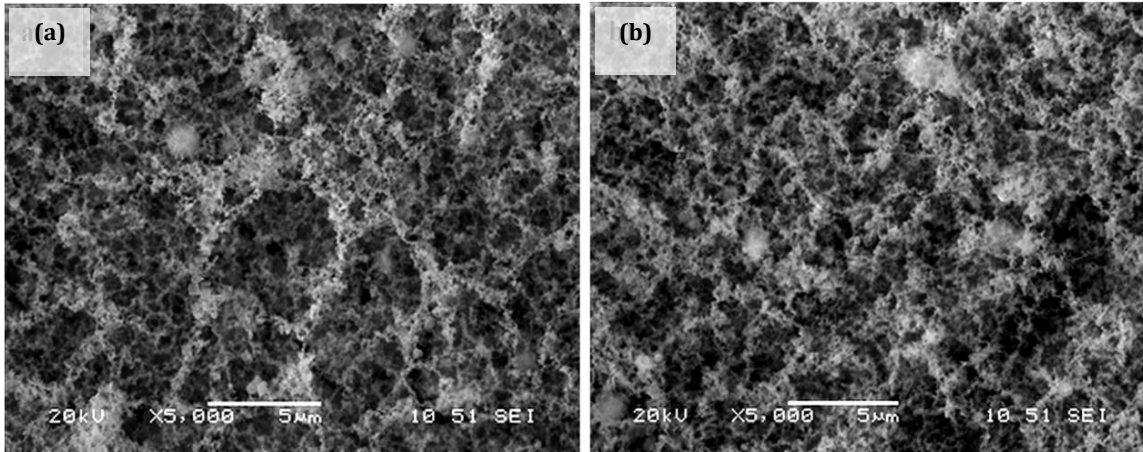


Figure 4.12 SEM images of calcium carbonate nanofibrous structure synthesized on an eggshell at laser repetition rates of (a) 8 MHz, and (b) 13 MHz.

The EDS analysis was conducted in order to evaluate the composition of nanofibrous structure. Figure 4.13 depicts the EDS analyses which compare the elemental composition of nanofibrous structures with an unprocessed eggshell. Although all the elements presented on the unprocessed eggshell, i.e., Ca, P, Mg, C, and O, can be recognized on the synthesized nanofibrous structure, the percentage of oxygen and carbon has been decreased significantly in the nanofibers which implies the decomposition of the organic part due to laser irradiation.

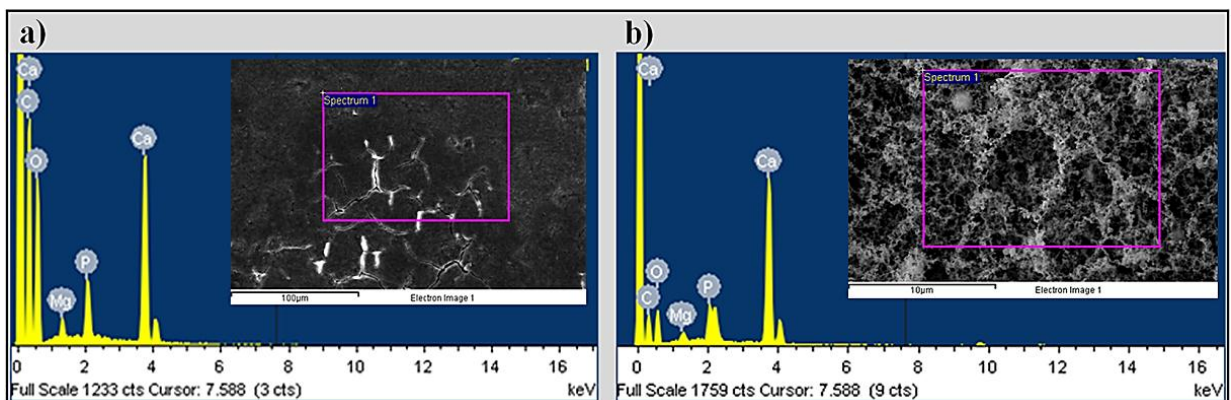


Figure 4.13 EDS analyses of (a) unprocessed eggshell, and (b) synthesized calcium carbonate nanofibrous structure.

In order to observe the possible phase changes of nanofibrous structures as a result of laser irradiation, the XRD pattern of unprocessed eggshell and the nanofibrous structures can be compared. From Figure 4.14 one can notice that the XRD patterns for both samples show a significant peak around 30° (2θ). This is the characteristic of crystalline calcite which indicates the hkl (104) [74], [123]. However, there are three peaks marked with asterisks (*) which are associated with calcium hydroxide [124]. Laser irradiation might result in calcium carbonate decomposition to calcium oxide. This calcium oxide later would convert to calcium hydroxide due to atmosphere exposure [74], [124]. Comparing Figure 4.14a and Figure 4.14b, it can be observed that the intensity of the XRD peaks has been decreased for nanofibrous structures due to the reduction of the calcite crystal sizes.

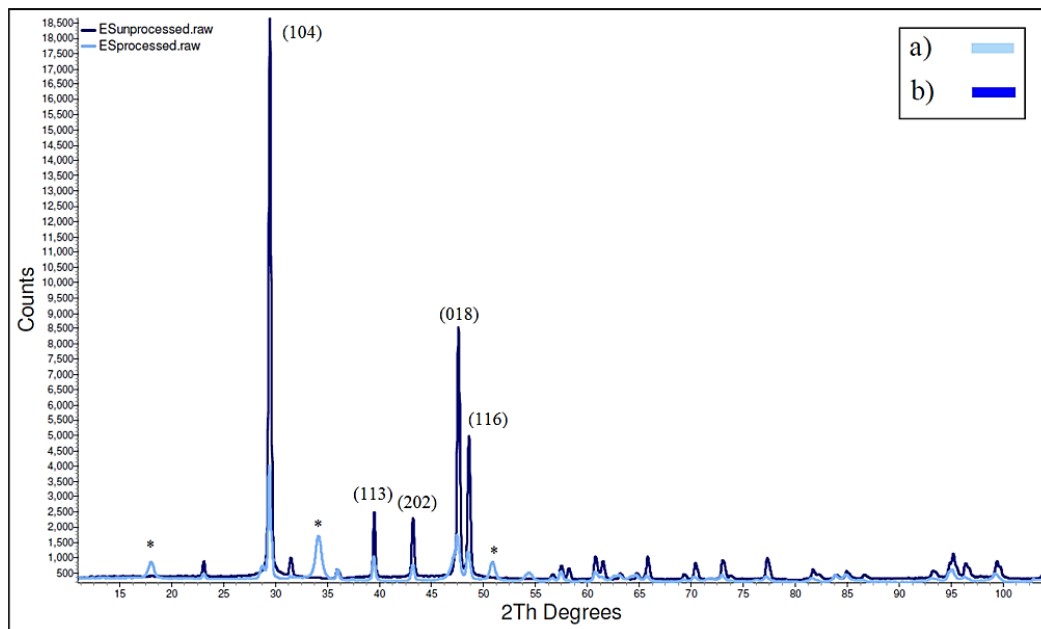


Figure 4.14 X-ray Diffraction patterns of (a) unprocessed eggshell (b) nanofibrous structure generated on the eggshell substrate. The peaks marked with asterisk (*) correspond to calcium hydroxide.

Previous *in vitro* and *in vivo* studies have pointed out that the microporosity of the bone substitute surface structure as well as its biodegradability play an important role in bone healing. Thus, the generated nanofibrous structure with different porosity shows a different degree of biodegradability when implanted in the biological environment. Microporosity influences the bone substitute dissolution rate in biological fluids; hence a surface with higher porosity shows better degradability. Biodegradation of bone substitutes is vital to initiate the bone deposition process [125], [126]. Porous structures increase adsorption of proteins such as bone morphogenetic proteins and other necessary ones required for bone formation which consequently influences cell adhesion and the subsequent cell proliferation and differentiation of osteoblasts [72], [125], [126]. On the other hand, cell attachment and proliferation are improved for nanostructures in comparison with micron-structures owing to higher effective surface area of the nanofibers [84]. As a result, it is predicted that the calcite nanofibrous structure generated on the eggshell substrate could enhance the biodegradability as well as the osteoconductivity of the surface in comparison with nanoparticles or micron-structure.

4.3 Laser Processing of Natural Material: Synthesis of 3-D

Micro/Nanostructures on Rice Husk and Wheat Straw

Amorphous silica has been proven to be biocompatible and biodegradable in living tissue. However, cell adhesion to bulk biomaterials is poor and surface modifications are required to improve biomaterial-cell interaction. In this study, high repetition femtosecond laser irradiation is utilized to synthesize interwoven micro/nanostructures from rice husk and wheat straw. The rice husk and wheat straw bio-waste is value engineered to silica 3-D fibrous structure in a single step under ambient conditions. The striking results from this study demonstrate that by controlling the laser fluence, nanostructures with different nano-features can be achieved.

4.3.1 Results and Discussions

The structure of the nanofibrous layer is affected by various laser parameters such as laser fluence, laser pulse repetition and laser pulse dwell time. First, the influence of laser power on porosity and size of the synthesized nanofibers was studied.

Figure 4.15 shows SEM images of the nanofibrous layer generated at pulse repetition of 26 MHz and beam power of 15W. A close up view of the layer shows that it consisted of self-assembled closed rings and bridges in which nanoparticles are fused together rather than loosely bonded. Figure 4.16 and Figure 4.17 depict the structures synthesized at 26 MHz laser repetition but at different power.

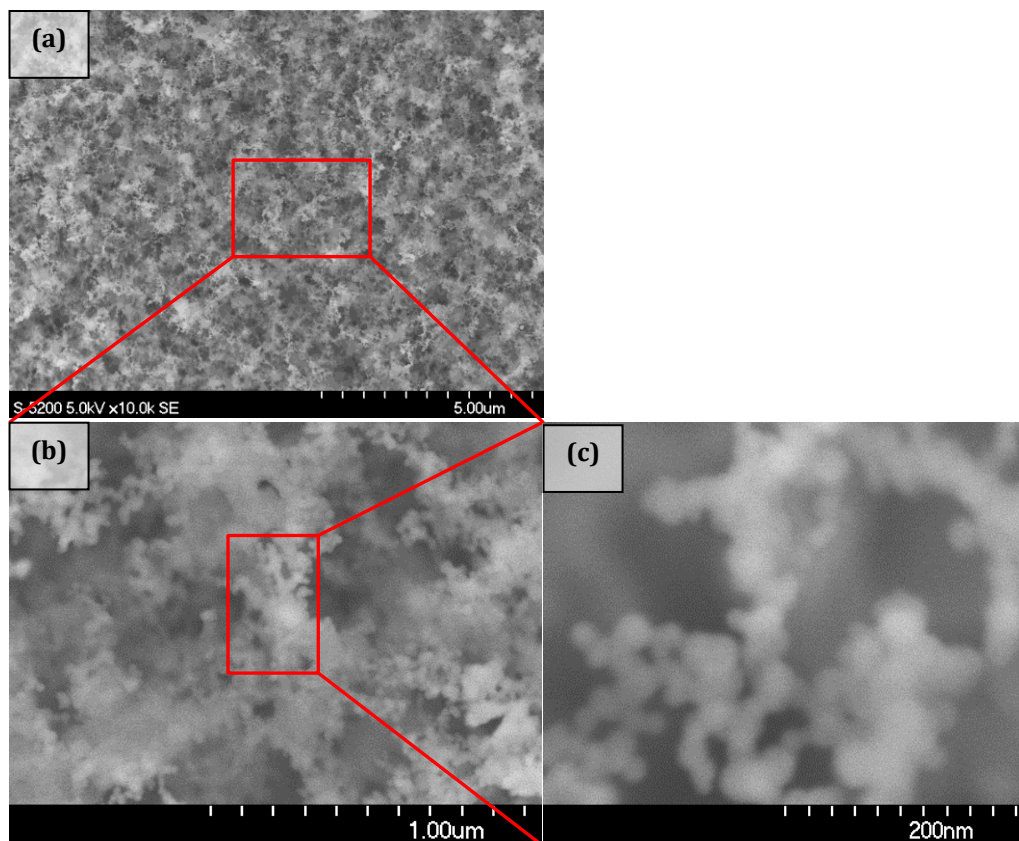


Figure 4.15 SEM micrograph of structure generated on rice husk at laser rep of 26 MHz, and dwell time of 0.1 ms beam power of 15W at magnification of a) X10K, b) X50K, and c) X200K.

Keeping the repetition rate constant, by decreasing the laser power the pulse energy and consequently laser fluence reduces. Nanofibrous structures are results of the nanoparticle aggregation. Nanoparticle aggregation takes place as part of vapor condensation by the collision of nucleus. To generate nanofibrous structures, an immense amount of nanoparticle aggregation is required. Therefore, continuous arrival of the plume is needed in order to maintain the nucleus density at a certain level. Therefore, critical amount of pulse energy should transfer to the substrate in order to initiate the plume and keeps it at certain level. Hence, the formation of nanofibrous structure is not possible in lower laser power instead microstructure will be synthesized.

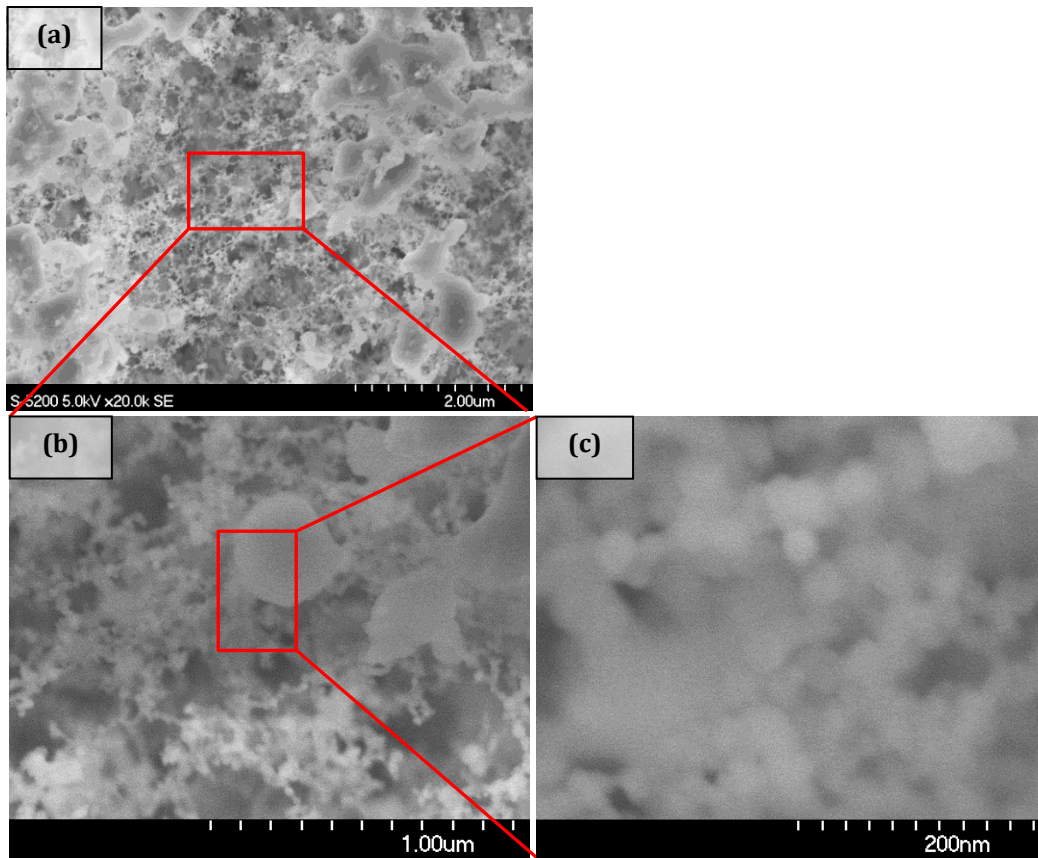


Figure 4.16 SEM micrograph of structure generated on rice husk at laser rep of 26 MHz, dwell time of 0.1 ms and beam power of 10W at magnification of a) X20K, b) X50K, and c) X200K.

Figure 4.18 compares the changes on composition of nanofibrous structures by altering the laser power using EDS analysis. Since experiments have been carried out at an ambient condition, the presence of oxygen is noticeable. For the unprocessed rice husk and synthesized structures at lower power, silicon and other inorganic elements are not detectable or barely detectable due to high amount of organic on the substrate. At higher laser power, the organic part is burnt away and the other inorganic element could be distinguished. Comparing unprocessed and processed structures, it's interesting that elements such as chlorine which are not in favor has been removed after laser ablation.

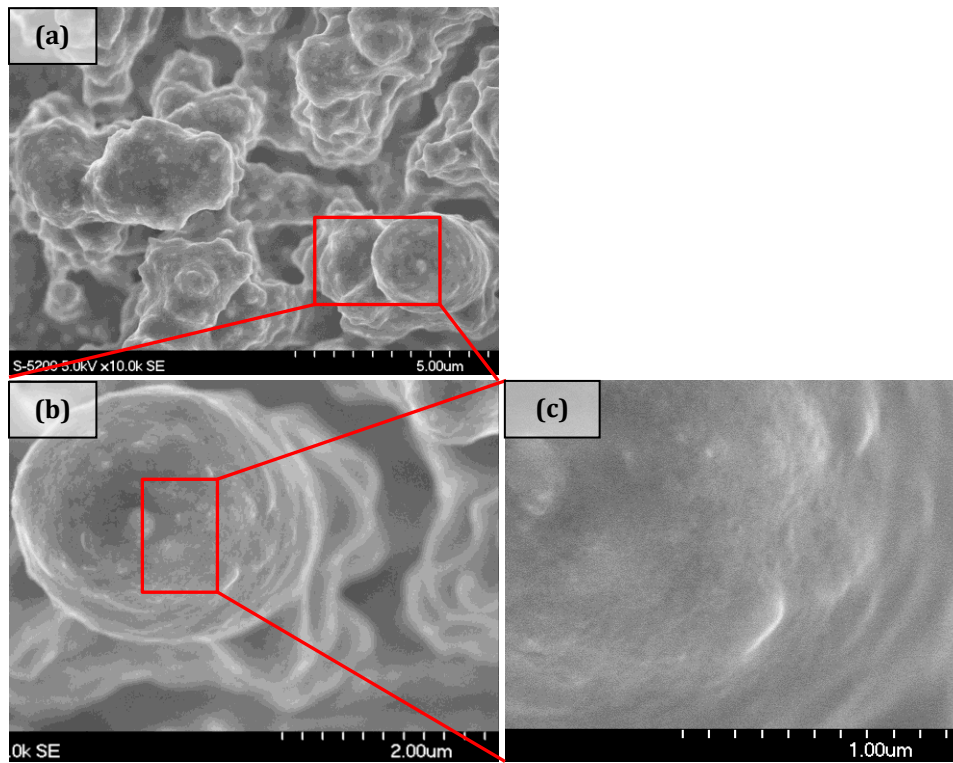


Figure 4.17 SEM micrograph of structure generated on rice husk at laser rep of 26 MHz, and dwell time of 0.1 ms beam power of 5W at magnification of a) X10K, b) X20K, and c) X50K.

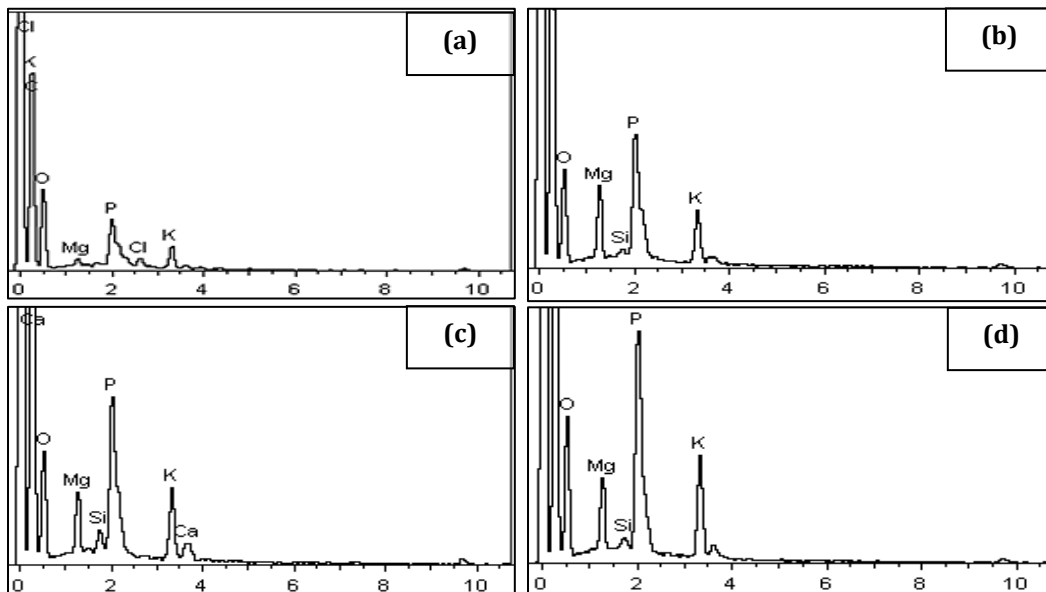


Figure 4.18 EDXs analyses of a) unprocessed rice husk and b) structures generated on rice husk at laser rep of 26 MHz and power 5W, c) structures generated on rice husk at laser rep of 26 MHz and power 10W, and d) structures generated on rice husk at laser rep of 26 MHz and power 15W.

The experiments were carried on at different laser repetition and dwell time. Figure 4.19 through Figure 4.22 illustrate the structures synthesized at different laser dwell time and power. Decreasing the dwell time leads to reducing laser fluence transfer to the substrates. This will result in a decrease in plume volume and nucleus density inside it which leads to generation of microstructures instead of nanofibrous structures.

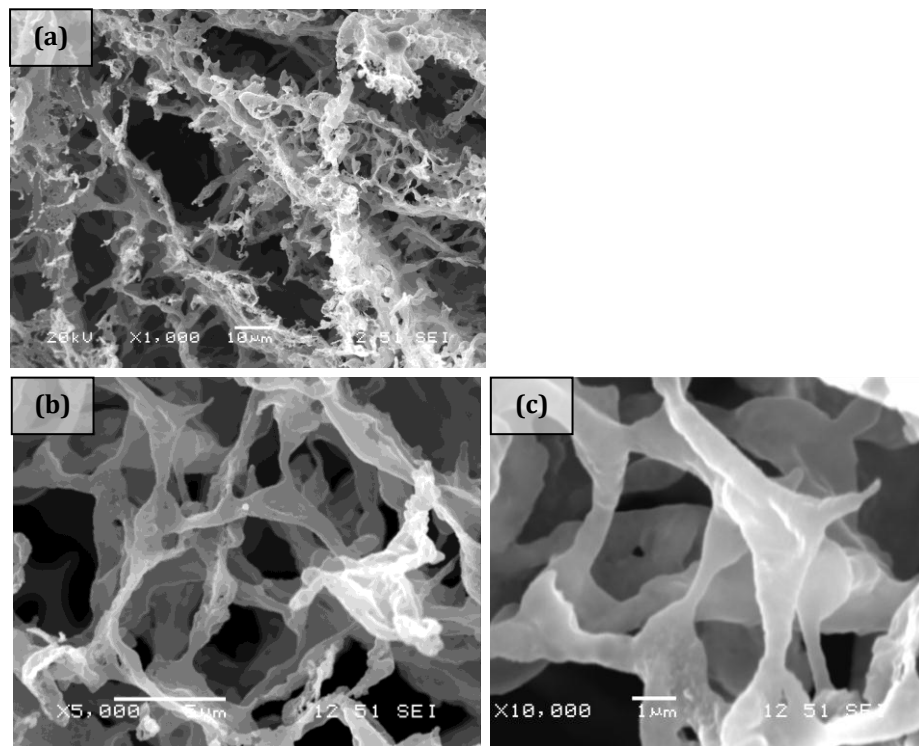


Figure 4.19 SEM micrographs of structure generated on Rice husk at laser rep. of 26 MHz, dwell time of 0.05 ms, and power of 5W at magnification of a) X1K, b) X5K, and c) X10K.

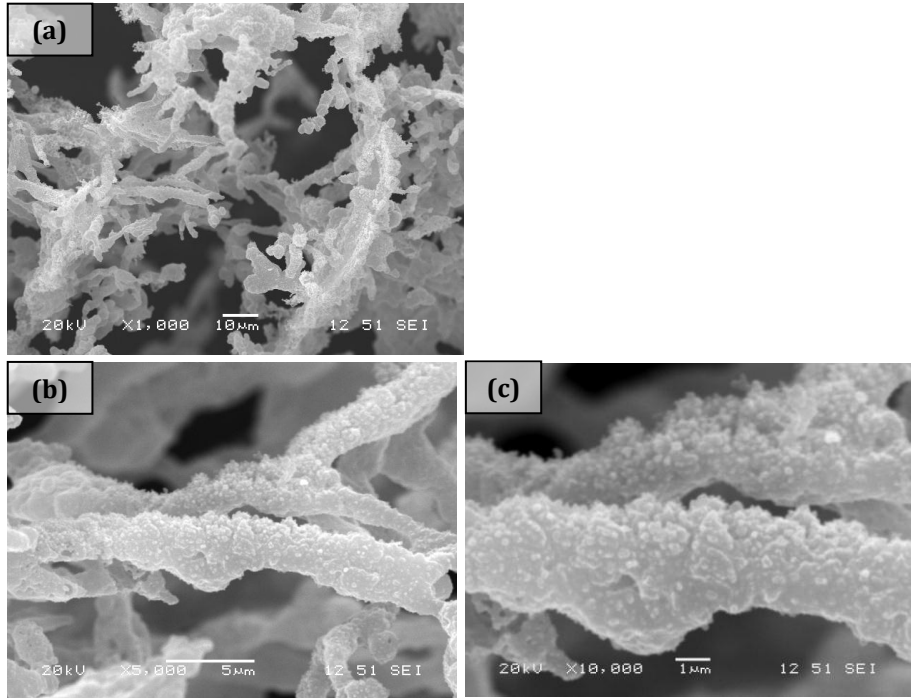


Figure 4.20 SEM micrographs of structure generated on wheat straws at laser rep of 26 MHz, dwell time of 0.05 ms, and power of 5W at magnification of a) X1K, b) X5K, and c) X10K (Same parameters as Figure 4.19 but at different location).

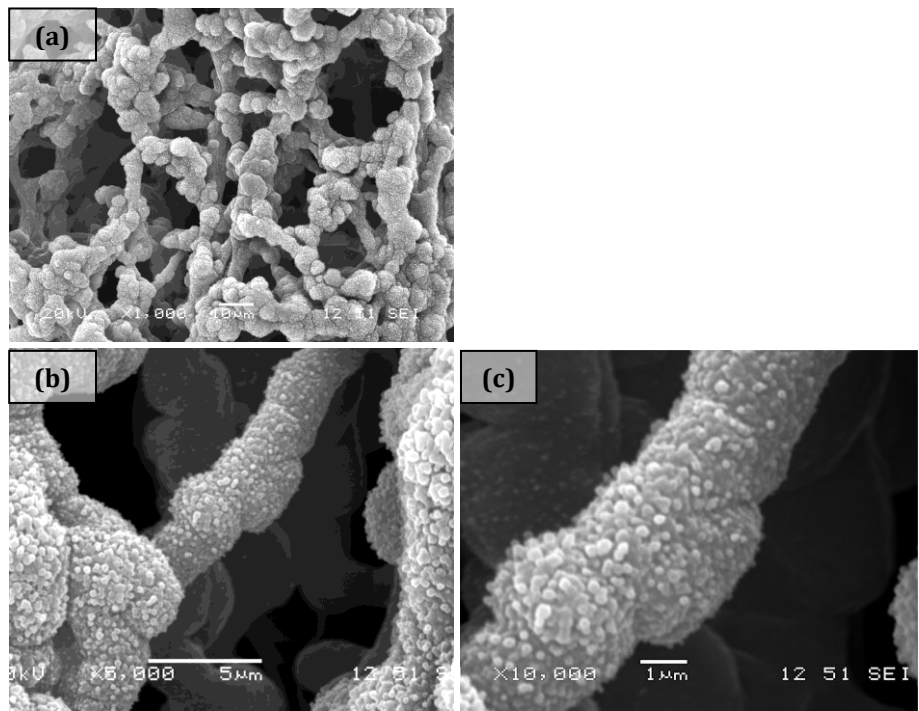


Figure 4.21 SEM micrographs of structure generated on Rice husk at laser rep. of 26 MHz, dwell time of 0.05 ms, and power of 10W at magnification of a) X1K, b) X5K, and c) X10K.

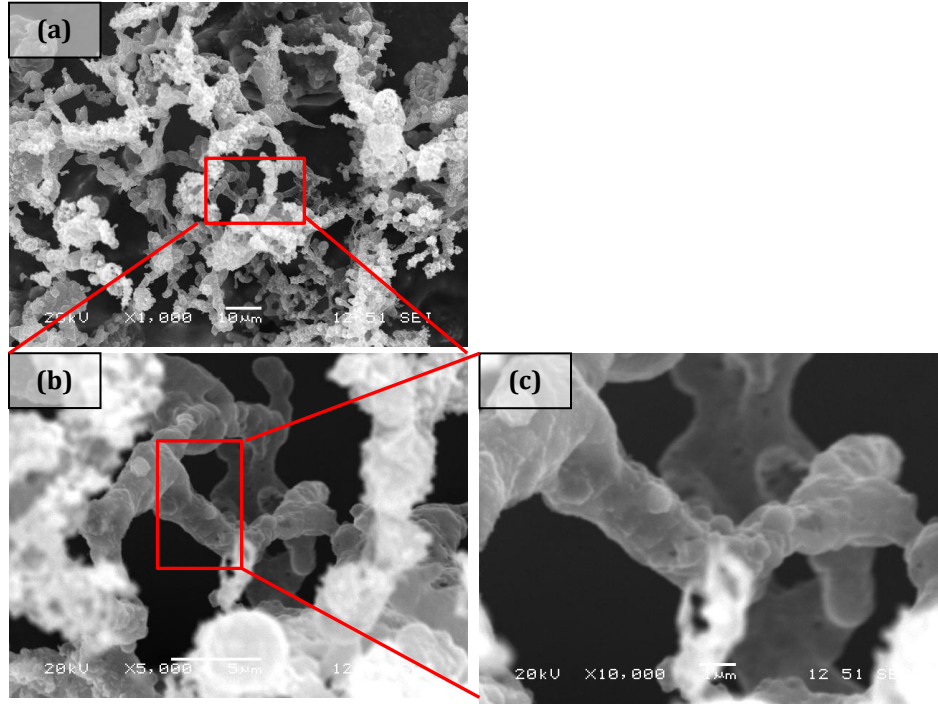


Figure 4.22 SEM micrographs of structure generated on wheat straws at laser rep of 26 MHz, dwell time of 0.05 ms, and power of 15W at magnification of a) X1K, b) X5K, and c) X10K.

This proposed method suggest a promising step in synthesizing interwoven 3-D platforms from natural biomaterials to support new bone formation and achieve rapid bone healing as well as to improve develop new functional biomaterials for various biomedical applications. However, *in vitro* and *in vivo* studies (e.g., cell proliferation and cell adhesion) are required to confirm the claim.

4.4 Summary

This chapter investigated experimentally and theoretically, the formation mechanism of web-like 3-D nanofibrous structure by femtosecond laser ablation of biomaterial target at background air. The results showed that femtosecond laser ablation of Ti target at air background resulted in the formation of crystalline titania nanostructures.

The formation of crystalline titania nanostructures was preceded through thermal mechanism of nucleation and growth. In addition at the presence of air, collisions between the gas atoms and the surface markedly reduce the lifetime of this non-equilibrium surface state which allows thermal evaporation to proceed before the surface cools. The femtosecond laser pulse interaction with titanium substrate at ambient air was explained using a simple and straightforward analytical model. The formulas for evaporation rates and the number of ablated particles for the ablation by a single pulse and multiple pulses as a function of laser parameters, background gas and material properties were derived and compared to experimental results. The calculated dependence of the evaporation rate on the pulse repetition and laser pulse dwell time was in accordance with the experimental data. Also, the formation of nanofibrous structures was demonstrated by applying an existing simplified kinetic model to Ti target and ambient condition. The results showed that laser pulse repetition could control the density, size, and pore size of engineered nanofibrous structure. It also described that this technique allows the synthesis of micro/nanofibrous structure on natural biomaterial including eggshell, rice husk, and wheat straw. To the best of our knowledge, this is the first time that synthesizing 3-D micro/nanofibrous structures generated on natural biomaterials using femtosecond laser have been reported.

CHAPTER 5

DIRECT NANOSTRUCTURE INTEGRATION INTO OTHER STRUCTURES

In this chapter, the potential use of the presented technique for fabricating integrated nanostructures on transparent platforms as well as inside microstructures is investigated. Presented studies show that integrated nanostructure inside microchannels can be fabricated in one single step using this technique. In addition, femtosecond laser induced reverse transfer (LIRT) is used for controllable site-specific deposition of nanostructure on transparent platforms.

5.1 Incorporation of Nanofibrous structures on Transparent Platform¹

This section demonstrates that Laser induced reverse transfer (LIRT) can be used for controllable site-specific deposition of fibrous nanostructure. The LIRT method makes it achievable to generate and deposit fibrous nanostructure of metallic and semiconductor targets on transparent acceptor in a single step process at an ambient condition. The deposition of fibrous nanostructure was conducted using ultrafast laser ablation of silicon and aluminum targets placed behind a glass acceptor. Femtosecond laser pulses pass through the transparent acceptor and hit the bulk donor. Consequently a mass quantity of nanoparticles ablates from the donor and then aggregates and forms a porous fibrous nanostructure on the transparent acceptor. Our experiments show that the gap between the target and the glass acceptor was critical in the formation and accumulation of nanofibers and it determines the density of the formed nanostructure. The formation mechanism of the nanostructures can be explained by the well-established theory of vapor condensation within the plume induced by ultrafast laser ablation. Experimental results also show that the length of the nanostructure can be controlled by the gap between the target and glass acceptor. Lastly, EDS analysis shows the oxygen concentration in the nanofibrous structure which is associated with oxidation of ablated material at ambient atmosphere.

¹ Reprinted from Journal of Micromechanics and Microengineering, 20, A. Tavangar, B. Tan, and K. Venkatakrishnan, Deposition of fibrous nanostructure by ultrafast laser ablation, pp. 055002, Copyright (2010), with permission from IOP Publishing. The dissertation author was the primary investigator and author of this article.

5.1.1 Laser-induced reverse transfer LIRT

Laser-induced forward transfer (LIFT) has been widely studied as a method for direct deposition in predetermined micro-patterns [127–129]. In this method, prior to the laser irradiation a donor thin film is deposited on a transparent support substrate. The ablation of the thin film generates a fast travelling plume that deposits ablated material onto an acceptor substrate which is placed after the donor substrate [130]. Due to the fine spatial resolution of a laser spot, materials can be deposited in desired patterns in micron and sub-micron scale [131], [132]. LIFT process can be performed in air and at room temperature.

Alternatively, backward-LIFT (Laser-induced reverse transfer LIRT) can be used, where the donor substrate is placed after the acceptor substrate along the laser propagation direction. In LIFT, laser ablates the donor thin film from the bottom after transmitting through the transparent support substrate. This imposes limitation on the applicability of LIFT, since some materials are not easy to be processed into thin films. Unlike LIFT, LIRT ablates donor material from the front side of the donor substrate. Therefore, donor materials need not to be thin films; instead bulk materials can be used as donors [131]. On the other hand, LIRT requires transparent acceptor which restrains its applications.

Recently, researchers have begun to exam the potentials of using LIFT for nano-material deposition due to the continuous interest in nanotechnology. For example, M LA Rigout et al [132] used a two-step LIFT method to form chain-like silicon nano-wire networks.

This work demonstrates that LIRT can be utilized to generate and deposit metallic and semiconductor nanofibrous structures on a transparent acceptor under ambient conditions. It is found that the distance between metallic and silicon target and glass acceptor has significant influence on the density of fibrous nanostructure.

5.1.2 Experimental detail and fabrication process

Experiments were conducted with a 515 nm wavelength direct-diode-pumped Yb-doped fiber amplified ultrafast laser system. The general laser-induced reverse transfer process is shown schematically in Figure 5.1. The femtosecond laser beam transmits through the transparent acceptor and hits the donor substrate. The plume generated from the donor target surface propagates reversely to the glass acceptor and ejected species agglomerate into nanoparticles which form interwoven nanofibers by further collision.

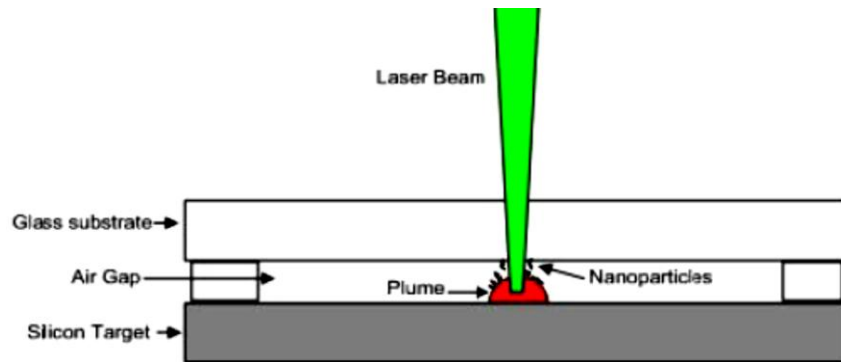


Figure 5.1 Schematic of Laser-Induced Reverse Transfer process

5.1.3 Results and discussions

When the laser intensity surpasses the ablation threshold of a target, the irradiation creates a plasma plume that consists of three propagation fronts of different velocities. The first front is the fastest and it contains vaporized atoms and ions. Due to the small size of

atoms and ions, this front is very thin. The second front which starts after the atomic front has lower velocity and mostly consists of clusters. This front makes the majority of the emitted species [60], [133]. The third front has the longest delay and contains a small amount of molten liquid droplets in micron or submicron size. The bigger the particle size, the shorter it can travel. Therefore, the molten liquid droplets propagate the least distance in comparison with the two other fronts. As the plasma expands outward, the plume's temperature and pressure start to decrease, leading to the nucleation and consequently the growth of nanoparticles [134], [135]. In the case of multiple-pulse irradiation, massive nanoparticle agglomeration takes place if the subsequent pulse arrives before the plume cools below the vaporization point. The agglomerates can be recognized by their chain or web shape. In LIRT process, when a laser pulse is irradiated to the donor substrate, the plasma created on its surface propagates backward at high speed to the transparent acceptor placed close to it. As a result, dependent on the distance between the acceptor and the donor substrate, formation and emission of various particle sizes on the acceptor may happen.

Previously, it was revealed that the formation of fibrous structure is possible only if the pulse frequency was higher than 1 MHz and the density of nanoparticles and consequently the generated nanofibers are maximized at 13 MHz [112]. Thus, the experiments in this study were conducted at a frequency of 13 MHz in order to obtain the highest amount of nanofibers. In this study, LIRT technique is utilized to ablate silicon or metallic donors and generate nanofibrous structure on the transparent acceptors placed in close proximity of the target.

First, the ablation process was performed with a silicon wafer (donor) and a glass acceptor in near contact. Although deposition was presented on the acceptor, no fibrous nanostructures were generated, instead droplets in sub-micron size were observed, as shown in Figure 5.2. Extremely short spacing between the acceptor and the donor restricts the plume expansion and condensation process, resulting in reduction of the nuclei formation onset, hence, leading to formation of large particles [134], [136]. On the other hand, due to very small separation, molten liquid droplets are able to reach the acceptor surface and deposit.

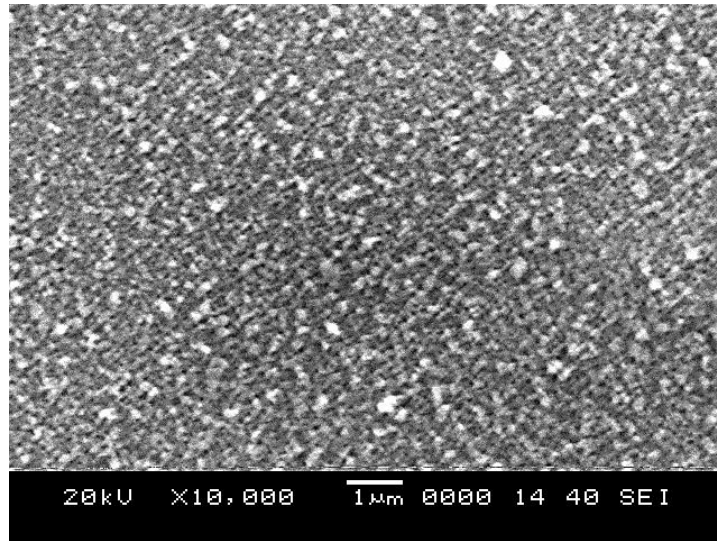


Figure 5.2 SEM image of Aluminum deposition formed by laser beam of 515 nm wavelength, at freq. of 13 MHz and machining velocity of 1000 mm/s.

The role of substrate distance was thoroughly discussed in LIFT techniques [130], [137], [138]. Based on this knowledge, it was estimated that a suitable separation of 60 μm should be able to result in nanofiber deposition, taking into account the laser fluence and the target material. This spacing allows more room for plume expansion, leading to a longer plume propagation length. A longer plume length yields a lower concentration of

ablated species in the plume which results in smaller clusters [134], [136]. Figure 5.3 presents the fibrous nanostructures obtained with the 60- μm spacing. However, a small amount of large droplets is still visible from a close-up of the nanostructure, as shown in Figure 5.3b. This suggests that under the current experimental condition, a spacing of 60 μm is not sufficient to completely avoid molten liquid droplet deposition. Direct emission of liquid phase fragments from the donor surface to the acceptor still happens on a smaller scale due to the inadequate space.

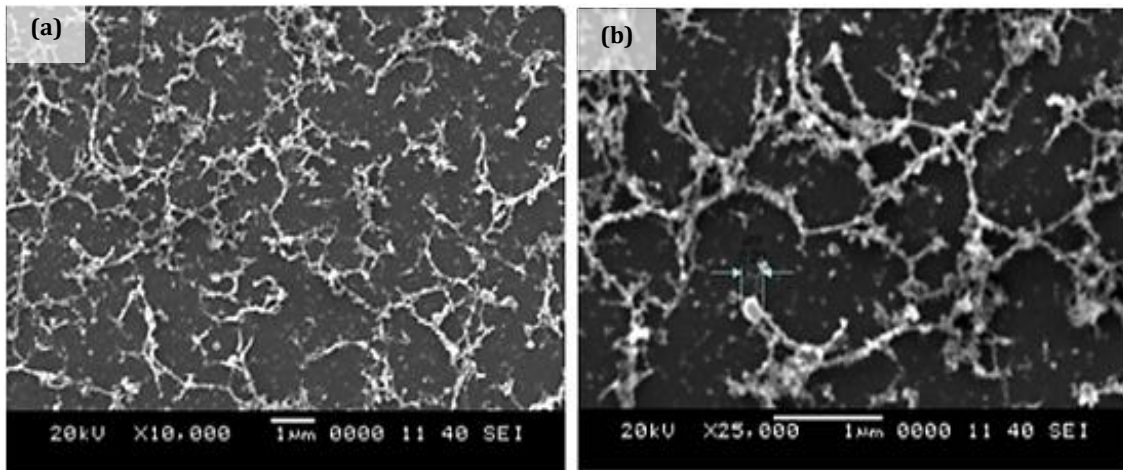


Figure 5.3 SEM image of silicon nanofibers deposited on a glass acceptor with gap of 60 μm and formed by laser beam of 515 nm wavelength, at frequency of 13 MHz and machining velocity of 1000 $\mu\text{m/s}$ at magnification of a) X1000 and b) X25000.

The experiment was continued with wider gaps at 120, 180 and 240 μm in order to investigate the influence of the target and acceptor distance on the nanofibrous structure. As shown in Figure 5.4, the density and length of fibers are more than those on an acceptor with a gap of 60 μm . The average length of nanofibers obtained at the 60 μm gap was in the range of 0.55 μm to 0.70 μm whereas, it was about 1.06 μm to 1.18 μm for those obtained at the 120 μm gap. Comparing Figure 5.3 and Figure 5.4, it was found that the large droplets

diminished in size and amount. Besides, as the gap between the target and the acceptor increased, deposited nanofibers became thinner.

The experiment was repeated with other target materials such as aluminum, and graphite. It was found that, the aggregations can be deposited from metals, carbon and semiconductors. Alloy targets composed of these elements were also found to generate fibrous nanostructure by ultrafast laser irradiation.

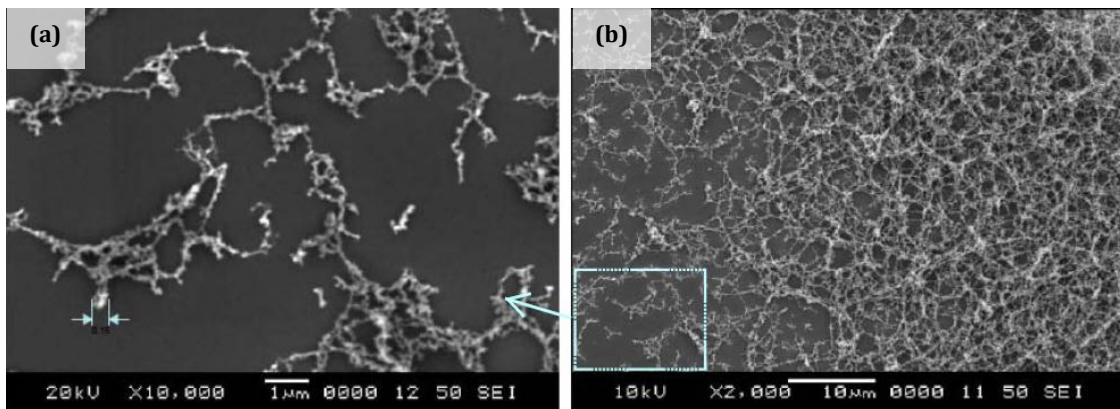


Figure 5.4 SEM image of silicon nanofibers deposited on a glass substrate with gap of 120 μm and formed by laser beam of 515 nm wavelength, at frequency of 13 MHz and machining velocity of 1000 mm/s at magnification of a) X10000 and b) X2000.

Figure 5.5 depicts nanofibers that were generated in parallel lines. It demonstrates that deposition of nanofibers can be carried out at specific sites. Comparing Figure 5.5a and Figure 5.5b, it can be seen that the density of nanofibers increased with the increase in the gap between the glass acceptor and the donor.

Figure 5.6 shows a spot ablated with a stationary laser beam. Nanofiber density is the maximum at the center of the spot and decreases with the increase in the radial distance from the center of the laser spot. At larger distances, the density of the nanofibers falls dramatically. This observation agrees well with previous study on spectroscopy of

laser-ablated silicon plasma related to nanoparticle formation [139]. The spatial dependence shows the reduction in temperature and density with the increase in distance. The high plasma pressure causes a lateral plasma compression wave, leading to change in energy distribution on the target, which explains the density variety of deposition along the radial direction [139].

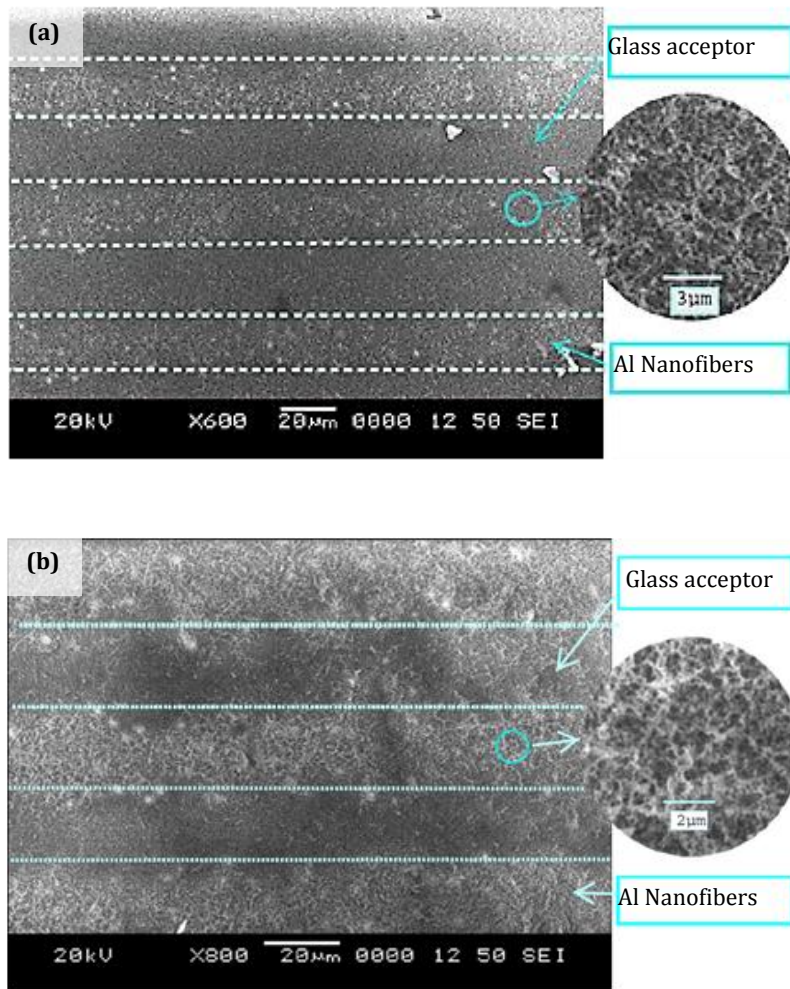


Figure 5.5 SEM image of Aluminum nanofibers deposited on a glass acceptor with a) gap of 60 μm and b) gap of 180 μm formed by laser beam of 515 nm wavelength, at frequency of 13 MHz and machining velocity of 1000 mm/s.

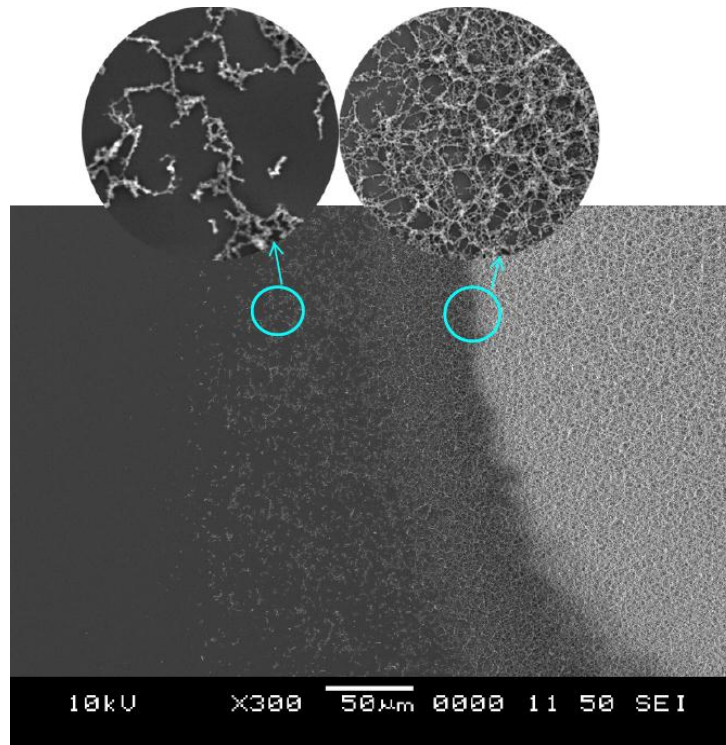


Figure 5.6 SEM image of three different zones of silicon nanofibers deposited on a glass acceptor with gap of 120 μm and formed by laser beam of 515nm wavelength, at frequency of 13 MHz and machining velocity of 1000 mm/s.

In order to examine the composition of nanofibrous structure, EDS analysis was carried out. As depicted in Figure 5.7, EDS analysis of aluminum nanofibrous structure on the glass acceptor showed Si, Ca and O together with aluminum. To investigate whether these elements belong to the glass acceptor or the nanofibrous structure, EDS analyses of glass acceptor with and without nanofibrous structure were compared. By comparison between those results, it was concluded that only oxygen concentration is higher in the nanofibrous structure and other elements belonged to the glass acceptor. Since the LIRT process is performed at atmospheric ambient, oxidation of ablated nanoparticles occurs, which results in the generation of metallic or silicon oxide nanofibrous structure. In order to confirm the nanofiber composition and precise measurement of oxygen level, EDS

analysis was obtained for silicon nanofibers which were directly generated on pure Si substrate. As shown in Figure 5.8, for Si nanofibers, the presence of O along with Si agrees with EDS analysis of Al.

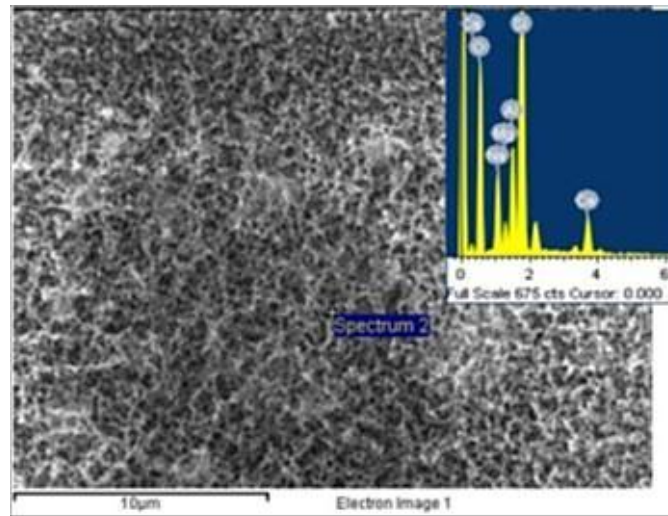


Figure 5.7 EDS analysis of aluminum oxide nanofibers deposited on a glass acceptor.

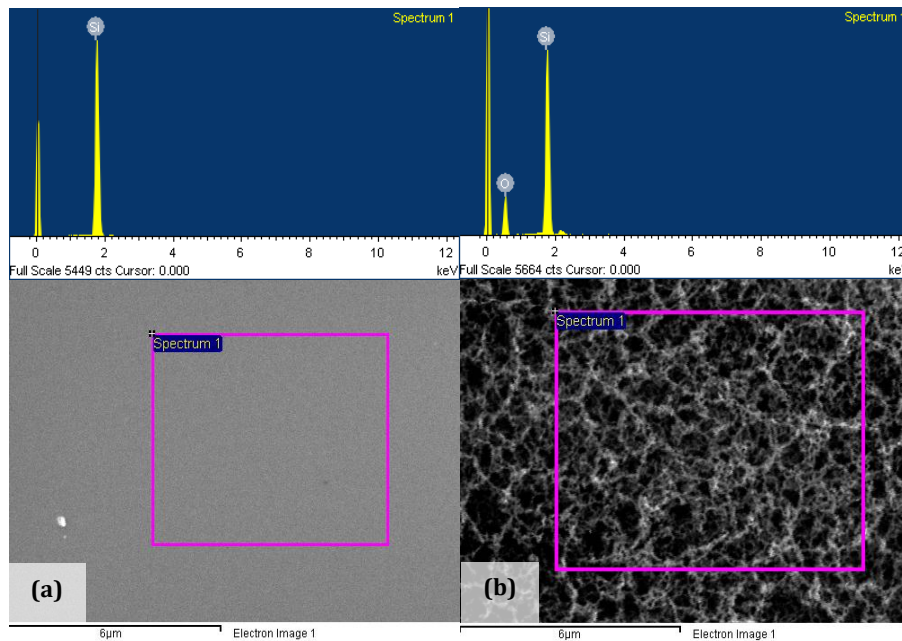


Figure 5.8 EDS analysis of a) pure Si and b) silicon oxide nanofibers deposited on a Si substrate.

5.2 Single-step Generation and Incorporation of Nanofibrous Membrane into Microchannels¹

This section demonstrates a new method to fabricate silicon microfluidic channels filled with porous nanofibrous structure utilizing a femtosecond laser. The nanofibrous structure can act as a membrane used for microfiltration. This method allows us to generate both the microfluidic channel and the fibrous nanostructure in a single step at ambient condition. Due to the laser irradiation, a large amount of nanoparticles ablates from the channel surface and then aggregates and grows into porous nanofibrous structures and fills the channels. EDS analysis was conducted to examine the oxygen concentration in the membrane structure. The results show that by controlling the laser parameters including pulse repetition, pulse width, and scanning speed, different microfluidic channels with a variety of porosity can be obtained.

5.2.1 Membranes

The usage of membranes in microfluidics has been growing rapidly [140]. Various recent studies have concentrated on the evolvement of membranes with nanometer-scale pores [9], [141–143]. Several methods have been developed to fabricate nanoporous membranes such as lithography [65], [144], [145], ion track technique [146], self-organization [147], and sol-gel [91]. Most of these methods suffer from manufacturing

¹ Reprinted from Journal of Micromechanics and Microengineering, 20, A. Tavangar, B. Tan, and K. Venkatakrishnan, Single-step fabrication of microfluidic channels filled with nanofibrous membrane using femtosecond laser irradiation, pp. 085016, Copyright (2010), with permission from IOP Publishing. The dissertation author was the primary investigator and author of this article.

complexity either in lithography processes or during membrane assembly to the microfluidic systems [141]. Despite its easy control on pore diameter and simple fabrication procedure, the ion track technique has limitations owing to both the inefficiency caused by the thick membrane and the inconvenient deployment in other microfluidics systems. In the sol-gel technique, the material is too costly and a ceramic support layer, fabricated by solid state sintering, is required [148]. Therefore, this chapter reports a new laser application for fabrication of nanoporous membranes inside microfluidic channels which provides high controllability on average pore sizes. It is interesting to note that our proposed method generates both the porous nanofibrous structure and the microfluidic channel in a single step under ambient condition. The nanoparticles are fused together rather than loosely bonded. Thus, it's assumed that the bond structure of aggregation and the channel is strong. Also, It's determined that the pore size and density in the membrane can be controlled through adjustment of the laser parameters and laser scanning procedure.

5.2.2 Experimental details

Experiments were performed with a 1040 nm wavelength direct-diode-pumped Yb-doped fiber amplified ultrafast laser system. The target was a polished silicon wafer with <100> crystal orientation and 550 μ m thickness. The schematic diagram of the fabrication process is shown in Figure 5.9.

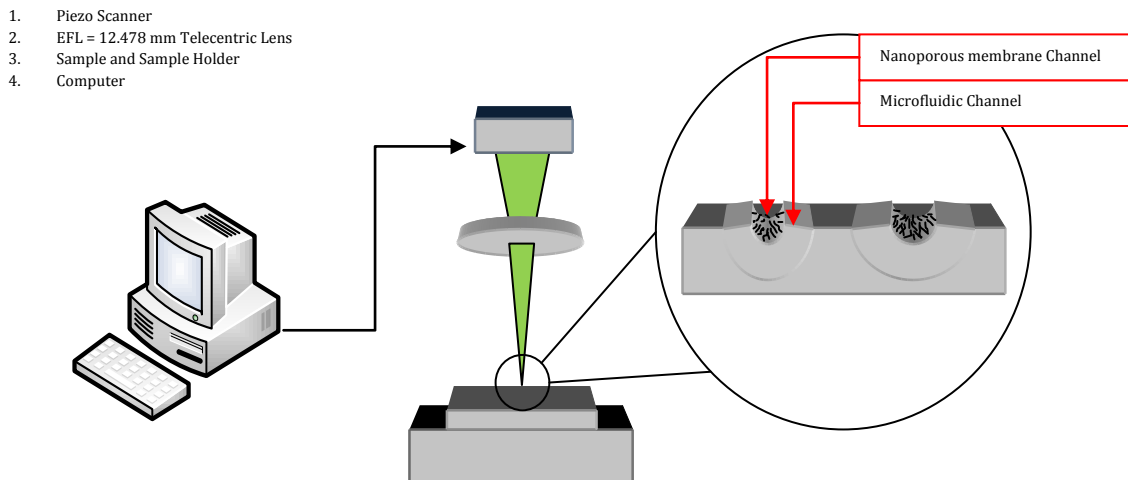


Figure 5.9 Fabrication set up

5.2.3 Results and discussions

5.2.3.1 *The growth mechanism of nanofibrous structure*

Primary experiments were conducted to investigate laser scanning strategies for the creation of a microchannel filled with nanofibrous structure including laser scanning speed and number of passes. The close scheme of the nanofiber growth mechanism in a microchannel and its cross-sectional view is shown in Figure 5.10.

Basically, emitting a laser beam at a target creates a heated region which causes vaporization leading to plasma that consists of electrons and ionized atoms. As the plasma expands outward, due to heat transfer at the contact surface between the plume and the ambient gas, the vapor plume starts to cool down and condensation begins at the cooler front of the plume cloud [149], [150]. Condensation of the vaporized atoms leads to nucleation and consequently the growth of nanoparticles [135]. Nanoparticle aggregation

takes place as a part of vapor condensation by the collision of nucleus. An immense amount of nanoparticle aggregation is required in order to generate nanofibrous structures. Therefore, continuous arrival of the plume is needed before the pulse cools below the vaporization point. A close view of the nanofibrous structures exhibits that the nanoparticles are mostly fused together instead of loosely linked. The structures are made of self-assembled closed ring and bridge nanofibers. Therefore the bond between the aggregated structure and the channels assumed to be strong.

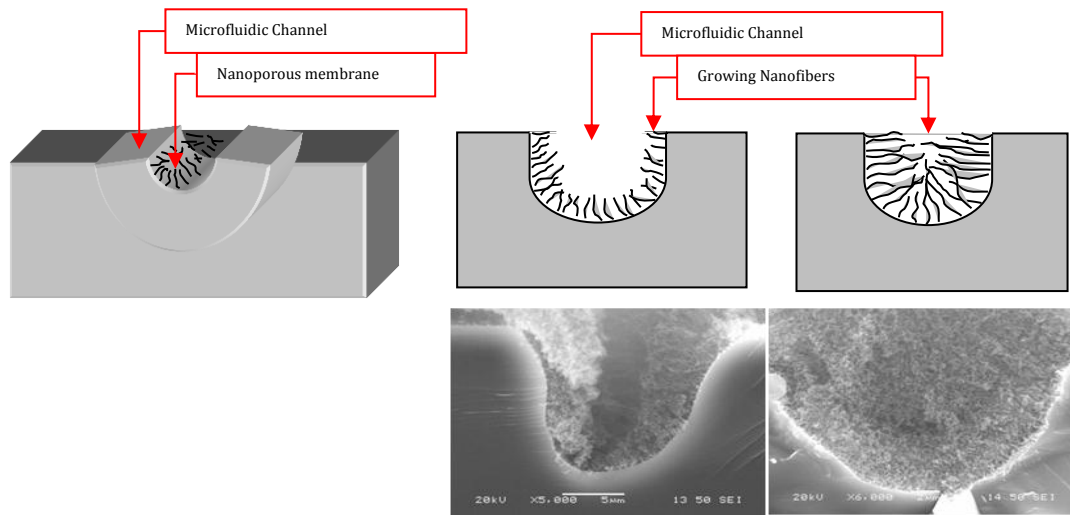


Figure 5.10 3-D and plane view of the microchannel and sequences of nanofiber growth inside the microchannel. The related SEM images corresponding to each sequence are brought on the bottom. The microchannels were formed by laser beam at freq. of 13 MHz with laser scanning speed of 1000 mm/s after a) 5 and b) 20 scanning passes.

As mentioned above, the plumes generated by sequential laser pulses have to arrive at the target before the critical time. Hence, the formation of fibrous structure is not possible in the high speed laser machining. Therefore, as the first step, optimum laser machining speed must be defined. As the machining speed decreases, interaction time

between laser beam and the target increases, leading to a higher laser pulse per spot on the target which consequently results in a higher amount of nanofiber agglomeration. On the other hand, by controlling the laser scanning passes, a variety of microchannels with different depth and width can be achieved.

5.2.4 Effect of laser scanning parameters

As depicted in Figure 5.11, it was found that at low laser scanning speeds and high scanning passes the depth of the microfluidic channel increases and its width decreases. In the case of high number of laser scanning passes, more fibrous structure is generated. In addition to its effect on the amount of generated nanofibrous structure, laser scanning speed influences the microchannel shape as well. Comparing Figure 5.11a and Figure 5.11b, at lower scanning speed (Figure 5.11a), a narrower channel was formed because of more dwell time on the specific spot and consequently higher energy per pulse. Conversely, at higher speed (Figure 5.11b), the plumes generated by sequential laser pulses could not arrive at a particular spot before the critical time needed to maintain the nucleus density at the certain level; therefore, no nanofibers were generated.

Figure 5.12 shows the growth mechanism of nanofibrous structure for different laser scanning passes. Firstly, microchannels were generated at high scanning speed with few scanning passes. As mentioned before, at higher speed, due to low interaction time between the laser and the substrate, no fibrous structure was generated and only the microchannel was formed. Afterwards, low scanning speed was employed to grow nanofibers inside the channel. As the number of scanning passes increases, more fibrous structures grow on the microchannel walls.

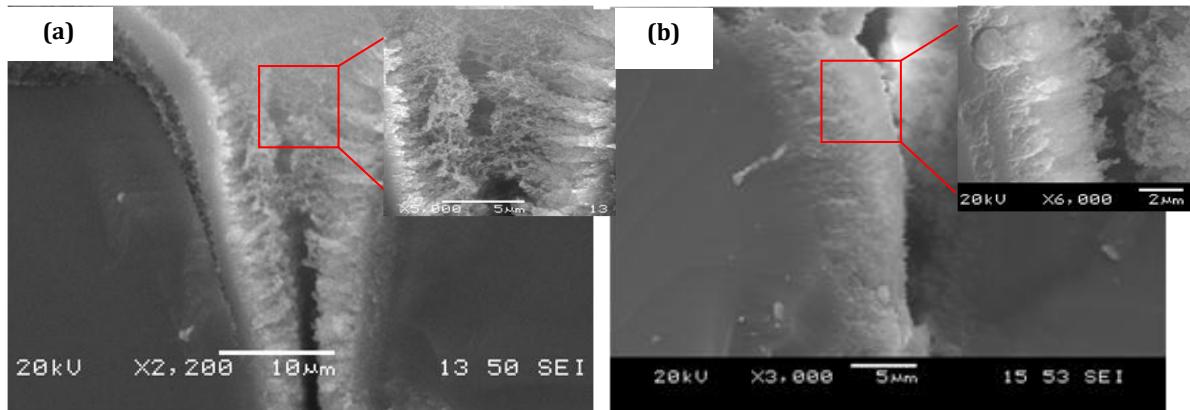


Figure 5.11 SEM cross sectional image of nanofibrous structure inside a microfluidic channel formed by laser beam at freq. of 13 MHz with laser scanning speed of a) 1000 mm/s and b) 2000 mm/s.

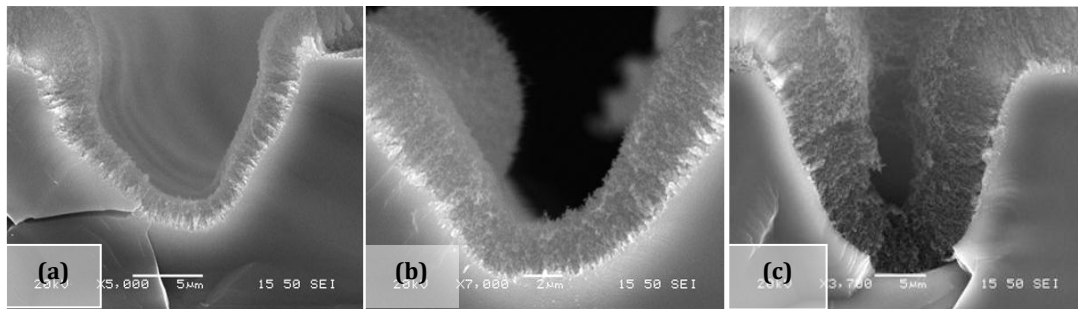


Figure 5.12 SEM cross sectional image of nanofibrous structure growth sequences inside the microfluidic channel formed by 1040 nm wavelength laser beam at freq. of 26 MHz after a) 5, b) 10, and c) 20 laser scanning passes.

5.2.5 Study of pore size and density of nanofibrous structure

SEM analyses of nanofibrous structure revealed that laser repetition rate and laser pulse width have an important impact on the pore size and density of the fibrous structure.

5.2.5.1 *Effects of laser repetition rate*

After finding the optimum laser scanning strategy, the effects of the laser repetition rate on both the shape of the channels and the porosity of the nanofibrous structure were determined.

In the case of multiple-pulse irradiation, a massive nanoparticle agglomeration takes place if the succeeding pulse arrives before the pulse cools below the vaporization point. Therefore the experiments were conducted at the frequencies of 8, 13, and 26 MHz to obtain the most nanofibrous structure. Note that in these experiments the time interval between pulses is about 125 ns, 77 ns and 38 ns for the frequencies of 8, 13, and 26 MHz, respectively. One of the distinguishing characteristics of these nanofibrous structures, unlike the random heaping of particles observed at Hz and kHz pulse frequencies, is that the fiber aggregation shows a certain degree of organization.

Pore size data were extracted directly from the SEM images using image processing software. SEM images of these membranes (see Figure 5.13) revealed that membrane pore size decreases as the pulse repetition rate increases, whereas the density of pores increases with increasing pulse repetition rate. However pore size distribution is wider for 13 MHz repetition in comparison with the two other frequencies. This heterogeneity might be caused when the channels got cut for cross section imaging. Membranes have an average pore diameter of 492 nm, 313 nm, and 254 nm at the frequencies of 8, 13, and 26 MHz, respectively. The minimum pore diameter has been calculated to be approximately 90 nm at repetition of 26 MHz.

At the pulse repetition rates higher than the nanoparticle formation threshold, consecutive laser pulses hit the substrate before the ablated particles from the previous pulse cool down. As a result, nanoparticles ejected by the following laser pulses prefer to aggregate with particles ablated from the former laser pulses which are still at a very high temperature, resulting in an increase in nanofibrous structure density. Moreover, since laser power and laser spot size are constant, the pulse energy decreases as the pulse repetition increases which results in a reduction in nanoparticle size. Consequently, because of the smaller nanoparticle size, nanofibers become finer, leading to the lessening of the pore size (see Figure 5.13).

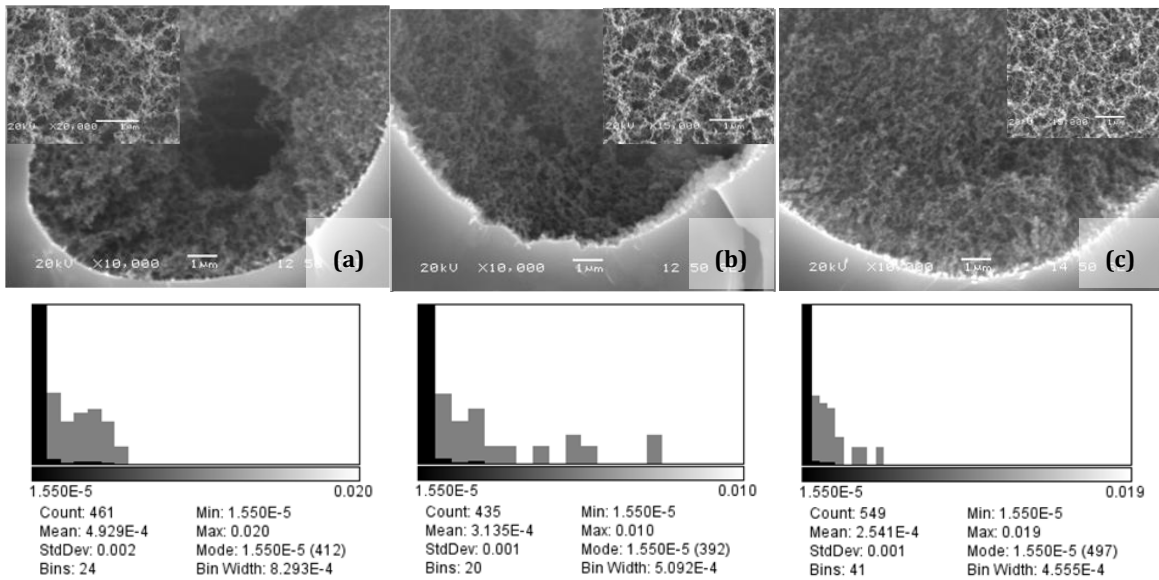


Figure 5.13 SEM cross sectional image and pore diameter distribution graph of nanofibrous structure inside the microfluidic channel formed by laser beam of 1040 nm wavelength, at freq. of a) 8 MHz b) 13 MHz, and c) 26 MHz

5.2.5.2 *Effects of laser pulse width*

Afterwards, influence of the laser pulse width on the membrane pore size was investigated. The laser used for all the presented experiments has the ability to work with different pulse widths from 214 fs to 3.5 ps.

To investigate the influence of different laser pulse widths on the porosity of the membrane, experiments were conducted at the repetition of 26 MHz with the same laser scanning speed and number of passes, but with different pulse widths of 214, 1428 and 3500 fs (see Figure 5.14). The experiments showed that as the pulse width goes to the femtosecond scale, less nanofibrous structure is generated. As the pulse width decreases from picoseconds to femtoseconds, the interaction time between the laser pulse and the substrate decreases. This causes a decrease in size of the nucleus which forms the nanoparticles. Accordingly, the size of nanofibers decreases. As a result, the smaller nanofibers lead to the pore size reduction (see Figure 5.14). The average pore diameter of the membranes were about 378 nm, 753 nm, and 832 nm at pulse widths of 214 fs, 1428 fs, and 3500 fs, respectively. The smallest pore diameter was estimated to be around 160 nm at 3500 fs pulse width.

Finally, in order to examine the composition of nanofibrous structures, EDS analysis was performed. Figure 5.15 depicts the EDS analyses comparing generated nanofibrous structures with an un-doped Si wafer. Since experiments were carried out at an ambient condition, the presence of oxygen along with silicon (Si) is noticeable for the nanofibrous structures.

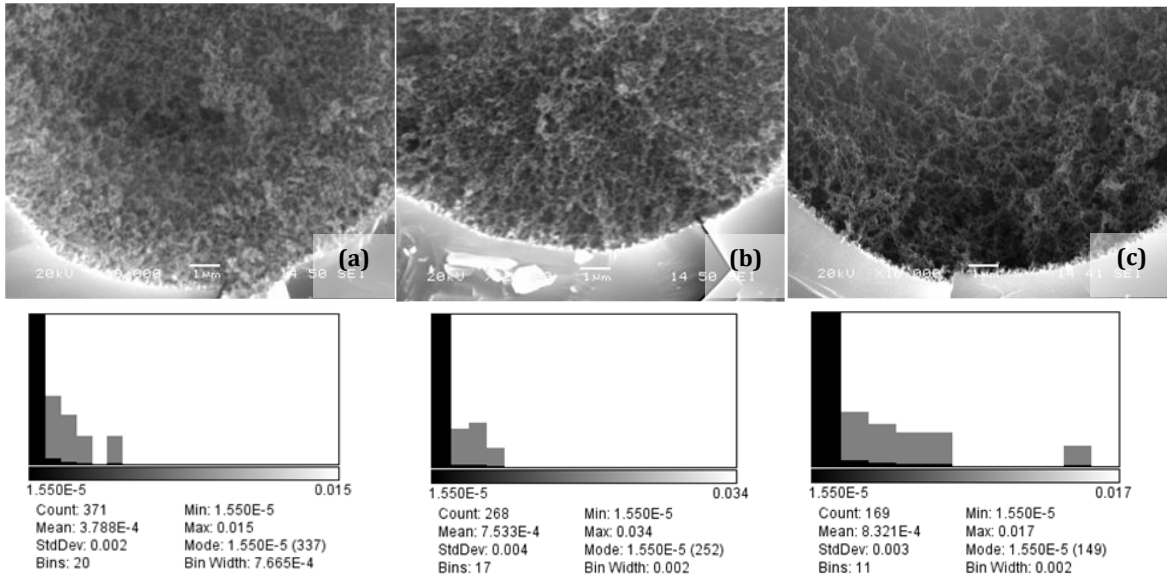


Figure 5.14 SEM image and pore diameter distribution graph of nanofibrous structure inside the microfluidic channel formed by laser beam at freq. of 26 MHz with pulse width of a) 214 fs, b) 1428 fs, and c) 3500 fs.

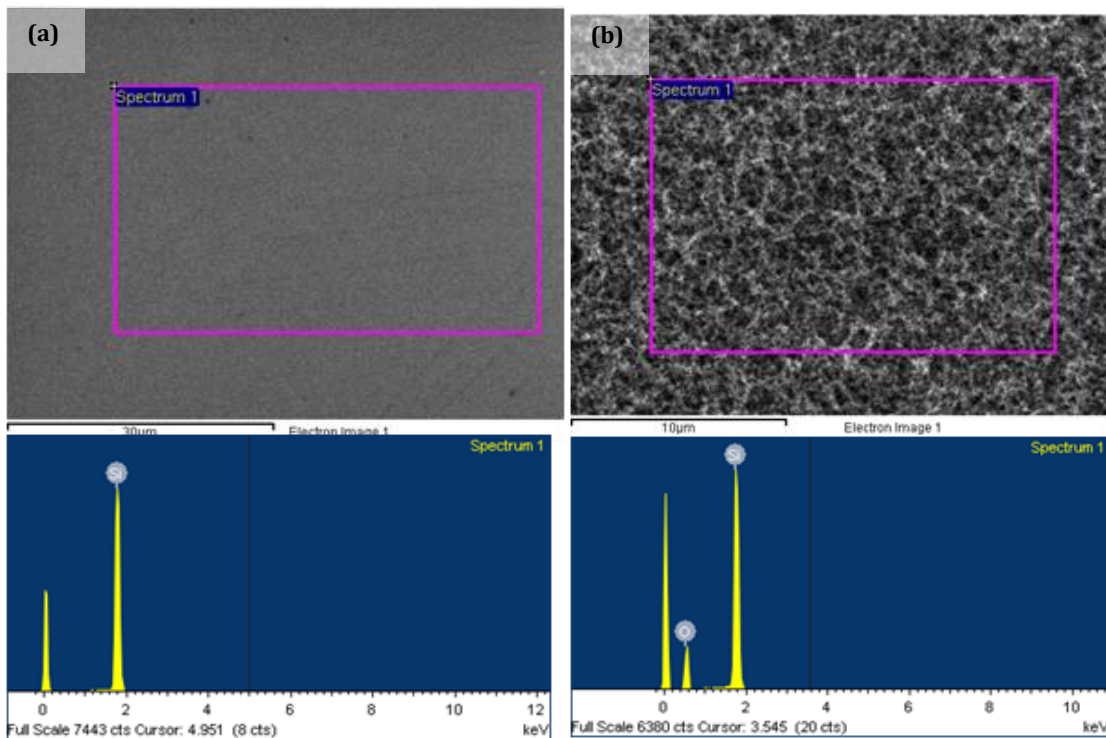


Figure 5.15 Energy dispersive X-ray spectroscopy (EDS) analysis of a) pure Si and b) silicon oxide nanofibers deposited on a Si substrate.

5.3 Summary

In this section, the deposition of metallic and semiconductor fibrous nanostructure on a transparent acceptor was demonstrated. It was found that the gap between the glass acceptor and the target plays a crucial role in the nanostructure formation and the density of nanofiber accumulation. Experimental results also show that size, length, density of aggregates and location of growth can be controlled by laser parameters under an ambient condition. The precise controllability of this fibrous nanostructure deposition will extend the application of this invention. Generation and deposition of nanofibrous structure was completed in a single step at an ambient condition. This method may find wide applications. Also, a development of a new method for fabricating silicon dioxide nanofibrous membranes grown inside microchannels was reported. The experiments showed that by controlling the laser parameters including pulse repetition, pulse width and scanning speed, different microfluidic channels with different porosity and pore density could be obtained. The EDS analyses indicated oxygen concentration in the membrane structure which was attributed to oxidation of ablated material at ambient atmosphere. Using this strategy, the microchannel and the fibrous nanostructure for a wide variety of materials can be generated in a single step at ambient condition. This achievement can in the future pave the way for extensive application of nanofilters in various membrane, filtration, and separation applications.

CHAPTER 6

BIOASSAY OF MANUFACTURED PLATFORMS

This chapter presents studies which demonstrate the *in vitro* analyses of the synthesized platform. The bioactivity of the synthesized structures is assessed using SBF with ion concentrations approximately equal to those of human blood plasma. Also, the interaction of the platforms with living cells is examined using different *in vitro* techniques. Cell-based assays such as cell adhesion, cell proliferation, and cell viability assay are carried out to evaluate the biocompatibility between cells and implanted scaffold.

6.1 Bioactivity assay of synthesized 3-D Titania Nanofibrous Platforms¹

The primary objective of current tissue regeneration research is to synthesize nano-based platforms that can induce guided, controlled, and rapid healing. Titanium nanotubes have been extensively considered as a new biomaterial for biosensors, implants, cell growth, tissue engineering, and drug delivery systems. However, cell adhesion to nanotube is poor due to their chemical inertness as well as one-dimensional structure and surface modification is required to enhance nanotube-cell interaction. While there are considerable studies on growing titanium nanotubes, synthesizing a 3-D nano-architecture which can act as a growth support platform for bone and stem cells has not been reported so far. In previous chapters the development of the laser ablation technique to synthesize and grow 3-D titania interwoven nanofibrous structures on titanium substrate has been reported. This surface architecture incorporate the functions of 3-D nano-scaled topography and modified chemical properties to improve osseointegration while at the same time leaving space for delivering other functional agents. It has been suggested that the crucial requirement for a synthetic biomaterial to bond to living bone is the formation of bonelike-apatite on its surface when implanted in the living body. This *in vivo* apatite formation can be mimicked in a SBF with ion concentrations nearly equal to those of human blood plasma [151]. The goal of the presented work is to evaluate the bone-like apatite-inducing ability of

¹ Reprinted from Acta Biomaterialia, 7(6), A. Tavangar, B. Tan, and K. Venkatakrishnan, Synthesis of bio-functionalized three-dimensional titania nanofibrous structures using femtosecond laser ablation, pp. 2726–2732, Copyright (2011), with permission from Elsevier. The dissertation author was the primary investigator and author of this article.

the Ti surface with different morphology using SBF. Ti surfaces with different morphology are synthesized by altering laser pulse repetition. The results indicate that laser pulse repetition can control the density and pore size of engineered nanofibrous structure. In vitro experiments reveal that the titania nanofibrous architecture possesses an excellent bioactivity and can induce rapid, uniform, and controllable bone-like apatite precipitation once immersed in SBF. This approach for synthesizing 3-D titania nanofibrous structures suggest considerable outlook for promoting Ti interfacial properties to develop new functional biomaterials for various biomedical applications.

6.1.1 Experimental detail

6.1.1.1 *Generating nanofibrous structures*

Specimens were irradiated by laser beam at laser pulse repetitions of 4, 8, and 12 MHz to generate nanofibrous structures with different density and pore size. The Ti samples processed at pulse repetitions of 4, 8, 12 MHz are referred to as: Ti4, Ti8, and Ti12, respectively. The laser pulse width, power and scanning dwell time were 214 fs, 15 W, and 5 ms, respectively.

6.1.2 Sample SBF soaking for in vitro assessment

The effect of surface morphology on its apatite-inducing ability was evaluated by soaking the samples in SBF with ionic concentration nearly equal to the human blood plasma (see Table 6.1). A modified simulated body fluid (m-SBF) was prepared by dissolving the following reagents in sequence in distilled water: NaCl, NaHCO₃, Na₂CO₃, KCl, K₂HPO₄·3H₂O, MgCl₂·6H₂O, CaCl₂, and Na₂SO₄. The solution

was buffered to pH 7.40 with 4-(2-hydroxyethyl)-1-piperazineethanesulfonic acid (HEPES) and 1 M NaOH at 37 °C [14]. Each Ti sample was then placed in a sterilized container with 30 ml SBF and kept in an incubator at 37 °C for 1 and 3 days. After exposure, the samples were removed and washed thoroughly with distilled water and dried in desiccators for further characterisation.

Table 6.1 Ion concentration of m-SBF in comparison with blood plasma, taken from [152]

Ion	Ion concentration (mM)	
	Blood Plasma	m-SBF
Na ⁺	142.0	142.0
K ⁺	5.0	5.0
Mg ²⁺	1.5	1.5
Ca ²⁺	2.5	2.5
Cl ⁻	103.0	103.0
HCO ₃ ⁻	27.0	10.0
HPO ₄ ²⁻	1.0	1.0
SO ₄ ²⁻	0.5	0.5
pH	7.2-7.4	7.4

6.1.3 Result and discussion

6.1.3.1 *The structure of the nanofibrous layer*

In this work, the effect of laser pulse repetition on porosity and size of the fabricated nanofibers was investigated. Figure 6.1 shows SEM images of the nanofibrous

layer generated on Ti4 surface at pulse repetition of 4 MHz. A close up view of the layer shows that it consisted of self-assembled closed rings and bridges in which nanoparticles are fused together. The pores are interconnected with sizes of 900-1000 nm. Additional experiments were performed with different laser repetition rates at 8 and 12 MHz (Figure 6.2 and Figure 6.3). The pore sizes range approximately from 700-800 nm for the nanofibrous layer generated on Ti8, while they are about 650-750 nm for those synthesized on the surface of Ti12.

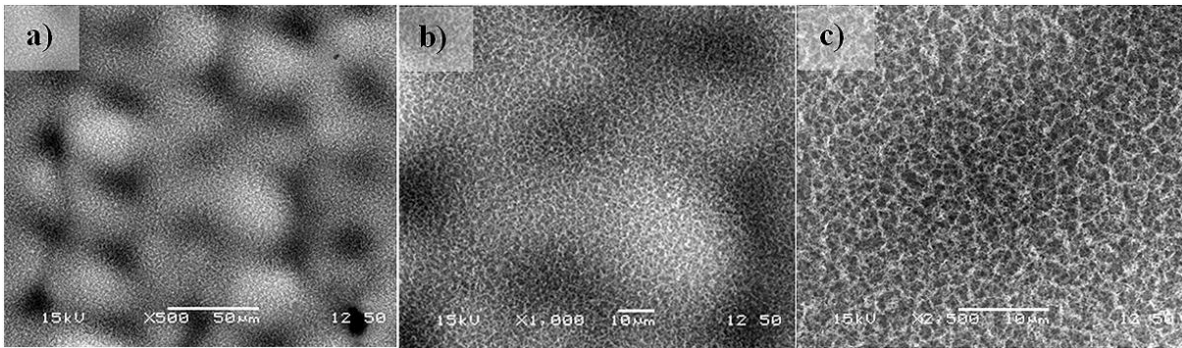


Figure 6.1 SEM images of titania nanofibrous structure synthesized on the Ti4 sample at laser repetition of 4 MHz at magnifications of a) X500, b) X1000, and c) X2500.

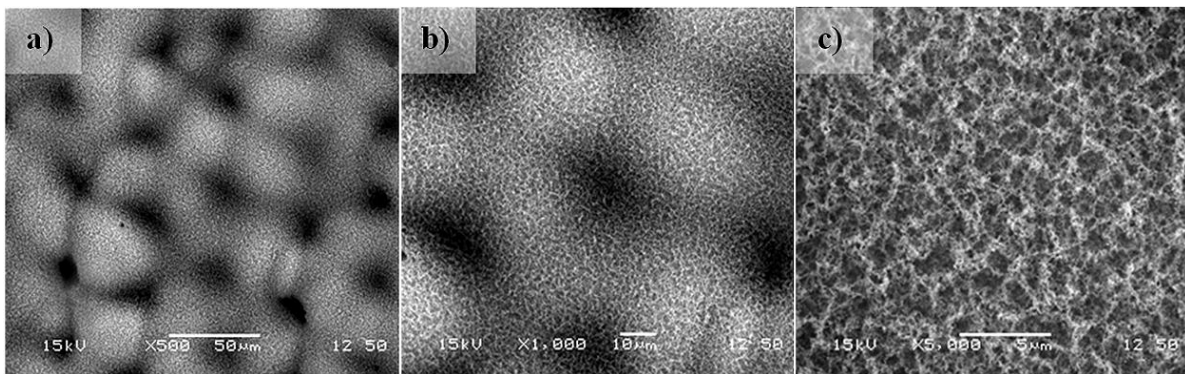


Figure 6.2 SEM images of titania nanofibrous structure synthesized on the Ti8 at laser repetition of 12 MHz at magnifications of a) X500, b) X1000, and c) X5000.

From TEM images of a single nanofiber, one can observe a high degree of nanoparticle aggregation (Figure 6.4). The nanoparticles are aggregated together in a semi-

solid state rather than loosely agglomerated. Therefore, the bond between the particles themselves and with the Ti substrate is assumed to be strong. The diameter of the nanofibers is approximately 16-20 nm for Ti12 and it increases as the repetition reduces to 4MHz. These results indicate that a reduction in laser pulse repetition leads to an increase in the density of the nanofibrous structures as well as in the size of nanoparticles. That is due to the fact that with the constant laser power and laser spot size, pulse energy drops off with an increase in pulse repetition rate which results in a reduction in material ablation and nanoparticle size.

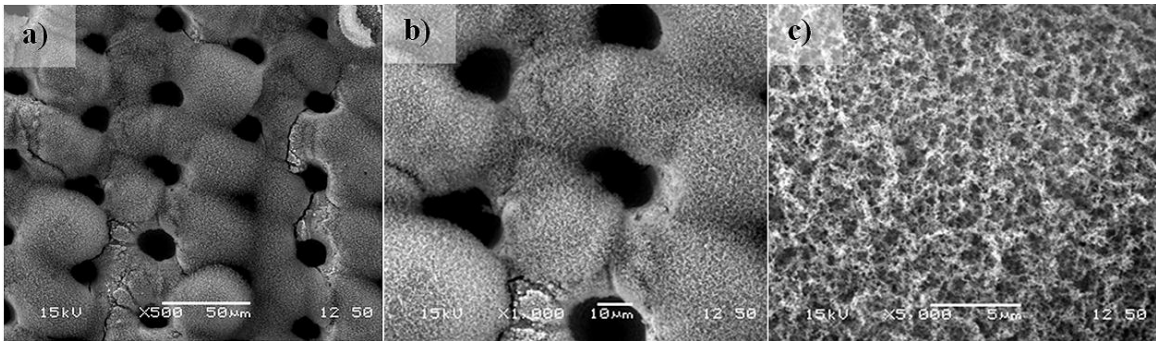


Figure 6.3 SEM images of titania nanofibrous structure synthesized on the Ti12 at laser repetition of 12 MHz at magnifications of a) X500, b) X1000, and c) X5000.

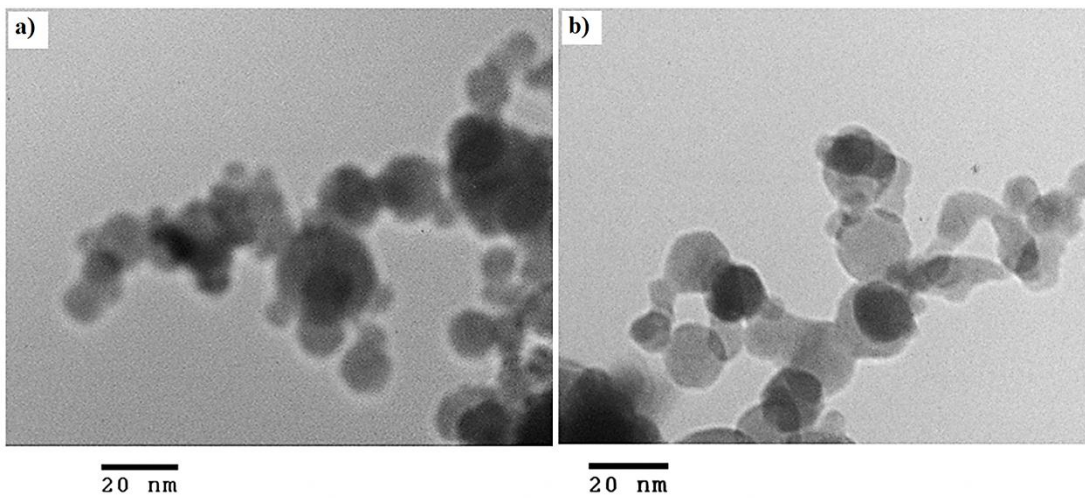


Figure 6.4 TEM images of Ti nanofibers synthesized at repetition of a) 12 MHz and b) 8 MHz.

In order to evaluate the crystal structure of nanofibrous layer XRD analysis was conducted. Figure 6.5 compares the XRD patterns of a Ti unprocessed sample and the nanofibrous layer generated on the Ti4 surface. The unprocessed Ti sample is entirely composed of alpha-phase titanium (α -Ti), while the pattern of nanofibrous structure indicate that it consists of tetragonal TiO_2 (rutile and anatase) and cubic TiO (hongquite). The sharp peaks in the patterns can be associated with the high crystallinity of the oxide phases. Titania exists in two main crystallographic forms, anatase (A) and rutile (R) [120]. The XRD peaks at 2θ : 25.28° (A101) and 2θ : 27.4° (R110) are often interpreted as the characteristic peaks of anatase and rutile crystal phases, respectively [120], [121]. The peaks at 2θ : 43.37° may be attributed to TiO . It has been reported that titanium oxide on the implant surface would greatly improve the apatite precipitation [153].

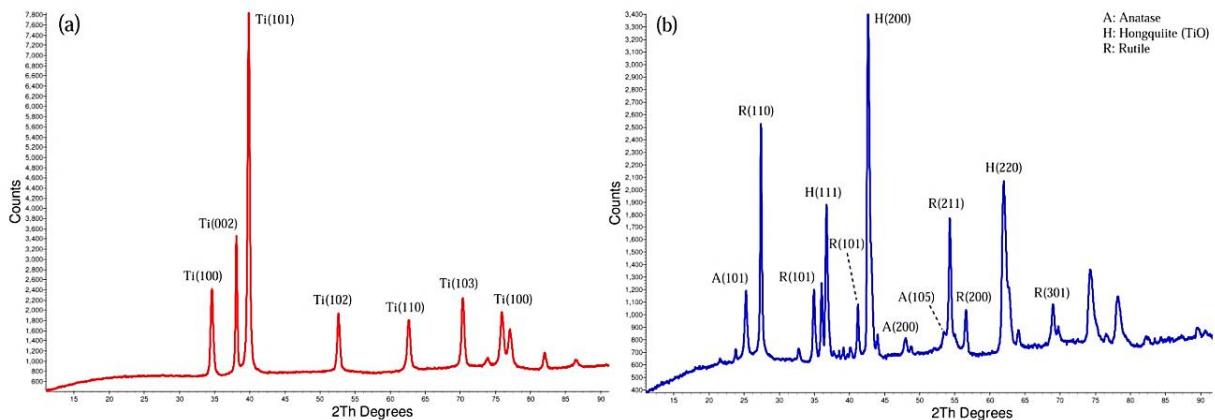


Figure 6.5 XRD patterns of a) an unprocessed Ti sample and b) the titania nanofibrous layer generated on the Ti4 sample after laser irradiation.

6.1.3.2 *The apatite-inducing ability of different surface morphologies*

SEM micrographs of the apatite-inducing ability of different surfaces are shown in Figure 6.6 through Figure 6.9. The unprocessed Ti sample did not induce any apatite

deposition after 3 days of soaking in SBF, whereas Ti4, Ti8, and Ti12 showed high apatite-inducing ability even after 1 day of immersion in SBF.

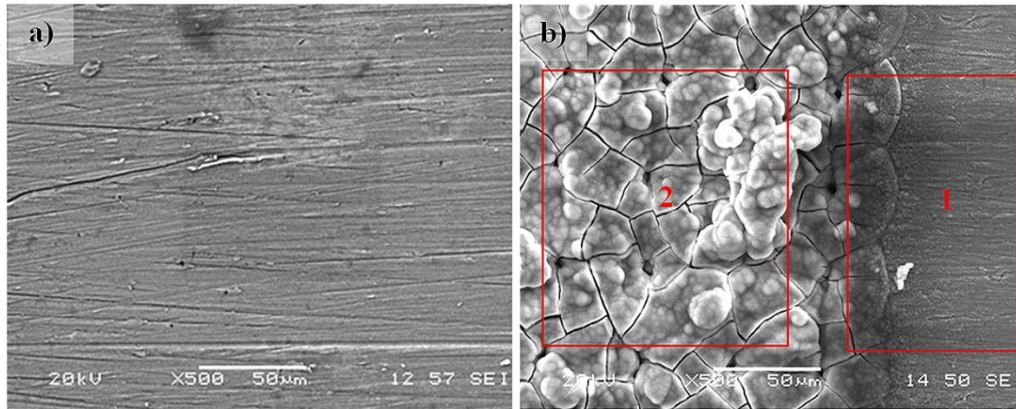


Figure 6.6 SEM images of surface morphology of an unprocessed Ti sample after a day soaking in SBF and b) SEM image of the Ti4 morphology which compares the different apatite-inducing abilities of (1) the unprocessed area, and (2) the nanofibrous layer after soaking for 3 days.

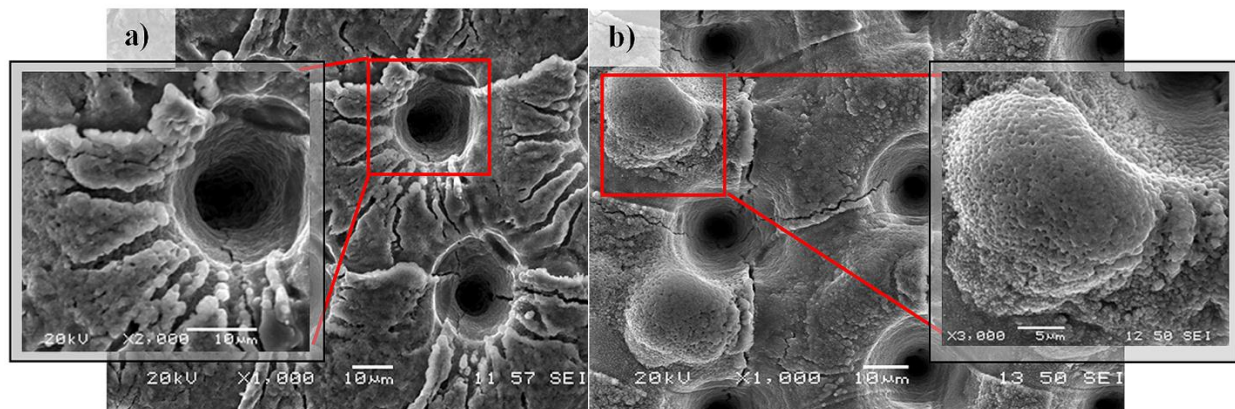


Figure 6.7 SEM images of the Ti12 surface morphology after soaking in SBF for a) 1day and b) 3days.

As illustrated in Figure 6.7a, for Ti12, although the apatite spheroids were too small to be detected, the whole nanofibrous surface was covered with apatite precipitation after 1 day of soaking. However, after 3 days of immersion, the precipitation layer became thick, and scattered apatite globules with a diameter of 22 μm were observed on the Ti12 surface. On the other hand, a thick precipitation layer made of apatite spheroids with a diameter of

2 μm deposited on the surfaces of the Ti4 and Ti8 samples even after 1 day of immersion in SBF (see Figure 6.8a and Figure 6.9). It can be observed that all the pores have been filled by apatite precipitation. However, the precipitation layer is not uniform for Ti8 in comparison with Ti4. After soaking for 3 days, all surfaces were covered by dense homogeneous apatite layers composed of numerous apatite spheroids with a diameter of 5 μm . Several apatite spheroids as large as 25 μm in diameter can be observed on both the Ti4 and the Ti8 surfaces after 3 days of immersion. The uniform apatite precipitation on the nanofibrous structure signifies that the reproducibility of apatite crystallization on the nanofibers is very high.

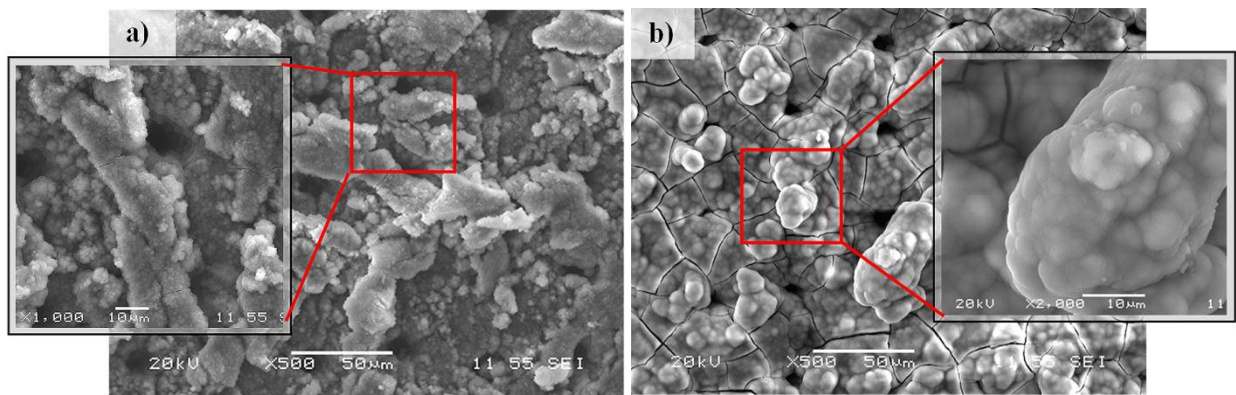


Figure 6.8 SEM images of the Ti8 surface morphology after soaking in SBF for a) 1day and b) 3days.

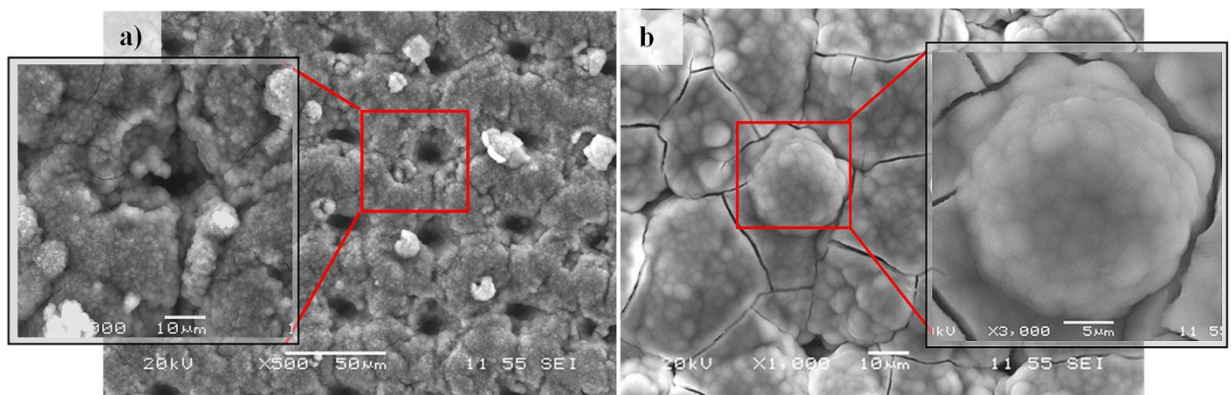


Figure 6.9 SEM images of Ti4 surface morphology after soaking in SBF for a) 1day and b) 3days.

The EDS analysis of the composition of the apatite layer deposited after 1 day of immersion in SBF for the Ti4 indicates the presence of titanium, calcium, phosphorous, and oxygen, as shown in Figure 6.10a. The molar Ca/P ratio was 1.31, which is attributed to that of octacalcium phosphate (OCP: $\text{Ca}_8\text{H}_2(\text{PO}_4)_6 \cdot 5\text{H}_2\text{O}$). OCP is considered to be necessary precursor in the crystallization of bone-like apatite [154], [155]. As depicted in Figure 6.10b, the EDS analysis of the Ti4 sample after immersion in SBF for 3 days shows rich phases of calcium and phosphorous with traces of magnesium. It is interesting that the titanium phase is barely detectable by EDS due to the fact that the deposited apatite layer is thick and compact. The molar Ca/P ratio for the precipitated apatite layer after 3 days of immersion in SBF was measured to be approximately 1.63, which corresponds to hydroxyapatite (HA: $\text{Ca}_5\text{H}_2(\text{PO}_4)_3 \cdot (\text{OH})$). Hydroxyapatite which has a composition similar to the mineral phase of bone is by far the most abundant inorganic phase in the human body [156]. It has been demonstrated that bone-like hydroxyapatite possesses good osteoconductibility and has a high affinity to living bone cells [155], [157].

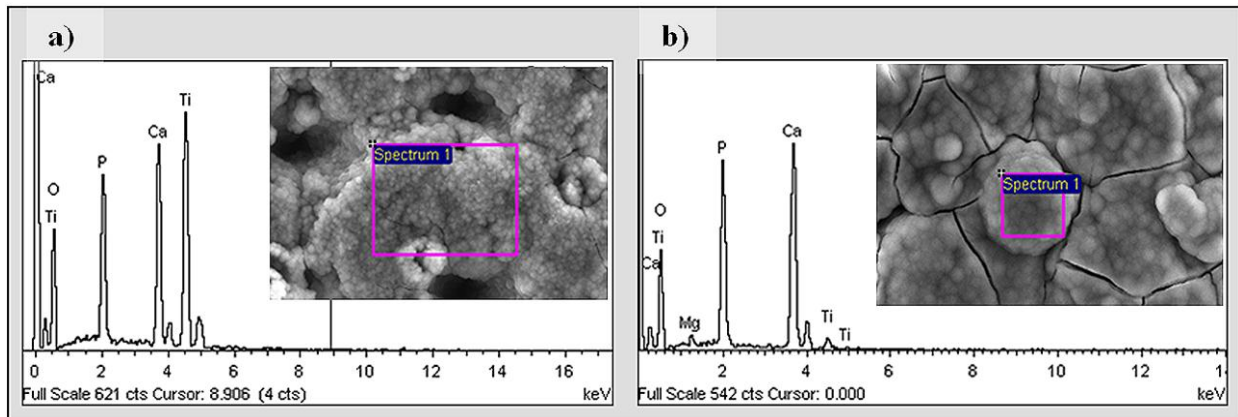


Figure 6.10 EDS analysis of Ti4 after soaking in SBF for a) 1day and b) 3days

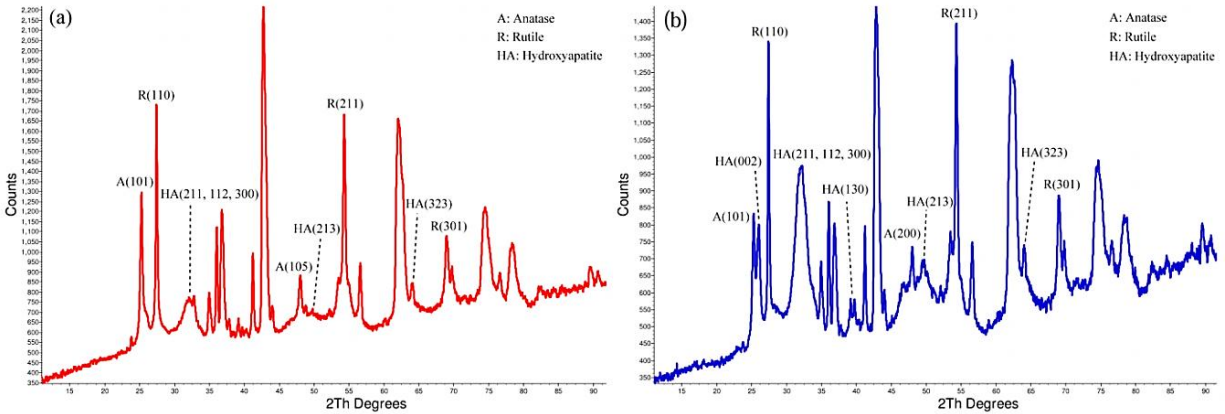


Figure 6.11 XRD analysis of Ti4 after soaking in SBF for a) 1day and b) 3days

Figure 6.11 contrasts XRD patterns of Ti4 after soaking in SBF for 1 day and 3 days. The broad peak at $2\theta: 32.6^\circ$ is attributed to the overlapping of (211), (112), (300), and (202) crystal planes, and the peak at $2\theta: 25.9^\circ$ is assigned to the (002) diffraction peak of HA. It can be seen that the apatite layer has been thick enough to be detected even after 1 day of immersion in SBF (Figure 6.11a). However, the peak at $2\theta: 25.9^\circ$ was not detected for the deposited layer after 1 day of soaking. The intensity of the peaks was increased for apatite layer precipitated after 3days as shown in (Figure 6.11b). It can be observed that the intensity of the peak attributed to HA diffraction plane at $2\theta: 32.6$ for the sample soaked for 3 days, has been dramatically increased and the peak became sharper which corresponds to larger crystal size.

In biological environments, the surface energy of the surfaces plays a crucial role in the mediation of solute adsorption and cell adhesion. The biological interactions between the biomaterial surface and a biological medium are closely associated with wettability [52], [62]. The wettability of unprocessed Ti substrates, Ti4, Ti8, and Ti12, has been studied by sessile drop contact angle measurement of a distilled water droplet. CA microscopic

images and CA measurements of an unprocessed Ti sample as well as the Ti4, Ti8, and Ti12 are depicted in Figure 6.12 and Figure 6.13, respectively.

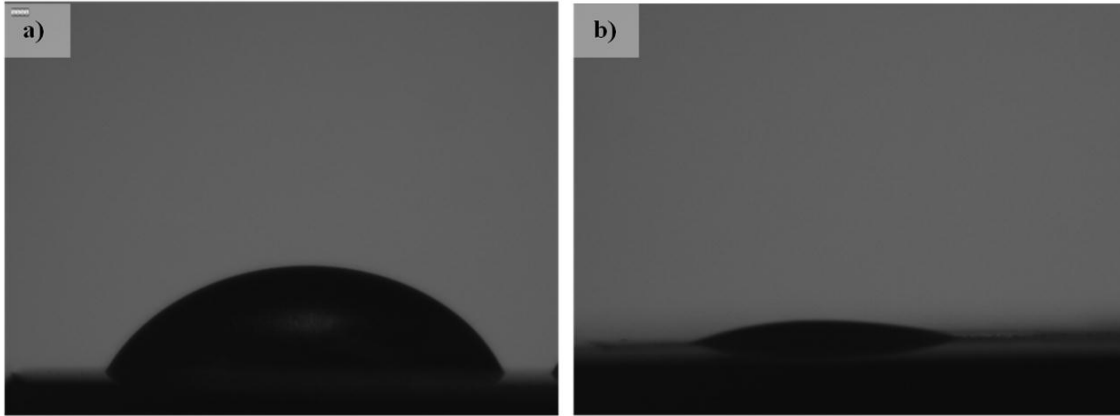


Figure 6.12 Microscopic images of a distilled water droplet on a) an unprocessed Ti and b) nanofibrous layer on the Ti8.

Contact angles $<4^\circ$, on titania nanofibrous layer on the Ti4 implies its superhydrophilic properties in contrast to those of unprocessed Ti surface (66.7 ± 1). The almost complete spreading of water droplets on the surface covered with the nanofibrous layer is observed during the CA measurement for all the samples.

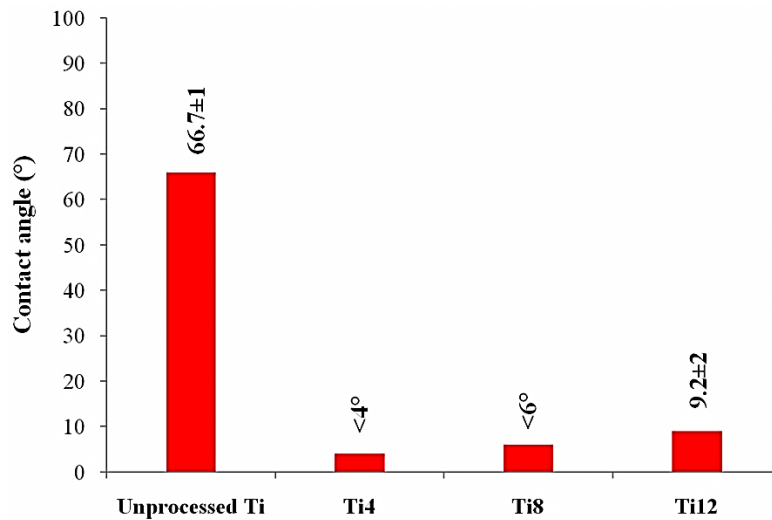


Figure 6.13 Sessile drop water contact angle measurement for an unprocessed Ti substrate, and the titania nanofibrous layer on the Ti4, Ti8, and Ti12.

The abovementioned results of this study showed that generated titania nanofibrous layer on the Ti surface using laser irradiation greatly enhanced the wettability of the surface that consequently increased the apatite-inducing ability of it. Furthermore, the results indicated that the density and porosity of the nanofibrous layer affected the apatite-inducing ability of the surface. Due to high temperatures and atmospheric oxygen, nanofibers become oxidized and covered by a few nanometer-thick titanium oxide layers. The XRD results showed that the oxide layer consisted of TiO_2 (rutile and anatase) and cubic TiO (hongquite). Several studies have demonstrated that both rutile and anatase enhance the apatite-inducing ability which consequently improves bioactivity and osteointegration of Ti surfaces [158–160].

The results of this study indicated that apatite nucleation and deposition happened even after a day. The results also demonstrated that the surface with a higher amount of nanofibrous structures resulted in more apatite deposition. The mechanism for rapid apatite deposition on the nanofibrous layers can be attributed to the 3-D structure of the layers as well as their surface chemistry. Nanofibrous structures with high specific surface areas enhance the wettability of the surface when soaking in SBF. The wettability improves the reaction of water molecules present in the SBF with the titanium oxides on the nanofiber surface leading to surface hydroxylation. The hydroxylated titanium oxide is supposed to be insoluble and results in the formation of Ti-OH group on the surface, which is believed to promote apatite nucleation [161–163]. Ti-OH layer reaction with aqueous solution changes the surface charge. At a lower pH (<4), the formation of $[\text{Ti-OH}]^+$ from basic Ti-OH results in positive surface charge, while at higher pH (>9) acidic Ti-OH gives

off a proton and yields $[\text{Ti} - \text{OH}]^-$ leading to negative surface energy. At pH levels between 4 and 9, both basic and acidic hydroxides coexist on the surface [164]. Since the isoelectric point (IEP) of titanium oxide is 5-6, at neutral pH, in our case SBF (7.4), the surface is slightly negative due to the deprotonation of acidic hydroxides. A negatively charged surface attracts Ca^{2+} cations and forms calcium hydroxide. Subsequently, phosphate ions (PO_4^{3-}) present in the SBF react with the calcium hydroxide layer that consequently results in apatite nuclei formation [165]. Since SBF is a supersaturated solution of Ca and P ions, bone-like apatite spheroids grow spontaneously on apatite nuclei sites. The Bone-like apatite layer acts as a temple for cell migration, integration, and differentiation at the biomaterial-tissue interface, which in turn improves bioactivity and osseointegration of Ti surfaces. In the current work, nanofibrous structures, owing to their highly effective surface area, promoted enormous nuclei sites which led to a decrease in the deposition time as well as an increase in the amount of apatite deposition. Conversely, the low surface energy and rare amount of hydroxide on the surface of the unprocessed Ti substrate impeded its apatite-inducing ability. Hence, no apatite deposition was seen on the unprocessed Ti, even after 3 days. A nanofibrous layer with a rapid apatite-inducing capability is expected to advance bone formation when implanted in a living body.

6.2 The Influence of Titania Nanofibrous Platforms on Cell

Behavior

The current challenge in bone tissue engineering is to design a platform that can provide appropriate pore surface to encourage desired cellular activities and to guide 3-D tissue regeneration. The main strategy of tissue regeneration research is the synthesis of specific platforms on which relevant cells, attach, grow and proliferate. Particularly for bone tissue engineering, biomaterials should combine the properties of both biocompatibility and bioactivity. The achievement of stable direct contact between bone and implant surface is a critical requirement for the development of optimal platform. The two most important key factors when designing such architectures are surface wettability and surface topography [166]. Previous studies have reported that surface characteristics of scaffolds have a direct control on tissue response by affecting protein adsorption as well as tuning cell proliferation and differentiation [5], [167], [168]. It is believed that cells are very sensitive to the surface nanotopography and distinguish surface topographical changes, which consequently can induce alterations in the cytoskeleton, cell shape and differentiation [169–171]. In addition to the cellular effect, surface nanotopography can serve as a platform to regulate the initiation and growth of hydroxyapatite crystals, the key building block of bone tissue [172]. Compared with traditional *in vitro* cell culture materials, three-dimensional nanofibrous scaffolds provide a superior environment for promoting cell functions by mimicking the natural regeneration micro-/nano-environments and the architecture of the ECM.

The current study investigates the influence of synthesized Ti platforms on the *in vitro* proliferation and viability of osteoblast-like MC3T3-E1 cells and NIH 3T3 mouse embryonic fibroblasts. Ti surfaces with different morphology are synthesized by altering laser fluence. The results point out that the density of engineered nanofibrous architecture can be tuned by laser fluence. The crystallinity, surface adhesion, and surface energy of the nanofibrous structures are discussed. The results from *in vitro* studies reveal that the titania nanofibrous architecture possesses excellent biocompatibility and significantly enhances proliferation of both cell lines compared to the untreated titanium specimen. The cell numbers on the substrates change consistently with the density of nanofibrous structures. This approach of nanoengineering 3-D architectures suggests considerable perspective for promoting Ti interfacial properties to develop new functional biomaterials.

6.2.1 Experimental details

6.2.1.1 *Sample preparation*

The freestanding nanofibrous structures have been synthesized on Ti specimens using single point femtosecond laser irradiation under ambient condition. Specimens in size of 10×10×0.5 mm were cut from grade 2 (ASTM B265) pure Ti sheet using a diamond saw with oil lubrication. The samples were then ground finished to 1200-grit silicate-carbon papers to eliminate macro-level surface defects and contaminations.

6.2.1.2 *Laser processing and synthesis of nanofibrous structures*

Specimens were irradiated by laser beam at laser repetition of 8 MHz and different laser dwell time of 2ms and 10ms to synthesize nanofibrous structures with different

abundance. The specimens irradiated at 2ms and 10ms are indicated as Ti2 and Ti10, respectively, through this study. The specimens had a lased surface area of 64 mm².

6.2.1.3 *Surface characterization*

6.2.1.3.1 SEM analysis of cells on structures

The morphology of nanofibrous structures was characterized using a SEM. The cell-nanofiber structures were first rinsed in Dulbecco's Phosphate-Buffered Saline (DPBS) and fixed in 2.5% glutaraldehyde. Afterwards, samples were dehydrated in a series of increasing concentrations of ethanol from 70% to 100%. The samples were then sputter-coated with gold using a sputter coater and observed under a scanning electron microscope (Hitachi) at 5 kV. The elemental contents on the surface of the structures were examined by EDS analyses (Hitachi XEDS system).

6.2.1.4 *Cell culture and assays*

All products were purchased from Sigma-Aldrich unless otherwise mentioned. NIH3T3 mouse embryonic fibroblasts and osteoblast-like MC3T3-E1 cells purchased from ATCC, USA, were used in this study. Cryopreserved cell suspensions were stored in a -150°C freezer until use. Prior to cell culture they were thawed in a water bath at 37°C. NIH3T3 cells were suspended in Dulbecco's Modified Eagle Medium (DMEM) supplemented with antibiotic and fetal bovine serum. The cell suspensions were added to 75 cm² culture flasks and incubated at 37 °C under a 5% CO₂ atmosphere. The cell suspensions were subcultured when they reached 70–90% confluence. The cells were transferred to tubes and centrifuged at 930 rpm for 8 mins, forming a cell pellet that was resuspended in the

appropriate culture medium. Concentrations of 5×10^6 cells were suspended in 13 ml of the appropriate culture medium. The cell suspensions were added to 75 cm^2 culture flasks and incubated at $37 \text{ }^\circ\text{C}$ under a 5% CO_2 atmosphere. The first medium change took place between 24 and 36 hours after initial culture; subsequent medium changes occurred every other day. The cells were seeded on an as-received grade 2 titanium foils (control) and titania synthesized nanofibrous structures, two different structure density (all substrates 1 cm^2), in a 24-well plate. Prior to the seeding, all substrates were sterilized and conditioned. The substrates were subjected to 2 hours UV exposure. The cells were seeded at an initial density of 5×10^6 cells. The substrates were incubated at $37 \text{ }^\circ\text{C}$ under a 5% CO_2 atmosphere and examined for proliferation and cytotoxicity assays after 48h culture.

In vitro proliferation of the cells was performed using 3-(4,5-Dimethylthiazol-2-Yl)-2,5-Diphenyltetrazolium Bromide (MTT) assay. MTT is a water soluble yellow tetrazolium salt which can be absorbed by metabolically active cells and converted into formazan dyes, giving a purple color. Prior to the measuring MTT activity, cell media was added to 2.54mg/ml of MTT in dulbecco's phosphate buffered saline (DPBS), and incubated for 4 hours. After incubation, the clear liquid was aspirated and dimethyl sulfoxide (DMSO) was added to dissolve formazan crystals. Absorbance was measured at 540 nm. Colorimetric analysis and comparison to a standard curve of known viable cell number can be employed to determine viable cell number for each condition.

6.2.1.5 *Statistical analysis*

Data were presented using the means \pm standard deviations ($n = 3$). Statistical analysis was performed using Student's t-test for differences among groups. A value of $p < 0.05$ was considered to be statistically significant.

6.2.2 **Results and discussion**

6.2.2.1 *Characteristics of the synthesized surfaces*

The structure of the nanofibrous layer is influenced by various laser parameters such as laser fluence, laser pulse repetition, and laser pulse dwell time. In our previous study, the effect of laser pulse repetition on porosity and size of the synthesized nanofibers was investigated [35]. In this study, the nanostructures were synthesized at different laser dwell time. Figure 6.14 depicts SEM images of the nanofibrous structures synthesized on Ti2 and Ti10 platforms at laser dwell time of 2ms and 10ms, respectively. The nanofiber density has increased significantly as the laser dwell time increased to 10ms in compared with 2ms.

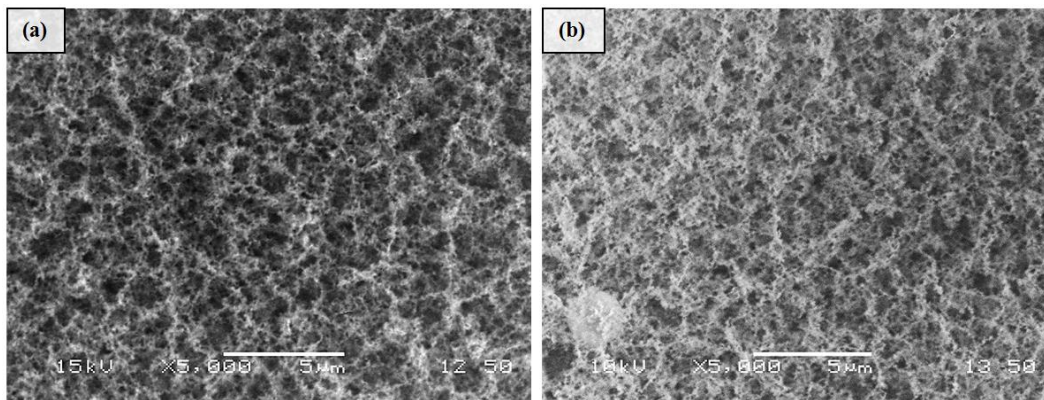


Figure 6.14 SEM images of titania nanofibrous structure of a) Ti2 sample at laser repetition of 8 MHz and dwell time of 2ms and b) Ti10 sample at laser repetition of 8 MHz and dwell time of 10ms.

As the laser dwell time increases, the focal spot of the laser beam stays on the same spot on the substrate for many consecutive pulses which results in an increase in the total laser energy flux transferred to the spot. As Eq. 4.9 predicts, the higher transferred laser energy flux, for the optimum evaporation regime, results in an increase in the number of evaporated particles. As Eq. 4.9 suggests, with increase of laser dwell time the number of evaporated particles in the laser plume intensifies which for the titanium target at wavelength of 1030 nm, one can obtain a good agreement with the experimental results.

The crystal structure of nanofibrous structures was evaluated using XRD. The XRD patterns of the control sample and the nanofibrous structures confirmed that the control sample was entirely composed of alpha-phase titanium (α -Ti), whereas the nanofibrous structure was consisted of tetragonal TiO_2 (rutile and anatase) and cubic TiO (hongquiiite).

In biological environments, the surface energy of the surfaces plays a key role in the mediation of protein adsorption and cell adhesion. The biological interactions between the biomaterial surface and a biological medium are closely associated with wettability [10], [62]. The wettability of control, Ti2, and Ti10 samples has been studied by sessile drop contact angle measurement of a distilled water droplet. CA measurements of the control sample as well as the Ti2 and Ti10 are depicted in Figure 6.15. Contact angles $<3^\circ$, on titania nanofibrous structure on the Ti10 indicates its superhydrophilic properties in contrast to those of control Ti surface (68 ± 1). The complete spreading of water droplets on the surface with the nanofibrous structure is observed during the CA measurement for both samples. This indicates a similar tendency as previously reported our previous study [35] in which

titanium substrates were laser treated in a similar way as in the present study but different laser parameters.

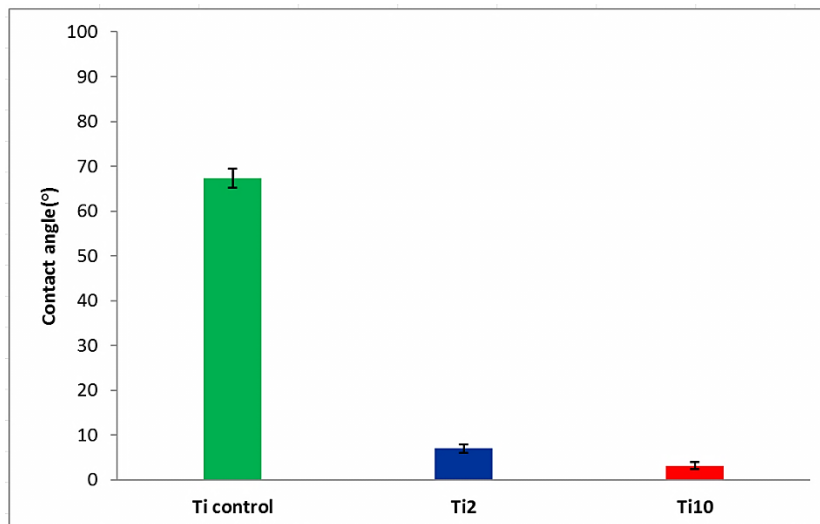


Figure 6.15 Sessile drop water contact angle measurement for the control sample, and the titania nanofibrous structures on the Ti2 and Ti10.

The electric charge of a material surface is considered to be one of the main physical factors involved in the biological evolution of the tissue around a scaffold. A biomaterial's ZP shows its electric surface properties. Higher ZP values indicate repulsive forces and stability at the surface. Zeta potential measurements were implemented to identify the difference in electro-kinetic interactions at the interface between aqueous electrolyte and material surfaces. Figure 6.16 illustrates the zeta potential values for Ti2, Ti10, and control samples. All samples showed the negative values for zeta potential.

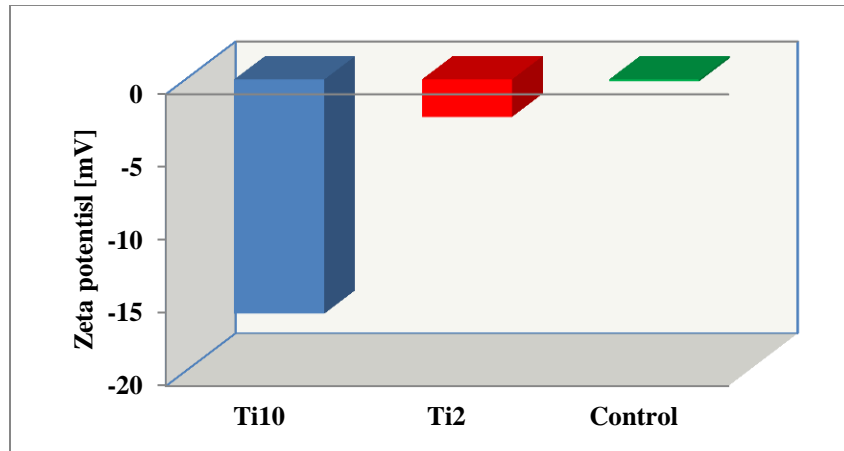


Figure 6.16 Zeta potential values for the control sample and the titania nanofibrous structures on the Ti2 and Ti10.

Force versus distance curves were acquired in order to reveal the interaction between the surface of the sample and the tip of the AFM. These curves permit the determination of the adhesion force between the tip and the sample surface. It is equal to the necessary force to elastically deform the cantilever during the jump off contact. Figure 6.17 represents force curves obtained for the surfaces of Ti2, Ti10, and control samples.

The areas under the force-height curves (adhesion energy) were measured to be 115, 69, and 18 for Ti10, Ti2, and control samples, respectively (Figure 6.18).

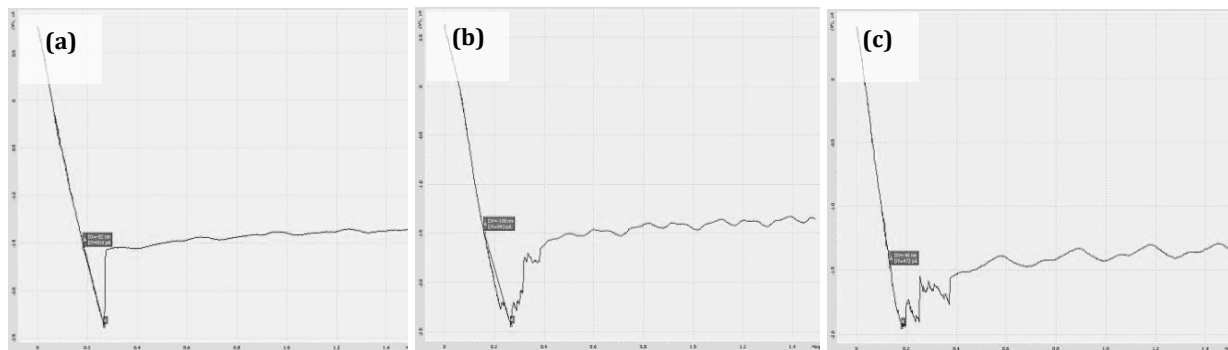


Figure 6.17 Force-distance curves taken at for the (a) control sample and the titania nanofibrous structures on the (b) Ti2 and (c) Ti10.

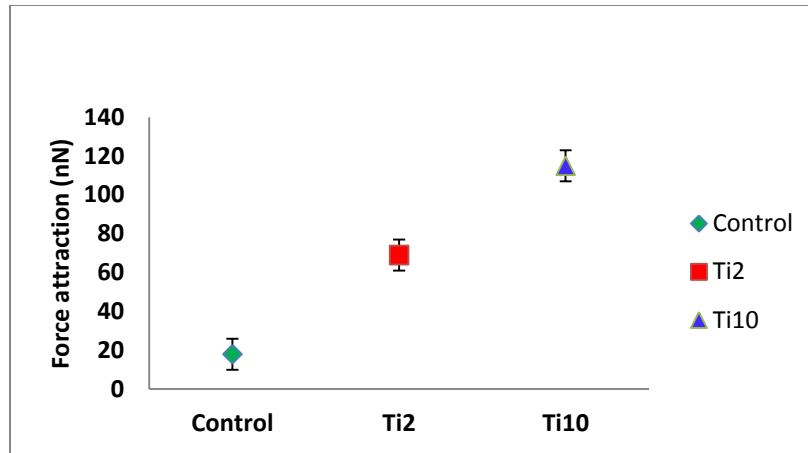


Figure 6.18 Adhesion energy calculated from the area under the force-height curves for the control sample and the titania nanofibrous structures on the Ti2 and Ti10.

The chemical bonds, such as hydrogen bonds, formed between metal oxide surfaces and outer cell membrane significantly is contributed to the adhesion. The number of hydrogen bonds that can form during the adhesion is clearly related to the contact area between the two surfaces as well as their composition and reactive site densities. The adhesion energy can be measured from the area under force-height curve. Therefore, higher the area under the force-height curve is the higher the adhesion energy will be which leads to greater number of hydrogen bonds. The results from Figure 6.9 suggests that as the density of nanofibrous structures on the surface increase the adhesion energy of the surfaces escalates which results in greater number of hydrogen bonds. The adhesion between surfaces is directly linked to the real area of contact. Since the nanofibrous structures have a much higher contact area than microstructures, as the density of nanostructures on a surface increase the adhesion energy goes up.

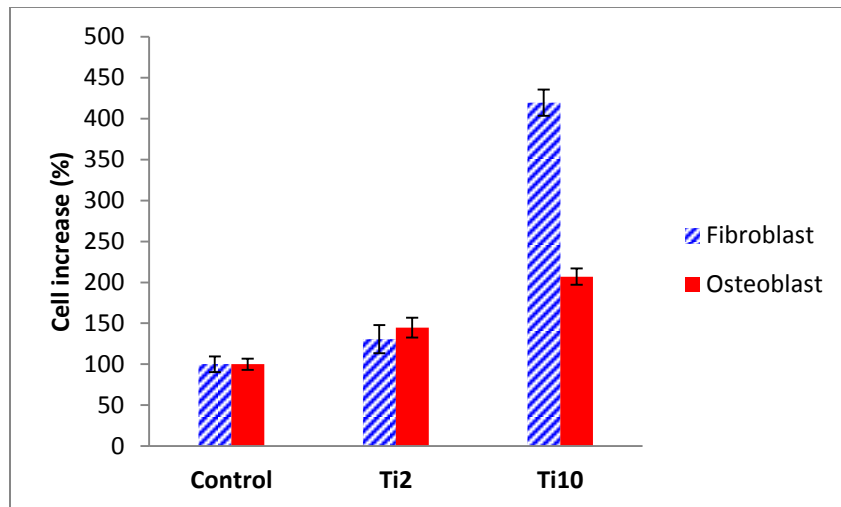


Figure 6.19 MTT assay of MC3T3-E1 cells (solid red) and NIH3T3 cells (stripe blue) seeded and incubated for 48 hrs on Ti2, Ti10, and control samples.

Figure 6.19 illustrates the results from MTT assay of MC3T3-E1 cells and NIH3T3 cells seeded and incubated for 48 hrs on Ti2, Ti10, and control substrates. The fibroblast cell number adhering to Ti substrates with nanostructures was significantly higher than that to the untreated counterpart, and increased with increasing the density of nanofibrous structures. The MC3T3-E1 cell population on the Ti10 substrate was considerably higher than that on the control sample, and increased with increasing the density of nanofibrous structures. The cell increase of more than 500% on the sample with high density nanofibrous structure was observed in compared with the control sample.

The effects of the Ti nanofibrous structures on the cell adhesion behaviour can be explained in terms of specific surface area of the nanofibrous structures, because the specific surface area increases with nanofibrous features at a direct proportion. Recent *in vivo* and *in vitro* studies have demonstrated that surfaces comprised of platforms with nano-features exhibit additional biological effects by producing integration between oxide and apatite nanocrystals and also by improving the cell-material interaction [10], [53],

[54]. Other than topographical properties, laser ablation of the Ti surface resulted in formation of titanium oxides (rutile and anatase phases) that enhanced the apatite deposition and adhesion rate on Ti substrate [158–160].

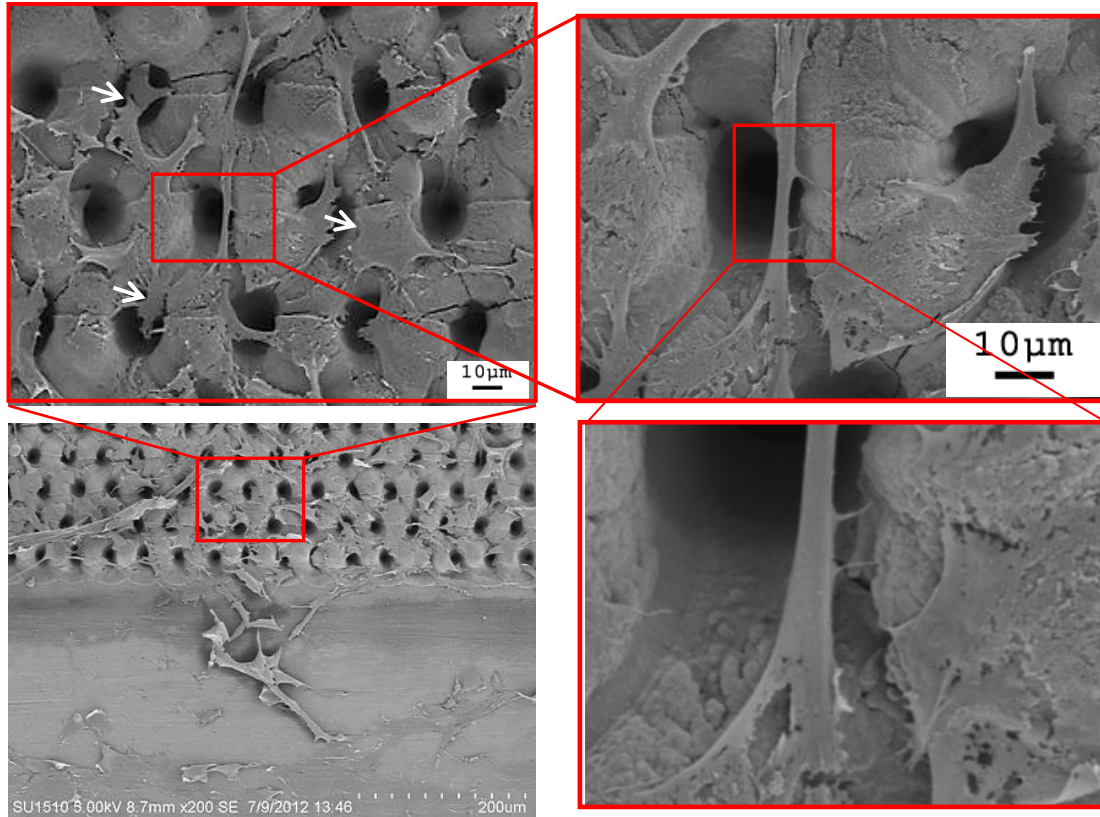


Figure 6.20 Representative SEM images of MC3T3-E1 cells after 1 day on the control substrate and titania nanofibrous structure. Images show a higher degree of MC3T3-E1 activation and matrix formation on titania nanofibrous structure. The close-up image on the right indicates MC3T3-E1 cell extension on the surface of titania nanofibrous structure. Arrows show cells spreading on the nanofibrous structures. Note that the substrates were coated with a 10 nm layer of gold and imaged at 5 keV. Experiments were replicated on at least three different samples.

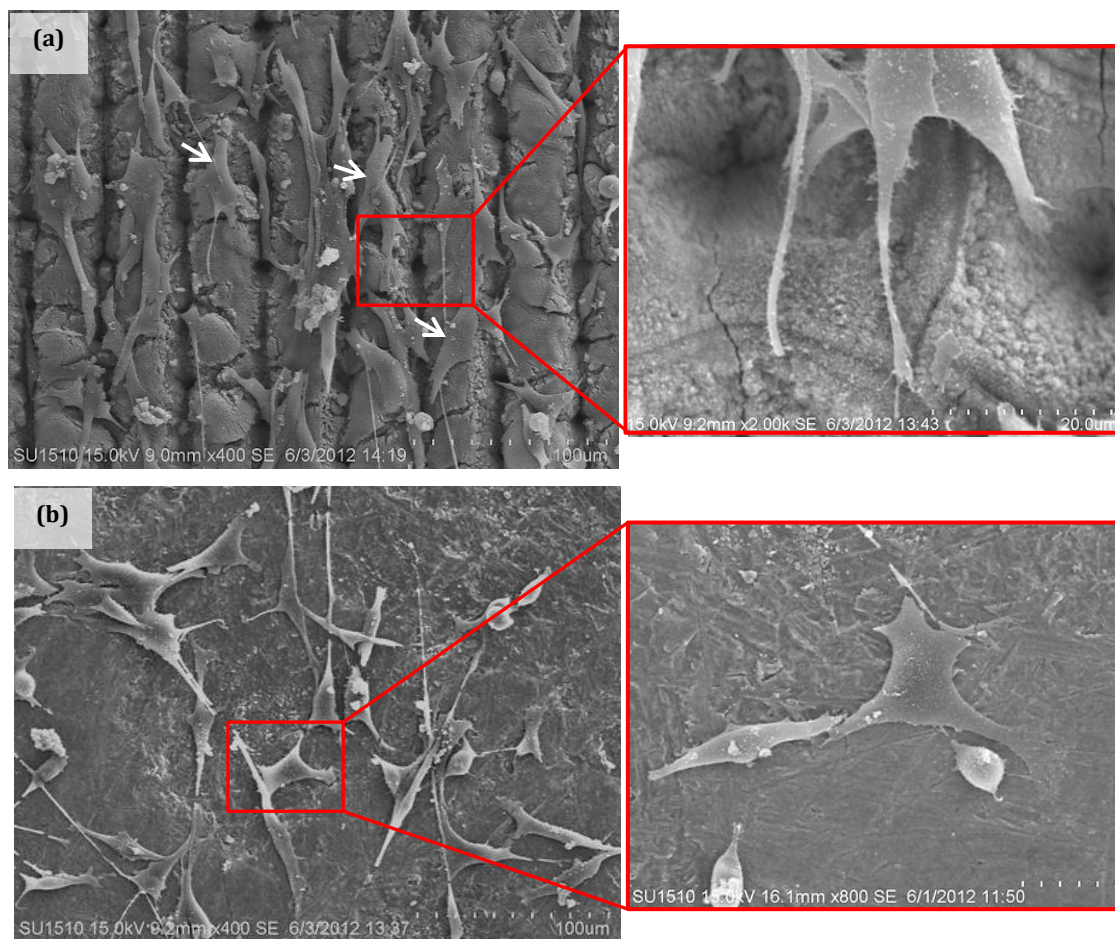


Figure 6.21 Representative SEM images of NIH3T3 cells after 1 day on (a) the titania nanofibrous structure and (b) the control substrate. Images show a higher degree of cell activation and matrix formation on titania nanofibrous structure. Arrows show cells spreading on the nanofibrous structures. Note that the substrates were coated with a 10 nm layer of gold and imaged at 15 keV. Experiments were replicated on at least three different samples.

The components present in the ECM are often derived from cell interactions with their environment, potentially resulting in cellular aggregation and activation, which can be visualized using SEM imaging. NIH3T3 and MC3T3-E1 cell morphology and interaction with the nanofibrous architecture was investigated after 1 and 2 days culture (Figure 6.20 and Figure 6.21). These results appear to support the presence of extracellular components, as indicated by the matrix-like formation deposited across all of the substrates in varying amounts. The greatest degree of extracellular, matrix-like

components is evident in the images of MC3T3-E1 cells after 3 days culture on nanofibrous structure, as shown in Figure 6.20.

The results presented here indicate that the nanofibrous architecture provides a favorable template for the growth and maintenance of both MC3T3-E1 and NIH3T3 cells.

6.2.3 Discussion

The interaction of cells with any material is a very complex process which is determined not only by the topography alone, but also by the surface chemistry.

In our previous study, it was shown that synthesized nanofibrous structures dramatically enhance the bioactivity of the titanium surfaces. Furthermore, the results indicate that the density and porosity of the nanofibrous layer affect the apatite-inducing ability of the surface. Nanofibrous structures with high specific surface areas enhance the wettability of the surface when soaking in SBF. The wettability improves the reaction of water molecules present in the SBF with the titanium oxides on the nanofiber surface leading to surface hydroxylation. The hydroxylated titanium oxide is supposed to be insoluble and results in the formation of Ti-OH group on the surface, which is believed to promote apatite nucleation [161-163]. Ti-OH layer reaction with aqueous solution changes the surface charge. At a lower pH (<4), the formation of $[\text{Ti} - \text{OH}]^+$ from basic Ti-OH results in positive surface charge, while at higher pH (>9) acidic Ti-OH gives off a proton and yields $[\text{Ti} - \text{OH}]^-$ leading to negative surface energy. At pH levels between 4 and 9, both basic and acidic hydroxides coexist on the surface [164]. Since the isoelectric point (IEP) of titanium oxide is 5-6, at neutral pH, in this case, SBF (7.4), the surface is

slightly negative due to the deprotonation of acidic hydroxides. A negatively charged surface attracts Ca^{2+} cations and forms calcium hydroxide. Subsequently, phosphate ions (PO_4^{3-}) present in the SBF react with the calcium hydroxide layer that consequently results in apatite nuclei formation [165]. Since SBF is a supersaturated solution of Ca and P ions, bone-like apatite spheroids grow spontaneously on apatite nuclei sites (Figure 6.22). The Bone-like apatite layer acts as a platform for cell migration, integration, and differentiation at the biomaterial-tissue interface, which in turn improves bioactivity and osseointegration of Ti surfaces.

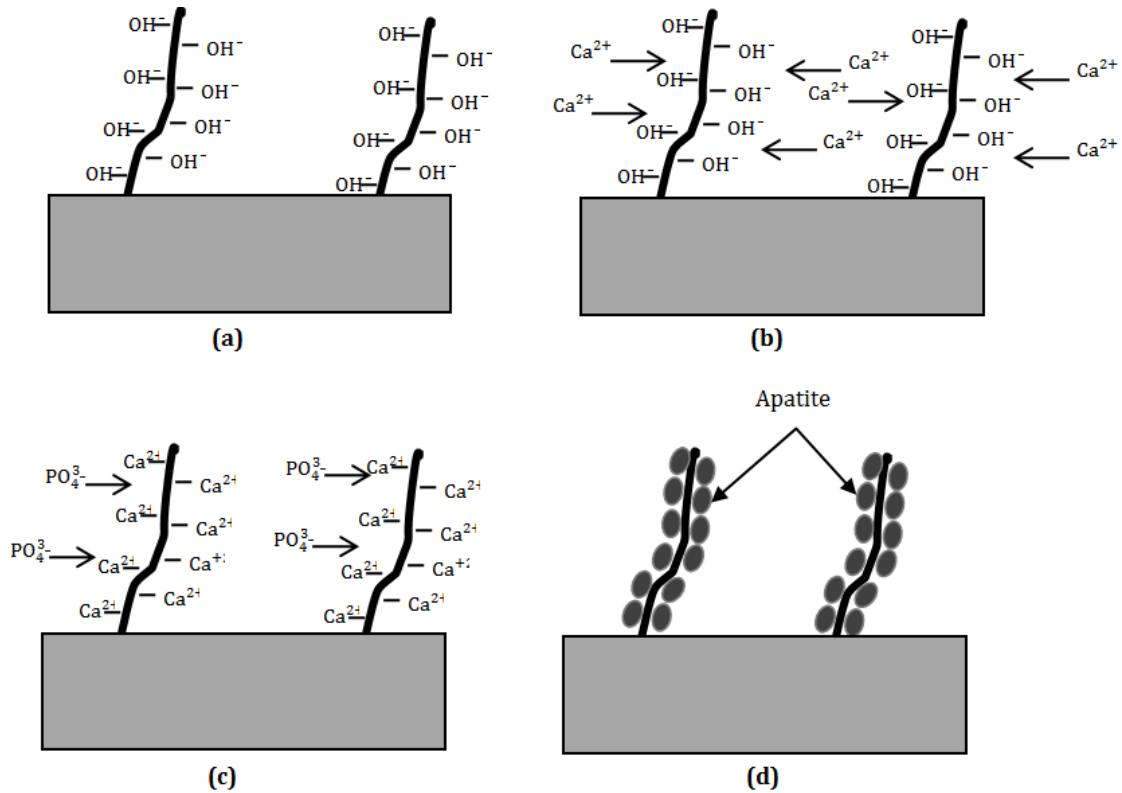


Figure 6.22 Schematic illustrations demonstrating the mechanism of apatite formation on nanofibers surface. a) The nanofibers surface is slightly negative due to the deprotonation of acidic hydroxides. b) A negatively charged surface attracts Ca^{2+} cations and forms calcium hydroxide. c) Phosphate ions (PO_4^{3-}) present in the SBF react with the calcium hydroxide layer that results in apatite nuclei formation. d) Since SBF is a supersaturated solution of Ca and P ions, bone-like apatite spheroids grow spontaneously on apatite nuclei sites.

The present study evaluated the cell compatibility of such 3-D freestanding nanofibrous structures using osteoblast-like MC3T3-E1 cells and NIH 3T3 mouse embryonic fibroblasts (ATCC) as a cell model. The fibroblast cell number adhering to the laser Ti substrate with nanostructures was significantly higher than that to the untreated counterpart after 48 h, and increased with increasing the density of nanofibrous structures. Woo et al. [173] claimed that scaffolds with nano-fibrous pore walls are able to adsorb fourfold more protein than scaffolds with solid pore walls. The adsorbed proteins are then thought to mediate the cells' interactions with the scaffolds (Figure 6.23). It's been also reported that greater amounts of proteins were presented on the nano-scale TiO_2 network than on a polished Ti surface [174] Therefore, the surface chemistry of titania nanofibrous structure appeared to enhance the adhesion of nanoscale proteins such as those found in cell culture media or animal body fluids. This also partially explained the superior in vitro and in vivo growth of fibroblasts on the titania nanofibrous layer compared to the control specimen.

In regards to topography, the surface energy of the nanofibrous structures was higher than that of the control sample in the present study. The surface with high surface energy enhanced the in vitro proliferation of the osteoblast-like cells significantly as the cell numbers on the nanofibrous structures were remarkably larger than that on the control sample. It has been reported that in vitro cell responses to the culture surfaces are usually mediated by proteins absorbed from serum-supplemented culture media [44]. In the present study, 10% fetal bovine serum was contained in the culture media. The globular protein, bovine serum albumin (BSA), is a major component of fetal bovine serum.

It's been shown that the BSA adsorption was directly related to the surface energy, with an excellent linear correlation with the polar component of the surfaces: the higher the polar component, the higher the albumin adsorption [175], [176]. Since proteins mediate adhesion of anchorage-dependent cells, and thus influence subsequent cellular functions (such as cell proliferation, deposition of calcium-containing mineral deposits, etc.), the mechanism(s) of protein interactions with titania nanostructures need to be further investigated and elucidated.

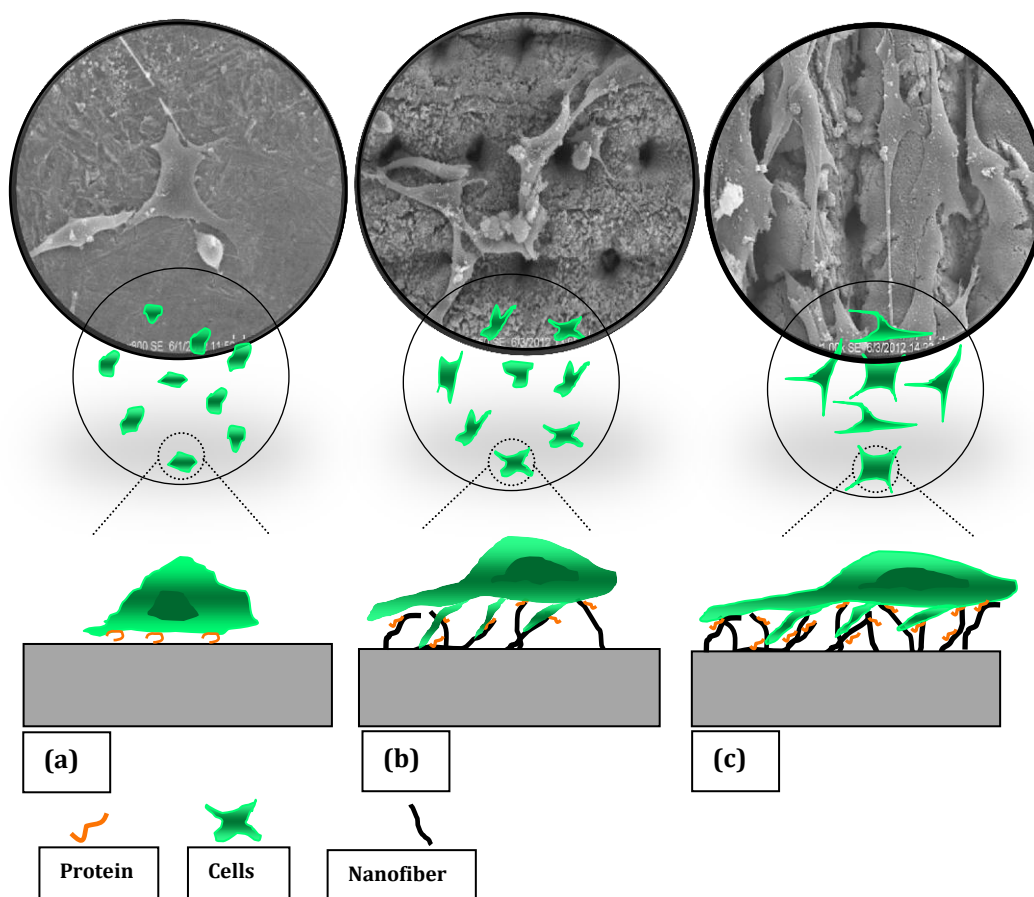


Figure 6.23 Comparison of the cell interaction and adhesion to the surface of a) control sample, b) surface with lower nanofiber density, and c) surface with higher nanofiber density. Upon immersion in culture media, proteins are adsorbed to the titania nanofibrous structures. By increasing the density of nanofibers and consequently increasing the surface area, more protein would be adsorbed to the nanostructures. These proteins would then act as potential adhesion sites for the cells.

6.3 Summary

In this study, the synthesis of titania nanofibrous structures on Ti substrates using a high repetition femtosecond laser was introduced. It was shown that a thick, homogenous hydroxyapatite layer was deposited on the Ti surface with titania nanofibrous layers after 3 days of immersion in SBF. The results indicated that the surface morphology as well as surface physiochemical properties (surface reactivity and wettability) of the nanofibrous layers significantly influenced their apatite-inducing capability. It was demonstrated that laser ablation of the Ti surface resulted in formation of rutile and anatase phases that enhanced the apatite deposition and adhesion rate on Ti substrate. A surface with a denser nanofiber layer showed a higher apatite-inducing ability. Also, the effect of synthesized titania architectures on the *in vitro* proliferation and viability of osteoblast-like MC3T3-E1 and NIH 3T3 mouse embryonic fibroblasts was assessed. The results from *In vitro* studies revealed that the titania nanofibrous architecture possesses an excellent biocompatibility and significantly enhances proliferation of the osteoblast cells compared to the untreated titanium specimen. The cell numbers on the substrates changed consistently with the density of nanofibrous structures. It is expected that synthesized 3-D titania nanofibrous layers will improve the properties of titanium and advance the development of new biomedical devices for diverse biomedical applications such as tissue scaffolds, orthopedic and dental implants, to control clotting, and to provide a platform to prevent bacterial adhesion.

CHAPTER 7

SUMMARY AND FUTURE RESEARCH

7.1 Summary

In this dissertation, a diverse range of scientific and engineering concepts was investigated which included: physics of laser ablation, phase transformations, material characterization, tissue regeneration, and biology.

The main objective of this dissertation was to introduce a new technique for direct fabrication of three-dimensional (3-D) interwoven nanofibrous platforms using femtosecond laser ablation of solids in ambient conditions.

The mechanism of ablation of solids by multiple femtosecond laser pulses in ambient air was described in an explicit analytical form. It was indicated that at the presence of air, collisions between the gas atoms and the surface markedly reduce the lifetime of this non-equilibrium surface state which allows thermal evaporation to proceed

before the surface cools. The formulas for evaporation rates and the number of ablated particles for laser ablation by a single pulse as well as multiple pulses as a function of laser parameters, background gas, and material properties were predicted and compared to experimental results of Ti ablation. The calculated dependence of the evaporation rate on the pulse repetition and laser pulse dwell time was in accordance with the experimental data. Later, the formation mechanism of the nanofibrous structures during femtosecond laser ablation of targets in the presence of air is discussed. The results from ablation of Ti, Si, and eggshell targets indicated that femtosecond laser ablation of solids at air background yields crystalline nanostructures. The formation of crystalline nanostructures is preceded through thermal mechanism of nucleation and growth. It also described that this technique allowed the synthesis of micro/nanofibrous structure on both synthetic materials such as Ti and Si as well as natural biomaterial including eggshell, rice husk, and wheat straw.

Potential usage of the presented technique for incorporation of nanostructures on transparent platforms as well as inside microstructures toward device fabrication was demonstrated. Femtosecond laser irradiated silicon nanofibrous structures were incorporated into microchannels in one step. Presented studies showed that integrated nanostructure inside microchannels can be fabricated in one single step using this technique. The experiments showed that by controlling the laser parameters including pulse repetition, pulse width and scanning speed, different microfluidic channels with different porosity and pore density could be obtained.

A new method, Laser induced reverse transfer (LIRT), was demonstrated for the deposition of metallic and semiconductor fibrous nanostructure on a transparent acceptor. It was found that the gap between the transparent acceptor and the target played an essential role in the nanostructure formation and the density of nanofiber accumulation. Experimental results also showed that size, length, density of aggregates and location of growth could be controlled by laser parameters. The generation and deposition of nanofibrous structure was completed in a single step at an ambient condition.

The 3-D titania nanostructures were incorporated into platforms used for tissue regeneration. Then, several *in vitro* studies were performed to evaluate the bioactivity and biocompatibility of the nanostructures. The fabricated structures incorporated the functions of 3-D nano-scaled topography and modified chemical properties to improve osseointegration. *In vitro* bioassays revealed that the titania nanofibrous platform possessed an excellent bioactivity and could induce rapid, uniform, and controllable bone-like apatite precipitation once immersed in simulated body fluid (SBF). The results indicated that the surface morphology as well as surface physiochemical properties (surface reactivity and wettability) of the nanofibrous layers significantly influenced their apatite-inducing capability. It was demonstrated that laser ablation of the Ti surface resulted in formation of rutile and anatase phases that enhanced the apatite deposition and adhesion rate on Ti platform. A surface with a denser nanofiber layer showed a higher apatite-inducing ability.

Furthermore, the influence of fabricated Ti platforms on the *in vitro* proliferation and viability of osteoblast-like MC3T3-E1 cells and NIH 3T3 mouse embryonic fibroblasts

was investigated. The results from *in vitro* studies pointed out that the titania nanofibrous platforms had outstanding biocompatibility and significantly enhanced proliferation of both cell lines compared to the untreated titanium platform. The cell numbers on the substrates change consistently with the density of nanofibrous structures.

The main contribution of this dissertation can be highlighted as follows:

A new technique for direct fabrication of three-dimensional (3-D) interwoven nanofibrous platforms using MHz femtosecond laser processing of solids in ambient conditions was demonstrated; unlike conventional techniques which requires multi-step process and complicated setup and procedure to generate nanostructures, the proposed technique allows a versatile, clean, single-step process to fabricate 3-D web-like nanostructures on a wide range materials in ambient environment. This technique offers the fabrication of 3-D interwoven nanostructures while other conventional techniques only support the generation of 1-D or 2-D nanostructures.

The mechanism of ablation of solids by multiple femtosecond laser pulses in ambient air was described in an explicit analytical form; the formulas for evaporation rates and the number of ablated particles for laser ablation by a single pulse as well as multiple pulses as a function of laser parameters, background gas, and material properties were predicted and compared to experimental results of ablation Ti targets.

A new method based on femtosecond laser processing was demonstrated to incorporate nanofibrous structures into microstructures in one single step; the integrated membranes (nanofibrous structure) inside microchannels were fabricated in one single step in ambient air using this method.

A new method, LIRT, was proposed for controllable site-specific deposition of nanofibrous structure; the LIRT method made it possible to synthesis and deposit nanofibrous structure of metallic and semiconductor targets on transparent acceptor in a single step process at an ambient condition.

A new method was demonstrated for the incorporation of 3-D titania nanostructures into platforms used for tissue regeneration; the fabricated platforms incorporated the functions of 3-D nano-scaled topography and modified chemical properties to improve osseointegration. Several *in vitro* studies were performed to evaluate the bioactivity and biocompatibility of the nanostructures. *In vitro* bioactivity assay revealed that the titania nanofibrous platform possessed an excellent bioactivity and could induce rapid, uniform, and controllable bone-like apatite precipitation once immersed in SBF. Furthermore, the influence of fabricated Ti platforms on the *in vitro* proliferation and viability of different cell lines was investigated. The results from *in vitro* studies pointed out that the titania nanofibrous platforms had outstanding biocompatibility compared to the conventional titanium platform.

7.2 Recommended future work

Although, good progress was made through studying the properties of new materials, still there are many unanswered questions and exciting avenues of research to explore with femtosecond laser ablation of both synthetic and natural materials. These avenues cross many fields including tissue engineering, biological sensors, solar cells and more. Those that are relevant to this dissertation are brought here.

Further research on the mechanism of ablation of Ti and Si can be done at various laser pulse wavelengths. Also, the physics of ablation of solids can be performed at different background gas to investigate the influence of ambient gas on material ablation and the synthesized nanostructures.

Research can be performed to further understand the mechanism of ablation of natural material in air background.

Work needs to be done to evaluate the degradation properties of both synthetic and natural material when implanted in biological environment

Studies can be performed to examine the bioactivity and biocompatibility of generated nanostructures on natural materials studied over the course of this dissertation.

Much research needs to be done on the influence of 3-D web-like nanostructures on Osteoblast differentiation as well as protein adsorption.

APPENDICES

APPENDIX A

A. List of publications

A.1 Refereed Journal

1. **A. Tavangar**, B. Tan, and K. Venkatakrisnan, "Study of the Formation of 3-D Titania Nanofibrous Structure by MHz Femtosecond Laser in Ambient Air," *Journal of Applied Physics*, vol. 113, no 2, pp. 023102-023110, Jan. 2013.
2. **A. Tavangar**, B. Tan, and K. Venkatakrisnan, "Synthesis of bio-functionalized three-dimensional titania nanofibrous structures using femtosecond laser ablation," *Acta Biomaterialia*, vol. 7, no. 6, pp. 2726–2732, Jun. 2011.
3. **A. Tavangar**, B. Tan, and K. Venkatakrisnan, "Synthesis of three-dimensional calcium carbonate nanofibrous structure from eggshell using femtosecond laser ablation," *J. Nanobiotechnol.*, vol. 9, Jan. 2011.
4. **A. Tavangar**, B. Tan, and K. Venkatakrisnan, "Single-step fabrication of microfluidic channels filled with nanofibrous membrane using femtosecond laser irradiation," *Journal of Micromechanics and Microengineering*, vol. 20, p. 085016, 2010.

5. **A. Tavangar**, B. Tan, and K. Venkatakrishnan, "Deposition of fibrous nanostructure by ultrafast laser ablation," *Journal of Micromechanics and Microengineering*, vol. 20, p. 055002, 2010.

A.2 Refereed conference papers

1. **A. Tavangar**, B. Tan, K. Venkatakrishnan, "Bioactivation of Titanium Surfaces by Femtosecond laser Processing," *Nanotech* 2011; 3: 229 - 232.

2. **A. Tavangar**, B. Tan, K. Venkatakrishnan, "Rapid Fabrication of Nanofibrous Membranes inside microchannels using Femtosecond Laser Micromachining," *Nanotech* 2011; 2: 246 - 248.

3. **A. Tavangar**, B. Tan, K. Venkatakrishnan, "Deposition of Interwoven Fibrous Nanostructure using Ultrafast Laser Ablation in Ambient Condition," *Nanotech* 2010; 2: 257 - 259.

A.3 Submitted to refereed journals

1. **A. Tavangar**, B. Tan, and K. Venkatakrishnan, "The Influence of Engineered Titania 3-D Nanofibrous Platforms on Cell Behavior," *Journal of Biomedical Nanotechnology*.

2. **A. Tavangar**, B. Tan, and K. Venkatakrishnan, "Formation of 3-D Biomorphous silica Nanofibrous Structure from Rice Husk Using Ultrashort Laser Processing," *Applied Physics Letters*.

APPENDIX B

B. Recipe for preparing simulated body fluid (SBF) and procedure of bioactivity test

B.1 Preparation of modified simulated body fluid (m-SBF)

B.1.1 Reagents for m-SBF

The following reagents in addition to ion-exchanged distilled water are used for the preparation of m-SBF:

- (1) Sodium chloride (NaCl),
- (2) Sodium hydrogen carbonate (NaHCO₃),
- (3) Sodium carbonate (Na₂CO₃),
- (4) Potassium chloride (KCl),
- (4) di-potassium hydrogen phosphate trihydrate (K₂HPO₄·3H₂O),
- (5) Magnesium chloride hexahydrate (MgCl₂·6H₂O),
- (6) Sodium hydroxide (NaOH),

(7) 2-(4-(2-hydroxyethyl)-1-piperazinyl)ethanesulfonic acid (HEPES),

(8) Calcium chloride (CaCl_2),

(9) Sodium sulfate (Na_2SO_4).

B.1.2. Ion concentrations of m-SBF

The ion concentrations of m-SBF are shown in Table 6.1.

B.1.3. Preparation procedure of m-SBF

As SBF is a supersaturated solution, special care should be taken during its preparation in order to avoid the precipitation of apatite in the solution. It should be borne in mind that the solution is retained transparent throughout the preparation and no precipitation on the surface of the bottle is observed. If any precipitation happens during or after the SBF preparation, the solution must be discarded and the procedure should be restarted from the beginning [151].

Table B.1 lists the reagents, their amounts and purity as well as the order of dissolution for preparing 1000 mL of the m-SBF. First, 700 mL of ion-exchanged distilled water is poured into a 1000-mL plastic beaker (polypropylene beaker recommended), heated, and stirred at 36.5°C [177].

The reagents need to be dissolved in the water in the order listed in Table B.1, after each reagent is entirely dissolved. 2-(4-(2-hydroxyethyl)-1-piperazinyl)ethanesulfonic acid (HEPES) is the buffer agent. HEPES is to be earlier dissolved in 100 mL of 0.2M NaOH aqueous solution. The final pH of the solution is later attuned to 7.40 at 36.5°C by carefully adding 1.0M NaOH aqueous. The solution is then transferred to a 1000-mL volumetric

Pyrex glass flask and chilled to 20°C before being diluted to a total volume of 1000 mL by adding ion-exchanged distilled water.

Table B.1 Order, amounts, and purities of reagents for preparing 1000 ml of m-SBF, adopted from [177]

Order	Reagents	Amount	Purity (%)
1	<i>NaCl</i>	5.403 g	>99.5
2	<i>NaHCO₃</i>	0.504 g	>99.5
3	<i>Na₂CO₃</i>	0.426 g	>99.5
4	<i>KCl</i>	0.225 g	>99.5
5	<i>K₂HPO₄·H₂O</i>	0.230 g	>99.0
6	<i>MgCl₂·6H₂O</i>	0.311 g	>98.0
7	<i>0.2M NaOH</i>	100 mL ^a	N/A
8	<i>HEPES</i>	17.892 g	>99.9
9	<i>CaCl₂</i>	0.293 g	>95.0
10	<i>Na₂SO₄</i>	0.072 g	>99.0
11	<i>1.0M NaOH</i>	15 mL	N/A

^a*HEPES* is already dissolved in 100 mL of 0.2M NaOH.

B.1.4. Preservation of SBF

Prepared SBF should be kept at 5-10 °C in a refrigerator and may be used within 30 days after preparation.

B.2. Procedure of apatite-forming ability test

The volume of SBF used for bioactivity testing dense materials can be calculated using $V_{SBF} = S_s/10$, where V_{SBF} is the volume of SBF (ml), and S_{DM} is the surface area of the specimen (mm^2).

For porous materials, however, the volume of SBF should be greater than the calculated V_{SBF} . The calculated volume of SBF is then poured into a plastic container. Afterwards, the SBF should be placed in an incubator and heated gradually to 37 °C. Then, the specimen is recommended to be positioned upright in the SBF solution. The specimen should be entirely submerged in the solution. One should note that once the specimen taken out of SBF and dried should not be soaked again [151].

APPENDIX C

C. Cell culture and assays

C.1 Cell culture

All products were purchased from Sigma-Aldrich unless otherwise mentioned. NIH3T3 mouse embryonic fibroblasts and osteoblast-like MC3T3-E1 cells purchased from ATCC, USA, were used in this study. Cryopreserved cell suspensions were stored in a -150°C freezer until use. Prior to cell culture they were thawed in a water bath at 37°C. NIH3T3 cells were suspended in Dulbecco's Modified Eagle Medium (DMEM) supplemented with antibiotic and fetal bovine serum. The cell suspensions were added to 75 cm^2 culture flasks and incubated at 37 °C under a 5% CO_2 atmosphere. The cell suspensions were subcultured when they reached 70–90% confluence. The cells were transferred to tubes and centrifuged at 930 rpm for 8 mins, forming a cell pellet that was resuspended in the appropriate culture medium. Concentrations of 5×10^6 cells were suspended in 13 ml of the appropriate culture medium. The cell suspensions were added to 75 cm^2 culture flasks

and incubated at 37 °C under a 5% CO_2 atmosphere. The first medium change took place between 24 and 36 hours after initial culture; subsequent medium changes occurred every other day. The cells were seeded on an as-received grade 2 titanium foils (control) and titania synthesized nanofibrous structures, two different structure density (all substrates 1cm^2), in a 24-well plate. Prior to the seeding, all substrates were sterilized and conditioned. The substrates were subjected to 2 hours UV exposure. The cells were seeded at an initial density of 5×10^6 cells. The substrates were incubated at 37 °C under a 5% CO_2 atmosphere and examined for proliferation and cytotoxicity assays after 48h culture.

C.2 Cell proliferation

In vitro proliferation of the cells was performed using 3-(4,5-Dimethylthiazol-2-Yl)-2,5-Diphenyltetrazolium Bromide (MTT) assay. MTT is a water soluble yellow tetrazolium salt which can be absorbed by metabolically active cells and converted into formazan dyes, giving a purple color. Prior to the measuring MTT activity, cell media was added to 2.54mg/ml of MTT in dulbecco's phosphate buffered saline (DPBS), and incubated for 4 hours. After incubation, the clear liquid was aspirated and dimethyl sulfoxide (DMSO) was added to dissolve formazan crystals. Absorbance was measured at 540 nm. Colorimetric analysis and comparison to a standard curve of known viable cell number can be employed to determine viable cell number for each condition.

REFERENCES

- [1] L. Zhang and T. J. Webster, "Nanotechnology and nanomaterials: promises for improved tissue regeneration," *Nano Today*, vol. 4, no. 1, pp. 66–80, 2009.
- [2] B. D. Gates, Q. Xu, M. Stewart, D. Ryan, C. G. Willson, G. M. Whitesides, and others, "New approaches to nanofabrication: molding, printing, and other techniques," *Chemical Reviews-Columbus*, vol. 105, no. 4, pp. 1171–1196, 2005.
- [3] K. Ariga, J. P. Hill, M. V. Lee, A. Vinu, R. Charvet, and S. Acharya, "Challenges and breakthroughs in recent research on self-assembly," *Science and Technology of Advanced Materials*, vol. 9, p. 014109, 2008.
- [4] V. J. Chen and P. X. Ma, "Nano-fibrous poly (L-lactic acid) scaffolds with interconnected spherical macropores," *Biomaterials*, vol. 25, no. 11, pp. 2065–2073, 2004.
- [5] J. R. Venugopal, S. Low, A. T. Choon, A. B. Kumar, and S. Ramakrishna, "Nanobioengineered electrospun composite nanofibers and osteoblasts for bone regeneration," *Artificial organs*, vol. 32, no. 5, pp. 388–397, 2008.
- [6] K. Hata, D. N. Futaba, K. Mizuno, T. Namai, M. Yumura, and S. Iijima, "Water-assisted highly efficient synthesis of impurity-free single-walled carbon nanotubes," *Science*, vol. 306, no. 5700, pp. 1362–1364, 2004.
- [7] S. Sun, H. Zeng, D. B. Robinson, S. Raoux, P. M. Rice, S. X. Wang, and G. Li, "Monodisperse MFe₂O₄ (M= Fe, Co, Mn) nanoparticles," *Journal of the American Chemical Society*, vol. 126, no. 1, pp. 273–279, 2004.
- [8] B. D. Fahlman, "What is Materials Chemistry?," *Materials Chemistry*, pp. 1–12, 2011.
- [9] S. P. Albu, A. Ghicov, J. M. Macak, R. Hahn, and P. Schmuki, "Self-organized, free-standing TiO₂ nanotube membrane for flow-through photocatalytic applications," *Nano letters*, vol. 7, no. 5, pp. 1286–1289, 2007.

- [10] K. Vasilev, Z. Poh, K. Kant, J. Chan, A. Michelmore, and D. Losic, "Tailoring the surface functionalities of titania nanotube arrays," *Biomaterials*, vol. 31, no. 3, pp. 532–540, 2010.
- [11] S. Yoriya, G. K. Mor, S. Sharma, and C. A. Grimes, "Synthesis of ordered arrays of discrete, partially crystalline titania nanotubes by Ti anodization using diethylene glycol electrolytes," *J. Mater. Chem.*, vol. 18, no. 28, pp. 3332–3336, 2008.
- [12] C. C. Wang, C. Y. Yu, C. C. Kei, C. T. Lee, and T. P. Perng, "The formation of TiO₂ nanowires directly from nanoparticles," *Nanotechnology*, vol. 20, p. 285601, 2009.
- [13] G. K. Mor, O. K. Varghese, M. Paulose, and C. A. Grimes, "Transparent highly ordered TiO₂ nanotube arrays via anodization of titanium thin films," *Advanced Functional Materials*, vol. 15, no. 8, pp. 1291–1296, 2005.
- [14] S. M. Liu, L. M. Gan, L. H. Liu, W. D. Zhang, and H. C. Zeng, "Synthesis of single-crystalline TiO₂ nanotubes," *Chemistry of materials*, vol. 14, no. 3, pp. 1391–1397, 2002.
- [15] Y. Lei, L. D. Zhang, G. W. Meng, G. H. Li, X. Y. Zhang, C. H. Liang, W. Chen, and S. X. Wang, "Preparation and photoluminescence of highly ordered TiO nanowire arrays," *Applied Physics Letters*, vol. 78, p. 1125, 2001.
- [16] B. D. Yao, Y. F. Chan, X. Y. Zhang, W. F. Zhang, Z. Y. Yang, and N. Wang, "Formation mechanism of TiO₂ nanotubes," *Applied physics letters*, vol. 82, no. 2, pp. 281–283, 2003.
- [17] N. F. Fahim and T. Sekino, "A novel method for synthesis of titania nanotube powders using rapid breakdown anodization," *Chemistry of Materials*, vol. 21, no. 9, pp. 1967–1979, 2009.
- [18] S. Rani, S. C. Roy, M. Paulose, O. K. Varghese, G. K. Mor, S. Kim, S. Yoriya, T. J. LaTempa, and C. A. Grimes, "Synthesis and applications of electrochemically self-assembled titania nanotube arrays," *Phys. Chem. Chem. Phys.*, vol. 12, no. 12, pp. 2780–2800, 2010.
- [19] B. S. Kim and I. S. Kim, "Recent Nanofiber Technologies," *Polymer Reviews*, vol. 51, no. 3, pp. 235–238, 2011.
- [20] A. Bogaerts, Z. Chen, R. Gijbels, and A. Vertes, "Laser ablation for analytical sampling: what can we learn from modeling?," *Spectrochimica Acta Part B: Atomic Spectroscopy*, vol. 58, no. 11, pp. 1867–1893, Nov. 2003.
- [21] D. B. Chrisey, A. Pique, R. A. McGill, J. S. Horwitz, B. R. Ringeisen, D. M. Bubb, and P. K. Wu, "Laser deposition of polymer and biomaterial films," *ChemInform*, vol. 34, no. 18, p. no–no, 2003.
- [22] R. Cristescu, I. Stamatina, D. E. Mihaiescu, C. Ghica, M. Albuiescu, I. N. Mihaiescu, and D. B. Chrisey, "Pulsed laser deposition of biocompatible polymers: a comparative study in case of pullulan," *Thin solid films*, vol. 453, pp. 262–268, 2004.

- [23] T. C. Chen and R. B. Darling, "Parametric studies on pulsed near ultraviolet frequency tripled Nd: YAG laser micromachining of sapphire and silicon," *Journal of materials processing technology*, vol. 169, no. 2, pp. 214–218, 2005.
- [24] T. C. Chen and R. B. Darling, "Laser micromachining of the materials using in microfluidics by high precision pulsed near and mid-ultraviolet Nd: YAG lasers," *Journal of materials processing technology*, vol. 198, no. 1–3, pp. 248–253, 2008.
- [25] A. Tavangar, B. Tan, and K. Venkatakrishnan, "Single-step fabrication of microfluidic channels filled with nanofibrous membrane using femtosecond laser irradiation," *Journal of Micromechanics and Microengineering*, vol. 20, p. 085016, 2010.
- [26] J. Meijer, K. Du, A. Gillner, D. Hoffmann, V. S. Kovalenko, T. Masuzawa, A. Ostendorf, R. Poprawe, and W. Schulz, "Laser machining by short and ultrashort pulses, state of the art and new opportunities in the age of the photons," *CIRP Annals-Manufacturing Technology*, vol. 51, no. 2, pp. 531–550, 2002.
- [27] C. Hosokawa, S. N. Kudoh, A. Kiyohara, and T. Taguchi, "Resynchronization in neuronal network divided by femtosecond laser processing," *NeuroReport*, vol. 19, no. 7, p. 771, 2008.
- [28] C. Hosokawa, S. N. Kudoh, A. Kiyohara, Y. Hosokawa, K. Okano, H. Masuhara, and T. Taguchi, "Femtosecond laser modification of living neuronal network," *Applied Physics A: Materials Science & Processing*, vol. 93, no. 1, pp. 57–63, 2008.
- [29] E. G. Gamaly, A. V. Rode, B. Luther-Davies, and V. T. Tikhonchuk, "Ablation of solids by femtosecond lasers: Ablation mechanism and ablation thresholds for metals and dielectrics," *Physics of plasmas*, vol. 9, p. 949, 2002.
- [30] B. C. Stuart, M. D. Feit, A. M. Rubenchik, B. W. Shore, and M. D. Perry, "Laser-induced damage in dielectrics with nanosecond to subpicosecond pulses," *Physical Review Letters*, vol. 74, no. 12, pp. 2248–2251, 1995.
- [31] S. Nolte, C. Momma, H. Jacobs, A. Tünnermann, B. N. Chichkov, B. Wellegehausen, and H. Welling, "Ablation of metals by ultrashort laser pulses," *JOSA B*, vol. 14, no. 10, pp. 2716–2722, 1997.
- [32] X. Liu, D. Du, and G. Mourou, "Laser ablation and micromachining with ultrashort laser pulses," *Quantum Electronics, IEEE Journal of*, vol. 33, no. 10, pp. 1706–1716, 1997.
- [33] P. J. Scully, D. Jones, and D. A. Jaroszynski, "Femtosecond laser irradiation of polymethylmethacrylate for refractive index gratings," *Journal of Optics A: Pure and Applied Optics*, vol. 5, p. S92, 2003.
- [34] B. Girard, D. Yu, M. R. Armstrong, B. C. Wilson, C. M. L. Clokie, and R. J. Miller, "Effects of femtosecond laser irradiation on osseous tissues," *Lasers in surgery and medicine*, vol. 39, no. 3, pp. 273–285, 2007.
- [35] A. Tavangar, B. Tan, and K. Venkatakrishnan, "Synthesis of bio-functionalized three-dimensional titania nanofibrous structures using femtosecond laser ablation," *Acta Biomaterialia*, vol. 7, no. 6, pp. 2726–2732, Jun. 2011.

- [36] M. K. Bhuyan, F. Courvoisier, P. A. Lacourt, M. Jacquot, L. Furfaro, M. J. Withford, and J. M. Dudley, "High aspect ratio taper-free microchannel fabrication using femtosecond Bessel beams," *Optics Express*, vol. 18, no. 2, pp. 566–574, 2010.
- [37] K. C. Vishnubhatla, N. Bellini, R. Ramponi, G. Cerullo, and R. Osellame, "Shape control of microchannels fabricated in fused silica by femtosecond laser irradiation and chemical etching," *Optics express*, vol. 17, no. 10, pp. 8685–8695, 2009.
- [38] L. Zhao, L. Jiang, S. Wang, H. Xiao, Y. Lu, and H. L. Tsai, "A high-quality Mach-Zehnder interferometer fiber sensor by femtosecond laser one-step processing," *Sensors*, vol. 11, no. 1, pp. 54–61, 2010.
- [39] C. H. Lee, Y. C. Lim, D. F. Farson, H. M. Powell, and J. J. Lannutti, "Vascular Wall Engineering Via Femtosecond Laser Ablation: Scaffolds with Self-Containing Smooth Muscle Cell Populations," *Annals of biomedical engineering*, pp. 1–11, 2011.
- [40] C. P. Barnes, S. A. Sell, E. D. Boland, D. G. Simpson, and G. L. Bowlin, "Nanofiber technology: designing the next generation of tissue engineering scaffolds," *Advanced drug delivery reviews*, vol. 59, no. 14, pp. 1413–1433, 2007.
- [41] C. F. . Kuo, S. W. Liang, and H. M. Tu, "Optimization Parameters of Femtosecond Laser Isolation Processing for a Microcrystalline Silicon Thin Film Solar Cell," *Materials and Manufacturing Processes*, vol. 26, no. 10, pp. 1310–1318, 2011.
- [42] M. Long, H. J. Rack, and others, "Titanium alloys in total joint replacement-a materials science perspective," *BIOMATERIALS-GUILDFORD-*, vol. 19, pp. 1621–1639, 1998.
- [43] M. Jayaraman, U. Meyer, M. Bühner, U. Joos, and H. P. Wiesmann, "Influence of titanium surfaces on attachment of osteoblast-like cells in vitro," *Biomaterials*, vol. 25, no. 4, pp. 625–631, 2004.
- [44] P. Xiao, B. B. Garcia, Q. Guo, D. Liu, and G. Cao, "TiO₂ nanotube arrays fabricated by anodization in different electrolytes for biosensing," *Electrochemistry communications*, vol. 9, no. 9, pp. 2441–2447, 2007.
- [45] K. Besteman, J. O. Lee, F. G. M. Wiertz, H. A. Heering, and C. Dekker, "Enzyme-coated carbon nanotubes as single-molecule biosensors," *Nano Letters*, vol. 3, no. 6, pp. 727–730, 2003.
- [46] M. Paulose, K. Shankar, O. K. Varghese, G. K. Mor, B. Hardin, and C. A. Grimes, "Backside illuminated dye-sensitized solar cells based on titania nanotube array electrodes," *Nanotechnology*, vol. 17, p. 1446, 2006.
- [47] G. K. Mor, K. Shankar, M. Paulose, O. K. Varghese, and C. A. Grimes, "Use of highly-ordered TiO₂ nanotube arrays in dye-sensitized solar cells," *Nano Letters*, vol. 6, no. 2, pp. 215–218, 2006.
- [48] S. P. Albu, A. Ghicov, J. M. Macak, R. Hahn, and P. Schmuki, "Self-organized, free-standing TiO₂ nanotube membrane for flow-through photocatalytic applications," *Nano letters*, vol. 7, no. 5, pp. 1286–1289, 2007.

- [49] Z. Liu, D. D. Sun, P. Guo, and J. O. Leckie, "An efficient bicomponent TiO₂/SnO₂ nanofiber photocatalyst fabricated by electrospinning with a side-by-side dual spinneret method," *Nano letters*, vol. 7, no. 4, pp. 1081–1085, 2007.
- [50] R. Jayakumar, R. Ramachandran, V. V. Divyarani, K. P. Chennazhi, H. Tamura, and S. V. Nair, "Fabrication of chitin–chitosan/nano TiO₂-composite scaffolds for tissue engineering applications," *International Journal of Biological Macromolecules*, vol. 48, no. 2, pp. 336–344, 2011.
- [51] R. Langer, "Biomaterials in drug delivery and tissue engineering: one laboratory's experience," *Accounts of Chemical Research*, vol. 33, no. 2, pp. 94–101, 2000.
- [52] K. Vasilev, Z. Poh, K. Kant, J. Chan, A. Michelmore, and D. Losic, "Tailoring the surface functionalities of titania nanotube arrays," *Biomaterials*, vol. 31, no. 3, pp. 532–540, 2010.
- [53] A. Palmquist, O. M. Omar, M. Esposito, J. Lausmaa, and P. Thomsen, "Titanium oral implants: surface characteristics, interface biology and clinical outcome," *Journal of The Royal Society Interface*, vol. 7, no. Suppl 5, pp. S515–S527, 2010.
- [54] M. J. Dalby, D. McCloy, M. Robertson, C. D. W. Wilkinson, and R. O. C. Oreffo, "Osteoprogenitor response to defined topographies with nanoscale depths," *Biomaterials*, vol. 27, no. 8, pp. 1306–1315, 2006.
- [55] F. Variola, J. H. Yi, L. Richert, J. D. Wuest, F. Rosei, and A. Nanci, "Tailoring the surface properties of Ti6Al4V by controlled chemical oxidation," *Biomaterials*, vol. 29, no. 10, pp. 1285–1298, 2008.
- [56] G. K. Mor, O. K. Varghese, M. Paulose, and C. A. Grimes, "Transparent Highly Ordered TiO₂ Nanotube Arrays via Anodization of Titanium Thin Films," *Advanced Functional Materials*, vol. 15, no. 8, pp. 1291–1296, 2005.
- [57] G. Li Puma, A. Bono, D. Krishnaiah, and J. G. Collin, "Preparation of titanium dioxide photocatalyst loaded onto activated carbon support using chemical vapor deposition: A review paper," *Journal of hazardous materials*, vol. 157, no. 2, pp. 209–219, 2008.
- [58] B. D. Yao, Y. F. Chan, X. Y. Zhang, W. F. Zhang, Z. Y. Yang, and N. Wang, "Formation mechanism of TiO₂ nanotubes," *Applied Physics Letters*, vol. 82, no. 2, pp. 281–283, Jan. 2003.
- [59] N. F. Fahim and T. Sekino, "A Novel Method for Synthesis of Titania Nanotube Powders using Rapid Breakdown Anodization," *Chem. Mater.*, vol. 21, no. 9, pp. 1967–1979, 2009.
- [60] J. Perrière, C. Boulmer-Leborgne, R. Benzerga, and S. Tricot, "Nanoparticle formation by femtosecond laser ablation," *Journal of Physics D: Applied Physics*, vol. 40, no. 22, pp. 7069–7076, Nov. 2007.
- [61] M. Ullmann, S. K. Friedlander, and A. Schmidt-Ott, "Nanoparticle Formation by Laser Ablation," *Journal of Nanoparticle Research*, vol. 4, no. 6, pp. 499–509, 2002.

- [62] X. B. Chen, Y. C. Li, P. D. Hodgson, and C. Wen, "The importance of particle size in porous titanium and nonporous counterparts for surface energy and its impact on apatite formation," *Acta biomaterialia*, vol. 5, no. 6, pp. 2290–2302, 2009.
- [63] E. M. Christenson, K. S. Anseth, J. J. P. van den Beucken, C. K. Chan, B. Ercan, J. A. Jansen, C. T. Laurencin, W. J. Li, R. Murugan, L. S. Nair, and others, "Nanobiomaterial applications in orthopedics," *Journal of orthopaedic research*, vol. 25, no. 1, pp. 11–22, 2007.
- [64] G. Kotzar, M. Freas, P. Abel, A. Fleischman, S. Roy, C. Zorman, J. M. Moran, and J. Melzak, "Evaluation of MEMS materials of construction for implantable medical devices," *Biomaterials*, vol. 23, no. 13, pp. 2737–2750, 2002.
- [65] C. C. Striemer, T. R. Gaborski, J. L. McGrath, and P. M. Fauchet, "Charge-and size-based separation of macromolecules using ultrathin silicon membranes," *Nature*, vol. 445, no. 7129, pp. 749–753, 2007.
- [66] T. M. Benn and P. Westerhoff, "Nanoparticle silver released into water from commercially available sock fabrics," *Environmental Science & Technology*, vol. 42, no. 11, pp. 4133–4139, 2008.
- [67] C. You, C. Han, X. Wang, Y. Zheng, Q. Li, X. Hu, and H. Sun, "The progress of silver nanoparticles in the antibacterial mechanism, clinical application and cytotoxicity," *Molecular biology reports*, pp. 1–9, 2012.
- [68] Y. F. Li and C. Chen, "Fate and Toxicity of Metallic and Metal-Containing Nanoparticles for Biomedical Applications," *Small*, vol. 7, no. 21, pp. 2965–2980, 2011.
- [69] E. Hjørting-Hansen, "Bone grafting to the jaws with special reference to reconstructive preprosthetic surgery," *Oral and Maxillofacial Surgery*, vol. 6, no. 1, pp. 6–14, 2002.
- [70] J. W. Park, J. H. Jang, S. R. Bae, C. H. An, and J. Y. Suh, "Bone formation with various bone graft substitutes in critical-sized rat calvarial defect," *Clinical oral implants research*, vol. 20, no. 4, pp. 372–378, 2009.
- [71] L. Meijndert, G. M. Raghoobar, P. Schüpbach, H. J. A. Meijer, and A. Vissink, "Bone quality at the implant site after reconstruction of a local defect of the maxillary anterior ridge with chin bone or deproteinised cancellous bovine bone," *International journal of oral and maxillofacial surgery*, vol. 34, no. 8, pp. 877–884, 2005.
- [72] J. W. Park, S. R. Bae, J. Y. Suh, D. H. Lee, S. H. Kim, H. Kim, and C. S. Lee, "Evaluation of bone healing with eggshell-derived bone graft substitutes in rat calvaria: A pilot study," *Journal of Biomedical Materials Research Part A*, vol. 87, no. 1, pp. 203–214, 2008.
- [73] E. Durmuş, İ. Çelik, M. F. Aydın, G. Yıldırım, and E. Sur, "Evaluation of the biocompatibility and osteoproduative activity of ostrich eggshell powder in experimentally induced calvarial defects in rabbits," *Journal of Biomedical Materials Research Part B: Applied Biomaterials*, vol. 86, no. 1, pp. 82–89, 2008.

- [74] D. Siva Rama Krishna, A. Siddharthan, S. K. Seshadri, and T. S. Sampath Kumar, "A novel route for synthesis of nanocrystalline hydroxyapatite from eggshell waste," *Journal of Materials Science: Materials in Medicine*, vol. 18, no. 9, pp. 1735–1743, 2007.
- [75] R. Vago, D. Plotquin, A. Bunin, I. Sinelnikov, D. Atar, and D. Itzhak, "Hard tissue remodeling using biofabricated coralline biomaterials," *Journal of biochemical and biophysical methods*, vol. 50, no. 2, pp. 253–259, 2002.
- [76] S. Haque, I. Rehman, and J. A. Darr, "Synthesis and characterization of grafted nanohydroxyapatites using functionalized surface agents," *Langmuir*, vol. 23, no. 12, pp. 6671–6676, 2007.
- [77] X. Liang, J. Xiang, F. Zhang, L. Xing, B. Song, and S. Chen, "Fabrication of Hierarchical CaCO₃ Mesoporous Spheres: Particle-Mediated Self-Organization Induced by Biphasic Interfaces and SAMs," *Langmuir*, vol. 26, no. 8, pp. 5882–5888, 2009.
- [78] R. A. Yukna and C. N. Yukna, "A 5-year follow-up of 16 patients treated with coralline calcium carbonate (Biocoral™) bone replacement grafts in infrabony defects*," *Journal of clinical periodontology*, vol. 25, no. 12, pp. 1036–1040, 1998.
- [79] N. Velich, Z. Németh, C. Tóth, and G. Szabó, "Long-term results with different bone substitutes used for sinus floor elevation," *Journal of Craniofacial Surgery*, vol. 15, no. 1, p. 38, 2004.
- [80] M. J. Coughlin, J. S. Grimes, M. P. Kennedy, and others, "Coralline hydroxyapatite bone graft substitute in hindfoot surgery.," *Foot & ankle international/American Orthopaedic Foot and Ankle Society [and] Swiss Foot and Ankle Society*, vol. 27, no. 1, p. 19, 2006.
- [81] H. Liao, H. Mutvei, M. Sjöström, L. Hammarström, and J. Li, "Tissue responses to natural aragonite (*Margaritifera* shell) implants in vivo," *Biomaterials*, vol. 21, no. 5, pp. 457–468, 2000.
- [82] L. Dupoirieux, D. Pourquier, M. Neves, and L. Téot, "Resorption kinetics of eggshell: an in vivo study," *Journal of Craniofacial Surgery*, vol. 12, no. 1, p. 53, 2001.
- [83] A. Siddharthan, T. S. Sampath Kumar, and S. K. Seshadri, "Synthesis and characterization of nanocrystalline apatites from eggshells at different Ca/P ratios," *Biomedical Materials*, vol. 4, p. 045010, 2009.
- [84] K. Fujihara, M. Kotaki, and S. Ramakrishna, "Guided bone regeneration membrane made of polycaprolactone/calcium carbonate composite nano-fibers," *Biomaterials*, vol. 26, no. 19, pp. 4139–4147, 2005.
- [85] K. P. Sanosh, M. C. Chu, A. Balakrishnan, T. N. Kim, and S. J. Cho, "Utilization of biowaste eggshells to synthesize nanocrystalline hydroxyapatite powders," *Materials Letters*, vol. 63, no. 24, pp. 2100–2102, 2009.
- [86] H. Chen, F. Wang, C. Zhang, Y. Shi, G. Jin, and S. Yuan, "Preparation of nano-silica materials: The concept from wheat straw," *Journal of Non-Crystalline Solids*, vol. 356, no. 50, pp. 2781–2785, 2010.

- [87] J. A. RAVEN, "The transport and function of silicon in plants," *Biological Reviews*, vol. 58, no. 2, pp. 179–207, 1983.
- [88] M. Sumper and N. Kröger, "Silica formation in diatoms: the function of long-chain polyamines and silaffins," *J. Mater. Chem.*, vol. 14, no. 14, pp. 2059–2065, Jul. 2004.
- [89] V. Bansal, A. Ahmad, and M. Sastry, "Fungus-Mediated Biotransformation of Amorphous Silica in Rice Husk to Nanocrystalline Silica," *J. Am. Chem. Soc.*, vol. 128, no. 43, pp. 14059–14066, Nov. 2006.
- [90] G. H. Bogush and C. F. Zukoski IV, "Studies of the kinetics of the precipitation of uniform silica particles through the hydrolysis and condensation of silicon alkoxides," *Journal of colloid and interface science*, vol. 142, no. 1, pp. 1–18, 1991.
- [91] L. C. Klein and D. Gallagher, "Pore structures of sol-gel silica membranes," *Journal of membrane science*, vol. 39, no. 3, pp. 213–220, 1988.
- [92] S. Amoruso, G. Ausanio, R. Bruzzese, M. Vitiello, and X. Wang, "Femtosecond laser pulse irradiation of solid targets as a general route to nanoparticle formation in a vacuum," *Physical Review B*, vol. 71, no. 3, p. 033406, 2005.
- [93] M. Momcilovic, J. Limpouch, V. Kmetik, R. Readelli, J. Savovic, D. Batani, J. Stasic, P. Panjan, and M. Trtica, "Surface modification of copper using high intensity, 10^{15} W/cm², femtosecond laser in vacuum," *Applied Surface Science*, 2012.
- [94] E. G. Gamaly, B. Luther-Davies, V. Z. Kolev, N. R. Madsen, M. Duering, and A. V. Rode, "Ablation of metals with picosecond laser pulses: Evidence of long-lived non-equilibrium surface states," *Laser and Particle Beams-Pulse Power and High Energy Densities*, vol. 23, no. 2, pp. 167–176, 2005.
- [95] T. E. Glover, "Hydrodynamics of particle formation following femtosecond laser ablation," *JOSA B*, vol. 20, no. 1, pp. 125–131, 2003.
- [96] I. N. Zavestovskaya, P. G. Eliseev, O. N. Krokhin, and N. A. Men'kova, "Analysis of the nonlinear absorption mechanisms in ablation of transparent materials by high-intensity and ultrashort laser pulses," *Applied Physics A: Materials Science & Processing*, vol. 92, no. 4, pp. 903–906, 2008.
- [97] E. G. Gamaly, "The physics of ultra-short laser interaction with solids at non-relativistic intensities," *Physics Reports*, 2011.
- [98] M. Cirisan, J. M. Jouvard, L. Lavisse, L. Hallo, and R. Oltra, "Laser plasma plume structure and dynamics in the ambient air: The early stage of expansion," *Journal of applied physics*, vol. 109, p. 103301, 2011.
- [99] M. F. Modest, J. F. Ready, and D. F. Farson, *Handbook of Laser Materials Processing*. Magnolia Publishing Inc., Orlando, USA, 2001.
- [100] J. Cheng, C. Liu, S. Shang, D. Liu, W. Perrie, G. Dearden, and K. Watkins, "A review of ultrafast laser materials micromachining," *Optics & Laser Technology*, 2012.

- [101] V. Schmidt, W. Husinsky, and G. Betz, "Dynamics of laser desorption and ablation of metals at the threshold on the femtosecond time scale," *Physical review letters*, vol. 85, no. 16, pp. 3516–3519, 2000.
- [102] A. Y. Vorobyev and C. Guo, "Reflection of femtosecond laser light in multipulse ablation of metals," *J. Appl. Phys.*, vol. 110, no. 4, Aug. 2011.
- [103] J. Siegel, J. Solis, C. N. Afonso, F. Vega, J. Bankmann, O. M. Sacristán, and K. Sokolowski-Tinten, "Evidence for surface initiated solidification in Ge films upon picosecond laser pulse irradiation," *Journal of Applied Physics*, vol. 89, p. 3642, 2001.
- [104] E. G. Gamaly, A. V. Rode, V. T. Tikhonchuk, and B. Luther-Davies, "Electrostatic mechanism of ablation by femtosecond lasers," *Applied surface science*, vol. 197, pp. 699–704, 2002.
- [105] E. G. Gamaly, N. R. Madsen, M. Duering, A. V. Rode, V. Z. Kolev, and B. Luther-Davies, "Ablation of metals with picosecond laser pulses: Evidence of long-lived nonequilibrium conditions at the surface," *Physical Review B*, vol. 71, no. 17, p. 174405, 2005.
- [106] N. M. Bulgakova, V. P. Zhukov, A. Y. Vorobyev, and C. Guo, "Modeling of residual thermal effect in femtosecond laser ablation of metals: role of a gas environment," *Applied Physics A: Materials Science & Processing*, vol. 92, no. 4, pp. 883–889, 2008.
- [107] I. A. . Zel'dovich, *Physics of shock waves and high-temperature hydrodynamic phenomena*. Dover Pubns, 2002.
- [108] E. G. Gamaly, A. V. Rode, and B. Luther-Davies, "Ultrafast ablation with high-pulse-rate lasers. Part I: Theoretical considerations," *Journal of applied physics*, vol. 85, p. 4213, 1999.
- [109] B. Tan, A. Dalili, and K. Venkatakrishnan, "High repetition rate femtosecond laser nano-machining of thin films," *Applied Physics A*, vol. 95, no. 2, pp. 537–545, Nov. 2008.
- [110] K. C. A. Smith and C. W. Oatley, "The scanning electron microscope and its fields of application," *British Journal of Applied Physics*, vol. 6, no. 11, pp. 391–399, Nov. 1955.
- [111] J. Goldstein, *Scanning Electron Microscopy and X-Ray Microanalysis*. Springer, 2003.
- [112] D. B. Williams, C. B. Carter, D. B. Williams, and C. B. Carter, "The Transmission Electron Microscope," in *Transmission Electron Microscopy*, Springer US, 2009, pp. 3–22.
- [113] A. Kalantarian, R. David, and A. W. Neumann, "Methodology for High Accuracy Contact Angle Measurement†," *Langmuir*, vol. 25, no. 24, pp. 14146–14154, 2009.
- [114] B. Tan and K. Venkatakrishnan, "Synthesis of fibrous nanoparticle aggregates by femtosecond laser ablation in air," *Optics Express*, vol. 17, no. 2, pp. 1064–1069, 2009.
- [115] K. Venkatakrishnan, B. Tan, P. Stanley, L. E. N. Lim, and B. K. A. Ngoi, "Femtosecond pulsed laser direct writing system," *Optical Engineering*, vol. 41, p. 1441, 2002.

- [116] M. D. Perry, B. C. Stuart, P. S. Banks, M. D. Feit, V. Yanovsky, and A. M. Rubenchik, "Ultrashort-pulse laser machining of dielectric materials," *J. Appl. Phys.*, vol. 85, no. 9, pp. 6803–6810, May 1999.
- [117] B. Luther-Davies, A. V. Rode, N. R. Madsen, and E. G. Gamaly, "Picosecond high-repetition-rate pulsed laser ablation of dielectrics: the effect of energy accumulation between pulses," *Optical Engineering*, vol. 44, p. 051102, 2005.
- [118] E. G. Gamaly, N. R. Madsen, D. Golberg, and A. V. Rode, "Expansion-limited aggregation of nanoclusters in a single-pulse laser-produced plume," *Phys. Rev. B*, vol. 80, no. 18, p. 184113, Nov. 2009.
- [119] A. De Giacomo, M. Dell'Aglio, A. Santagata, and R. Teghil, "Early stage emission spectroscopy study of metallic titanium plasma induced in air by femtosecond-and nanosecond-laser pulses," *Spectrochimica Acta Part B: Atomic Spectroscopy*, vol. 60, no. 7, pp. 935–947, 2005.
- [120] L. Jing, B. Xin, F. Yuan, L. Xue, B. Wang, and H. Fu, "Effects of Surface Oxygen Vacancies on Photophysical and Photochemical Processes of Zn-Doped TiO₂ Nanoparticles and Their Relationships," *J. Phys. Chem. B*, vol. 110, no. 36, pp. 17860–17865, 2006.
- [121] Q. Zhang, L. Gao, and J. Guo, "Effects of calcination on the photocatalytic properties of nanosized TiO₂ powders prepared by TiCl₄ hydrolysis," *Applied Catalysis B: Environmental*, vol. 26, no. 3, pp. 207–215, 2000.
- [122] I. Banerjee, S. Karmakar, N. V. Kulkarni, A. B. Nawale, V. L. Mathe, A. K. Das, and S. V. Bhoraskar, "Effect of ambient pressure on the crystalline phase of nano TiO₂ particles synthesized by a dc thermal plasma reactor," *Journal of Nanoparticle Research*, vol. 12, no. 2, pp. 581–590, 2010.
- [123] W. T. Tsai, J. M. Yang, H. C. Hsu, C. M. Lin, K. Y. Lin, and C. H. Chiu, "Development and Characterization of mesoporosity in eggshell ground by planetary ball milling," *Microporous and Mesoporous Materials*, vol. 111, no. 1, pp. 379–386, 2008.
- [124] S. Matsuya, X. Lin, K. Udoh, M. Nakagawa, R. Shimogoryo, Y. Terada, and K. Ishikawa, "Fabrication of porous low crystalline calcite block by carbonation of calcium hydroxide compact," *Journal of Materials Science: Materials in Medicine*, vol. 18, no. 7, pp. 1361–1367, 2007.
- [125] F. B. Bagambisa, U. Joos, and W. Schilli, "Mechanisms and structure of the bond between bone and hydroxyapatite ceramics," *Journal of biomedical materials research*, vol. 27, no. 8, pp. 1047–1055, 1993.
- [126] M. Neo, T. Nakamura, C. Ohtsuki, T. Kokubo, and T. Yamamuro, "Apatite formation on three kinds of bioactive material at an early stage in vivo: a comparative study by transmission electron microscopy," *Journal of biomedical materials research*, vol. 27, no. 8, pp. 999–1006, 1993.

- [127] H. Yamada, T. Sano, T. Nakayama, and I. Miyamoto, "Optimization of laser-induced forward transfer process of metal thin films," *Applied Surface Science*, vol. 197–198, pp. 411–415, Sep. 2002.
- [128] M. R. Papantonakis and R. F. Haglund Jr., "Picosecond pulsed laser deposition at high vibrational excitation density: the case of poly(tetrafluoroethylene)," *Applied Physics A: Materials Science & Processing*, vol. 79, no. 7, pp. 1687–1694, 2004.
- [129] B. Tan, K. Venkatakrishnan, and K. . Tok, "Selective surface texturing using femtosecond pulsed laser induced forward transfer," *Applied Surface Science*, vol. 207, no. 1–4, pp. 365–371, Feb. 2003.
- [130] V. P. Veiko, "Laser microshaping: Fundamentals, practical applications, and future prospects," *RIKEN REVIEW*, pp. 11–18, 2001.
- [131] A. I. Kuznetsov, J. Koch, and B. N. Chichkov, "Laser-induced backward transfer of gold nanodroplets," *Opt. Express*, vol. 17, no. 21, pp. 18820–18825, Oct. 2009.
- [132] M. L. Rigout, H. Niu, C. Qin, L. Zhang, C. Li, X. Bai, and N. Fan, "Fabrication and photoluminescence of hyperbranched silicon nanowire networks on silicon substrates by laser-induced forward transfer," *Nanotechnology*, vol. 19, no. 24, p. 245303, Jun. 2008.
- [133] L. V. Zhigilei, "Dynamics of the plume formation and parameters of the ejected clusters in short-pulse laser ablation," *Applied Physics A: Materials Science & Processing*, vol. 76, no. 3, pp. 339–350, 2003.
- [134] Y. Khang and J. Lee, "Synthesis of Si nanoparticles with narrow size distribution by pulsed laser ablation," *Journal of Nanoparticle Research*, vol. 12, no. 4, pp. 1349–1354, 2010.
- [135] E. Lescoute, L. Hallo, D. Hébert, B. Chimier, B. Etchessahar, V. T. Tikhonchuk, J.-M. Chevalier, and P. Combis, "Experimental observations and modeling of nanoparticle formation in laser-produced expanding plasma," *Physics of Plasmas*, vol. 15, no. 6, pp. 063507–063507–11, Jun. 2008.
- [136] S. R. Franklin and R. K. Thareja, "Simulation of cluster formation in laser-ablated silicon plumes," *Journal of Applied Physics*, vol. 97, no. 12, pp. 123303–123303–6, Jun. 2005.
- [137] S. Bera, A. J. Sabbah, J. M. Yarbrough, C. G. Allen, B. Winters, C. G. Durfee, and J. A. Squier, "Optimization study of the femtosecond laser-induced forward-transfer process with thin aluminum films," *Appl. Opt.*, vol. 46, no. 21, pp. 4650–4659, Jul. 2007.
- [138] T. Sano, H. Yamada, T. Nakayama, and I. Miyamoto, "Experimental investigation of laser induced forward transfer process of metal thin films," *Applied Surface Science*, vol. 186, no. 1–4, pp. 221–226, Jan. 2002.
- [139] V. Narayanan and R. . Thareja, "Emission spectroscopy of laser-ablated Si plasma related to nanoparticle formation," *Applied Surface Science*, vol. 222, no. 1–4, pp. 382–393, Jan. 2004.

- [140] A. Frenot and I. S. Chronakis, "Polymer nanofibers assembled by electrospinning," *Current opinion in colloid & interface science*, vol. 8, no. 1, pp. 64–75, 2003.
- [141] S. M. Cooper, B. A. Cruden, M. Meyyappan, R. Raju, and S. Roy, "Gas transport characteristics through a carbon nanotubule," *Nano Letters*, vol. 4, no. 2, pp. 377–381, 2004.
- [142] J. K. Holt, A. Noy, T. Huser, D. Eaglesham, and O. Bakajin, "Fabrication of a carbon nanotube-embedded silicon nitride membrane for studies of nanometer-scale mass transport," *Nano Letters*, vol. 4, no. 11, pp. 2245–2250, 2004.
- [143] P. Mao and J. Han, "Massively-parallel ultra-high-aspect-ratio nanochannels as mesoporous membranes," *Lab Chip*, vol. 9, no. 4, pp. 586–591, 2009.
- [144] H. D. Tong, H. V. Jansen, V. J. Gadgil, C. G. Bostan, E. Berenschot, C. J. M. van Rijn, and M. Elwenspoek, "Silicon nitride nanosieve membrane," *Nano letters*, vol. 4, no. 2, pp. 283–287, 2004.
- [145] K. B. Neeves and S. L. Diamond, "A membrane-based microfluidic device for controlling the flux of platelet agonists into flowing blood," *Lab Chip*, vol. 8, no. 5, pp. 701–709, 2008.
- [146] W. M. Zhang, J. Li, L. X. Cao, Y. G. Wang, W. Guo, K. X. Liu, and J. M. Xue, "Fabrication of nanoporous silicon dioxide/silicon nitride membranes using etched ion track technique," *Nuclear Instruments and Methods in Physics Research Section B: Beam Interactions with Materials and Atoms*, vol. 266, no. 12, pp. 3166–3169, 2008.
- [147] A. Yamaguchi, F. Uejo, T. Yoda, T. Uchida, Y. Tanamura, T. Yamashita, and N. Teramae, "Self-assembly of a silica–surfactant nanocomposite in a porous alumina membrane," *Nature materials*, vol. 3, no. 5, pp. 337–341, 2004.
- [148] G. T. Lim, H. G. Jeong, I. S. Hwang, D. H. Kim, N. Park, and J. Cho, "Fabrication of a silica ceramic membrane using the aerosol flame deposition method for pretreatment focusing on particle control during desalination," *Desalination*, vol. 238, no. 1–3, pp. 53–59, 2009.
- [149] M. S. Tillack, D. W. Blair, and S. S. Harilal, "The effect of ionization on cluster formation in laser ablation plumes," *Nanotechnology*, vol. 15, p. 390, 2004.
- [150] S. I. Anisimov and B. S. Luk'yanchuk, "Selected problems of laser ablation theory," *Physics-Uspekhi*, vol. 45, p. 293, 2002.
- [151] T. Kokubo and H. Takadama, "How useful is SBF in predicting in vivo bone bioactivity?," *Biomaterials*, vol. 27, no. 15, pp. 2907–2915, 2006.
- [152] X. J. Wang, Y. C. Li, J. G. Lin, Y. Yamada, P. D. Hodgson, and C. E. Wen, "In vitro bioactivity evaluation of titanium and niobium metals with different surface morphologies," *Acta biomaterialia*, vol. 4, no. 5, pp. 1530–1535, 2008.
- [153] K. Das, V. K. Balla, A. Bandyopadhyay, and S. Bose, "Surface modification of laser-processed porous titanium for load-bearing implants," *Scripta Materialia*, vol. 59, no. 8, pp. 822–825, 2008.

- [154] L. Jonášová, F. A. Müller, A. Helebrant, J. Strnad, and P. Greil, "Biomimetic apatite formation on chemically treated titanium," *Biomaterials*, vol. 25, no. 7, pp. 1187–1194, 2004.
- [155] S. W. Choi, Y. Zhang, S. Thomopoulos, and Y. Xia, "In Vitro Mineralization by Preosteoblasts in Poly (dl-lactide-co-glycolide) Inverse Opal Scaffolds Reinforced with Hydroxyapatite Nanoparticles," *Langmuir*, vol. 26, no. 14, pp. 12126–12131, 2010.
- [156] L. T. de Jonge, S. C. G. Leeuwenburgh, J. G. C. Wolke, and J. A. Jansen, "Organic–inorganic surface modifications for titanium implant surfaces," *Pharmaceutical research*, vol. 25, no. 10, pp. 2357–2369, 2008.
- [157] S. C. Rizzi, D. J. Heath, A. G. A. Coombes, N. Bock, M. Textor, and S. Downes, "Biodegradable polymer/hydroxyapatite composites: surface analysis and initial attachment of human osteoblasts," *Journal of biomedical materials research*, vol. 55, no. 4, pp. 475–486, 2001.
- [158] B. Yang, M. Uchida, H. M. Kim, X. Zhang, and T. Kokubo, "Preparation of bioactive titanium metal via anodic oxidation treatment," *Biomaterials*, vol. 25, no. 6, pp. 1003–1010, 2004.
- [159] X. X. Wang, S. Hayakawa, K. Tsuru, and A. Osaka, "Bioactive titania gel layers formed by chemical treatment of Ti substrate with a H₂O₂/HCl solution," *Biomaterials*, vol. 23, no. 5, pp. 1353–1357, 2002.
- [160] M. Uchida, H. M. Kim, T. Kokubo, S. Fujibayashi, and T. Nakamura, "Structural dependence of apatite formation on titania gels in a simulated body fluid," *Journal of Biomedical Materials Research Part A*, vol. 64, no. 1, pp. 164–170, 2003.
- [161] P. Li, C. Ohtsuki, T. Kokubo, K. Nakanishi, N. Soga, and K. de Groot, "The role of hydrated silica, titania, and alumina in inducing apatite on implants," *Journal of biomedical materials research*, vol. 28, no. 1, pp. 7–15, 1994.
- [162] H. M. Kim, F. Miyaji, T. Kokubo, and T. Nakamura, "Preparation of bioactive Ti and its alloys via simple chemical surface treatment," *Journal of biomedical materials research*, vol. 32, no. 3, pp. 409–417, 1996.
- [163] W. H. Song, Y. K. Jun, Y. Han, and S. H. Hong, "Biomimetic apatite coatings on micro-arc oxidized titania," *Biomaterials*, vol. 25, no. 17, pp. 3341–3349, 2004.
- [164] R. Rohanizadeh, M. Al-Sadeq, and R. Z. LeGeros, "Preparation of different forms of titanium oxide on titanium surface: Effects on apatite deposition," *Journal of Biomedical Materials Research Part A*, vol. 71, no. 2, pp. 343–352, 2004.
- [165] S. R. Paital and N. B. Dahotre, "Wettability and kinetics of hydroxyapatite precipitation on a laser-textured Ca-P bioceramic coating," *Acta Biomaterialia*, vol. 5, no. 7, pp. 2763–2772, 2009.
- [166] B. Kasemo and J. Gold, "Implant surfaces and interface processes," *Advances in Dental Research*, vol. 13, no. 1, pp. 8–20, 1999.

- [167] R. A. Gittens, T. McLachlan, R. Olivares-Navarrete, Y. Cai, S. Berner, R. Tannenbaum, Z. Schwartz, K. H. Sandhage, and B. D. Boyan, "The effects of combined micron-/submicron-scale surface roughness and nanoscale features on cell proliferation and differentiation," *Biomaterials*, 2011.
- [168] K. C. Popat, L. Leoni, C. A. Grimes, and T. A. Desai, "Influence of engineered titania nanotubular surfaces on bone cells," *Biomaterials*, vol. 28, no. 21, pp. 3188–3197, 2007.
- [169] A. Curtis and C. Wilkinson, "Topographical control of cells," *Biomaterials*, vol. 18, no. 24, pp. 1573–1583, 1997.
- [170] M. J. Dalby, S. J. Yarwood, M. O. Riehle, H. J. H. Johnstone, S. Affrossman, and A. S. G. Curtis, "Increasing fibroblast response to materials using nanotopography: morphological and genetic measurements of cell response to 13-nm-high polymer demixed islands," *Experimental cell research*, vol. 276, no. 1, pp. 1–9, 2002.
- [171] L. E. McNamara, R. J. McMurray, M. J. P. Biggs, F. Kantawong, R. O. C. Oreffo, and M. J. Dalby, "Nanotopographical control of stem cell differentiation," *Journal of tissue engineering*, vol. 1, no. 1, 2010.
- [172] E. M. Pouget, P. H. H. Bomans, J. A. C. M. Goos, P. M. Frederik, N. A. J. M. Sommerdijk, and others, "The initial stages of template-controlled CaCO₃ formation revealed by cryo-TEM," *Science*, vol. 323, no. 5920, pp. 1455–1458, 2009.
- [173] K. M. Woo, V. J. Chen, and P. X. Ma, "Nano-fibrous scaffolding architecture selectively enhances protein adsorption contributing to cell attachment," *Journal of Biomedical Materials Research Part A*, vol. 67, no. 2, pp. 531–537, 2003.
- [174] H. H. Huang, S. J. Pan, and F. H. Lu, "Surface electrochemical impedance in situ monitoring of cell-cultured titanium with a nano-network surface layer," *Scripta materialia*, vol. 53, no. 9, pp. 1037–1042, 2005.
- [175] A. Michiardi, C. Aparicio, B. D. Ratner, J. A. Planell, and J. Gil, "The influence of surface energy on competitive protein adsorption on oxidized NiTi surfaces," *Biomaterials*, vol. 28, no. 4, pp. 586–594, 2007.
- [176] B. Feng, J. Weng, B. C. Yang, J. Y. Chen, J. Z. Zhao, L. He, S. K. Qi, and X. D. Zhang, "Surface characterization of titanium and adsorption of bovine serum albumin," *Materials Characterization*, vol. 49, no. 2, pp. 129–137, 2002.
- [177] A. Oyane, K. Onuma, A. Ito, H. M. Kim, T. Kokubo, and T. Nakamura, "Formation and growth of clusters in conventional and new kinds of simulated body fluids," *Journal of Biomedical Materials Research Part A*, vol. 64, no. 2, pp. 339–348, 2002.